UNIVERSITY OF OSLO
Department of Geosciences

Assessing atmospheric sensitivity to sea surface temperature variations using the Maximum Entropy Production Principle

Master thesis in Geosciences
Meteorology and oceanography

Ada Gjermundsen

21.05.2012

Abstract

Paltridge (1975, 1978) proposed that the atmosphere seeks to maximize entropy production, as a non-equilibrium thermodynamic system. He constructed a simple box model of the atmosphere which yields surprisingly realistic predictions for the latitudinally-averaged surface temperature, fractional cloud cover and meridional heat fluxes.

The poleward shift of the mid-latitude storm tracks is one of the most robust predicted features under global warming. Graff and LaCasce (2012) examined the relation between perturbed sea surface temperature (SST) and the intensity and position of the storm tracks using an Atmospheric General Climate Model (CAM 3.0). In line with several other studies, their findings suggest that both the intensity and position change in response to altered SST.

Heat transport in the atmosphere is intensified in the storm tracks. Thus, a change in the position of the storm tracks should correspond to a change in the maximum heat transport. The purpose of this study is to examine atmospheric sensitivity, and the sensitivity of atmospheric heat transport in particular, to changes in SST using a simplified energy balance model based on the principle of Maximum Entropy Production (MEP), similar to Paltridge's MEP model (1975; 1978).

A hierarchy of box models are developed and investigated, including Paltridge's original model. An Atmospheric MEP (AMEP) model is developed to make a model comparison with CAM 3.0 possible. The results from the AMEP model are compared to data from Graff and LaCasce (2012), to explore if we can capture the SST dependence. Despite having feedback mechanisms, the AMEP model is able to predict the main tendencies of the changes in temperature, convective heat flux and meridional heat transport. However,it fails to capture the shift in the meridional heat transport.

Acknowledgements

First and foremost, I would like to thank Prof. Joe LaCasce for making this an interesting journey. This was so not what I expected to do when I knocked on your door in August! However, it has been a great experience and I have learned so much. Thank you for sharing your enthusiasm and your knowledge, and for excellent guidance throughout. Also thank you for giving me freedom to explore my whims and for answering my questions at any time of the day.

Thanks to Lise and Maria for sharing your CAM3 expertise. An extra thanks to Lise for kindly providing all CAM3 data used in this thesis and for insightful storm tracks comments.

A special thanks to Andrea for proofreading and for adding a taste of academic structure.

Great thanks to Henrik, Rafa and Paulo for making Atmospheric Sciences to so much more than just Science! Henrik, thank you for thinking about everything differently and for teaching me that the Mediterranean Sea is slightly deeper than six meters. Rafa, thank you for asking intricate questions where no answer could satisfy you and for demanding ice cream breaks too often. Paulo, thank you for sharing your knowledge and for interesting discussions about dynamics and strange American food.

Most of all I would like to thank Henrik for giving me the chance to complete my master's degree. Also thank you for your support and care throughout. Life would not have been the same without you.

Ada

Contents

List of Figures

List of Tables

Chapter 1

Introduction

There are two great unexplained mysteries in our understanding of the universe. One is the nature of a unified generalized theory to explain both gravity and electromagnetism. The other is an understanding of the nature of turbulence. After I die, I expect God to clarify the general field theory to me. I have no such hope for turbulence.[1]

The parade of weather systems continuously developing and extinguishing over the mid-latitudes plays an essential part of mid-latitude climate. First, it determines local weather and precipitation patterns in particular. Second, it influences the general circulation in the atmosphere, due to the meridional transport of heat, moisture and momentum.

Mid-latitude cyclones, i.e. transient synoptic eddies, often move in preferred tracks. These tracks are called *storm tracks* and are characterized by maxima in transient eddy activity and eddy fluxes of heat and moisture (Hartmann, 1994, Ch. 6). In the Northern Hemisphere (NH) the storm tracks are most prominent downstream of the Tibetan Plateau over the Pacific Ocean and downstream of the Rocky Mountains over the Atlantic Ocean. In the Southern Hemisphere (SH) the storm tracks are located over the Southern Ocean and are more zonally symmetric than in the NH, due to the greater fraction covered by sea.

The storm tracks have a seasonal cycle. They shift equatorward from fall to midwinter and then migrate poleward afterwards (Lu et al., 2010). During the winter season, both the storm tracks and the jet stream intensify. There is a strong coupling between the storm tracks and the jet, and changes in the intensity or location of one affects the intensity and location of the other. That said, interactions between the large scale flow and the storm tracks are still not fully understood.

The storm tracks also shift poleward in response to global warming (Kushner et al., 2001; Yin, 2005; Lorenz and DeWeaver, 2007; Lu et al., 2007; Brayshaw

[1] Theodore Von Kármán (1881-1963)

et al., 2008; Lu et al., 2010; Graff and LaCasce, 2012). As opposed to the seasonal shifts, this is a shift in the mean location of the tracks. The shift leads to substantial changes in precipitation patterns, as well as in fluxes of heat and momentum, and has large ramifications for mid-latitude regional climate. Nevertheless, the mechanisms responsible for the shift are not clear.

A shift similar to that seen in the storm tracks is found for the mid-latitude jet. This jet is associated with mid-latitude momentum convergence due to eddy activity and is called the *eddy-driven jet*. The Intergovernmental Panel on Climate Change Fourth Assessment Report (IPCC, 2007) found that global circulation models (GCMs) predict a robust poleward shift of the eddy-driven jet in both hemispheres as a response to increased greenhouse gas forcing (Meehl et al., 2007). Due to the strong coupling between the storm tracks and the jet, a shift in both the storm tracks and the jet is expected. However, separating cause and effect in this matter is not simple. With so many open research questions, many different approaches have been applied in order to study interactions between the large scale flow and eddy circulation under global warming.

General Circulation Models (GCMs) are used to simulate many of these dynamic processes, as we understand them. These models are undoubtedly useful at times, but the enormous calculation schemes needed and the numerous feedback mechanisms taking place make GCMs difficult to grasp. Separation of cause and effect is not simple and the results obtained are never better than the method used to represent the process in the first place.

Another common approach is to use simpler models, e.g. one or two dimensional energy balance models (ebm*s*), to analyze the time-mean flow. These models are easier to grasp and have the advantage that multiple simulations can be conducted rapidly. Ebms provide a method by which to look at more specified dependencies, but are seldom able to represent the non-linearity of dynamic processes captured by the GCMs.

Graff and LaCasce (2012) used an Atmospheric GCM (CAM 3.0) to examine changes in the storm tracks due to sea surface temperature (SST) forcing. They found that SST forcing induced changes in both the strength and position of the storm tracks. The changes in the storm tracks corresponded with changes in the eddy-driven jet. Their results are consistent with results from other studies (Brayshaw et al., 2008; Lu et al., 2010). Due to feedback mechanisms in CAM 3.0, there are numerous variables affected by the altered SST. This makes it difficult to single out the reasons for the storm track shift observed in CAM 3.0.

In an attempt to resolve some of the difficulties in research on the mechanisms responsible for the shifts, the purpose of this study is to *examine atmospheric sensitivity, and the sensitivity of atmospheric heat transport in*

particular, to changes in SST using an ebm based on the principle of Maximum Entropy Production. To do so, the shift in the storm tracks is examined using a simplified ebm without any feedback mechanisms. The experiments conducted are based on the study of Graff and LaCasce (2012). Chapter 2 is therefore devoted to presenting their study, which acts as the main incentive for the work carried out in this thesis. The ebm used in this thesis does not contain any dynamics, so neither cyclones nor jet streams exist. The focus is on the shift in the maximal meridional heat transport in the atmosphere. The location of the maximal transport corresponds with the location of the storm tracks.

The ebm is based on the principle of Maximum Entropy Production (MEP), which states that for a thermodynamic system in non-equilibrium (e.g. the climate system), the most probable steady state will be the one with maximum entropy production. Dyke and Kleidon (2010), Kleidon (2009, 2004) and Dewar (2009) argue that the MEP constraint can account for some of the lacking dynamics and that the results obtained may be the same as if dynamical processes were present.

Ebms based on the MEP principle have previously been used in climate sensitivity studies. Grassl (1981) investigated climate sensitivity for a doubling of CO2 using a one dimensional zonal ebm constrained by MEP. The results were inconclusive when compared to a pure ebm. Pujol and Llebot (2000b) used a two dimensional horizontal ebm constrained by MEP to test different climate scenarios. Pujol and Llebot achieved reasonable results when compared to observations of the current climate, but the model exhibited unexpectedly low sensitivity at high latitudes for different climatic scenarios. Paltridge et al. (2007) examined cloud feedback and the response of surface temperature to a doubling of CO2. Compared to results from a GCM, the results where partly consistent. Lorenz et al. (2001) used a one dimensional zonal ebm constrained by MEP to study atmospheres on different planets. Their model successfully predicted zonally averaged temperatures on Earth, Mars and Titan.

The inconclusive results from these studies do not confirm or disprove the assumption that the climate system on Earth acts to maximize entropy production. The goal of the present study is to apply a more strenuous test of the ebm and compare the results to the results of a GCM. The ebm used in the present study also invokes the MEP principle. The fundamentals of the MEP principle and different applications of MEP theory are discussed in detail in chapter 3.

After having presented the main background and theory, the process of finding a suitable model is examined. Paltridge (1975, 1978) constructed the first MEP model. His model is reviewed first (chapter 4). As Paltridge's model is not suited for our purpose, a hierarchy of box models are developed

and investigated (chapter 5). Finally, an Atmospheric MEP model (AMEP) is developed (chapter 6) to allow for a model comparison with CAM 3.0. To compare results from two models that differ in every possible way is not straightforward. The data from CAM 3.0 sometimes need to be calculated in certain ways to make the comparison possible. Where new data calculations are needed a thorough description is given.

The results from AMEP are compared to data from Graff and LaCasce (2012), to see if the models exhibit similar SST dependence (chapter 7). A summary and a discussion of the results are given in chapter 8 and 9.

Chapter 2

The Incentive

Strong meridional gradients in surface temperatures are a common feature of mid-latitude climate. Storm tracks have long been associated with these surface temperature gradients and sea surface temperature (SST) gradients in particular (Brayshaw et al., 2008). Global warming is known to cause an increase in the SST (Levitus et al., 2000) and this in turn affects the storm tracks (Brayshaw et al., 2008; Lu et al., 2010; Graff and LaCasce, 2012).

An increase in the mean SST, increases the heat supply from the surface to the atmosphere. This in turn imposes temperature gradients in the atmosphere, which in combination with the increased latent heat release, is expected to promote storm growth (Brayshaw et al., 2008).

Under global warming, the SST gradients change as well. This is due in part because an increase in SST alters the temperature gradient between the continents and the oceans. The imposed SST gradients play an essential part in the storm track shift (Brayshaw et al., 2008) and in cyclone development in itself.

The idea that cyclone activity is proportional to the background temperature gradient originates from the work of Charney (1947), Eady (1949) and Phillips (1954) and their theories of baroclinic instability. Baroclinic instability arises in rotating, stratified fluids subject to horizontal temperature gradients (Vallis, 2006) and is the main mechanism behind cyclone formation in the atmosphere. Eady, Charney and Phillips all provided linear theories of baroclinic instability which state that the growth rate of baroclinic disturbances (e.g. cyclones) is proportional to the baroclinicity of the fluid. Changes in the surface temperature gradients under global warming affect the baroclinicity and hence alter the cyclone activity and the storm tracks.

Several studies examine the relations between changes in the SST, the resulting baroclinicity and the response of the jet and storm tracks (Brayshaw et al., 2008; Lu et al., 2010; Graff and LaCasce, 2012). The study of Graff and LaCasce (2012) is explained in detail in the following section.

2.1 The study of Graff and LaCasce (2012)

Graff and LaCasce (2012) examine the sensitivity of the mid-latitude storm track position and intensity to the SST boundary forcing using an Atmospheric General Circulation Model (AGCM). The model used is the NCAR Community Atmosphere Model version 3, CAM 3.0, henceforth referred to as CAM3. The resolution used is T42 in the horizontal which can capture features and their horizontal derivatives down to approximately 950km (Hack et al., 2006); they also used 26 height levels in the vertical. The storm tracks in this study are based upon bandpass transient variances. In addition to the storm tracks, the position and intensity of both the subtropical and the eddy-driven jet, the circulation cells and changes in the meridional transport of heat and momentum are examined.

The SST is changed in several different runs in order to examine the effects on the storm tracks, as a result of SST anomalies and SST gradients, in combination and separately. Graff and LaCasce (2012) execute five different experiments in addition to the control run. The SST is altered by 2K in different latitude bands (see figure 2.1):

The 2K run: the SST increased by 2K uniformly over the entire ocean.
The 2K-Lowlat run: the SST increased equatorward of 45°N/S, increasing both the low latitude heating and the mid-latitude SST gradients.
The 2K-Tropics run: the SST increased equatorward of 15°N/S, increasing low latitude heating and the SST gradients around 15°N/S.
The 2K-Highlat run: the SST increased poleward of 45°N/S, decreasing mid-latitude SST gradients.
The Minus 2K-Highlat run: the SST decreased poleward of 45°N/S, increasing mid-latitude SST gradients.

The Results

The data used derive from 20-year averages for the NH winter, DJF, for the period 1 Dec.1980 - 28 Feb.2000. A bandpass filter is applied, retaining fluctuations of approximately 2.5-6 days, to capture the storms. Both the intensity and position of the storm tracks change as a response to the SST forcing.

Increasing the low latitude heating and/or the SST gradients at mid-latitudes, i.e. the 2K, the 2K-Lowlat and the Minus 2K-Highlat runs, result in intensification and a poleward shift of the jet. For the Minus 2K-Highlat run the largest changes occur in the eddy-driven jet, while for the two other runs, i.e. the 2K and the 2K-Lowlat runs, the changes occur for both the subtropical and the eddy-driven jets. The shift in the storm tracks and the jets are accompanied by an intensification and expansion of the Hadley cell.

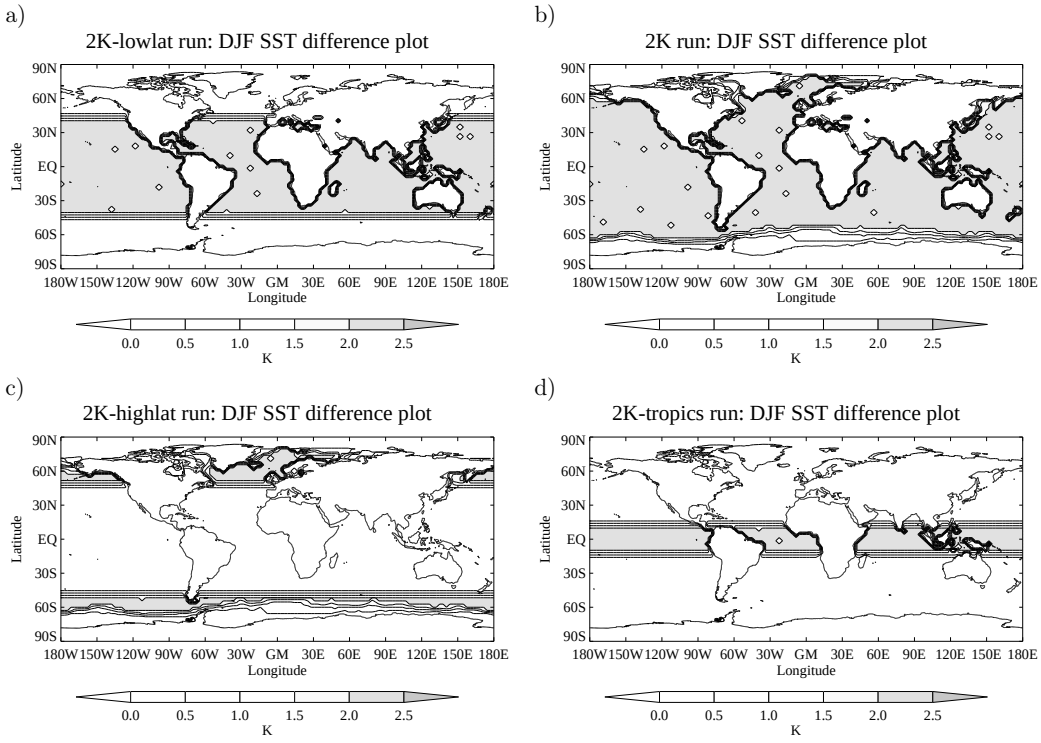

Figure 2.1: The altered SST compared to the control run in the different experiments. (a) The 2K-Lowlat run, (b) The 2K run, (c) the 2K-Highlat run (changes equal the changes in the Minus 2K-Highlat run except negative values used), (d) the 2K-Tropics run. The contour interval is 0.5 K as indicated in the bars beneath the figures. Figure 1 from Graff and LaCasce (2012).

The 2K-Tropics run and the 2K-Highlat run exhibit quite opposite results of the other runs. In both runs an equatorward shift of the storm tracks are seen and in the 2K-Highlat run the storm tracks also weakens. In the 2K-Tropics run there is intensification and an equatorward shift in the subtropical jet. In the 2K-Highlat the eddy-driven jet shifts equatorward while the subtropical jet remains unchanged. A contraction of the Hadley cell is seen in both runs.

Consider for example Figure 6 from Graff and LaCasce (2012) shown here as figure 2.2. The figure shows the difference of the results from the 2K-Lowlat run and the control run. In figure 2.2 a, b, d and f only data from bandpass-filtered fields are shown. In figure 2.2 c and e the temporally-averaged fields are shown. Figure 2.2 a), c) and d) are of main interest when a comparison is made later on in this work.

Figure 2.2 a) shows the bandpass-filtered **Z** difference fields. **Z** is the standard deviation of the temporally-averaged field of the geopotential height. The storm tracks have both intensified and shifted poleward in both hemispheres compared to the control run. The maxima in the **Z** field are approximately

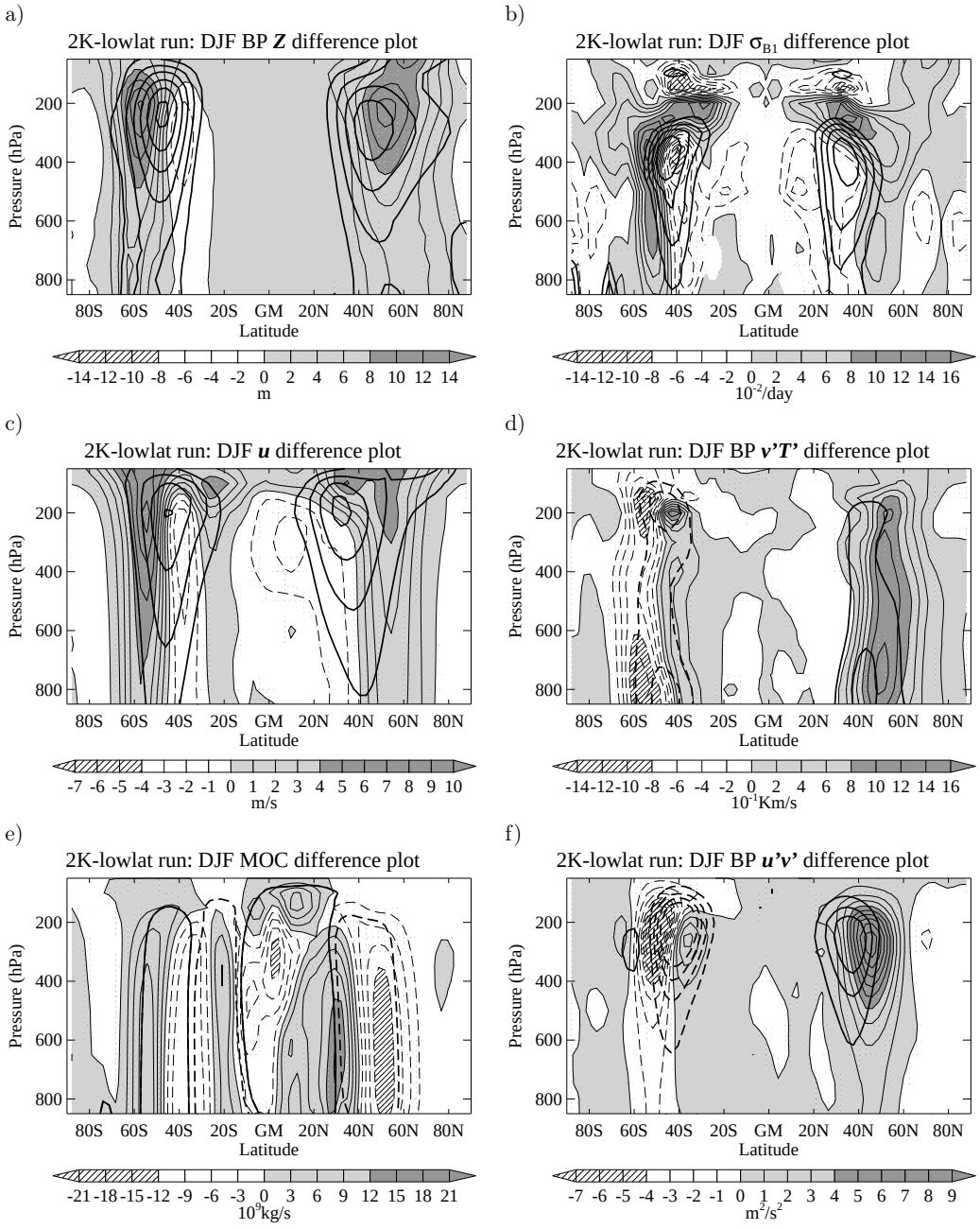

Figure 2.2: Zonally averaged DJF difference plots from the 2K-Lowlat run. The thick solid (stippled) contours are positive (negative) control run contours for reference. The thin filled contours are difference field contours. (a) The bandpass(BP) standard deviation difference field, **Z**. (b) The difference field for the Eady parameter of maximum baroclinic growth, σ_{B1}. (c) The mean wind difference field, **u**. (d) The meridional heat transport, **v'T'**, difference field. (e) The difference field for the meridional overturning circulation streamfunction, Φ. (f) The meridional flux of momentum, **u'v'**, difference field. Figure 6 from Graff and LaCasce (2012).

20% stronger and the shift is approximately 7 to 8°N/S.

Figure 2.2 c) shows the temporally- and zonally-averaged zonal wind, **u**. In the SH both the subtropical jet and the eddy driven jet have intensified and shifted. The eddy-driven jet is shifted poleward while the subtropical jet is shifted upward. The distinction between the two jets is not so clear in the NH, but intensification and a poleward shift are clearly seen.

The bandpass-filtered eddy heat flux, **v'T'**, seen in figure 2.2 d), has intensified and shifted poleward in both hemispheres. The difference is almost barotropic over much of the troposphere.

Chapter 3

The principle of Maximum Entropy Production (MEP)

Are you sitting comfortably? Then I'll begin[1]

The circulation in the atmosphere and ocean transforms the absorbed solar radiation into motion and determines the weather and climate as we know it. The circulation has many degrees of freedom and exhibits nonlinear interactions of several components on different time scales. This makes predictions, both for weather and climate, complicated. The dynamics in such systems are chaotic and characterized by internally generated variability.

GCMs and ebms are used to study the dynamical processes determining the climate. Both approaches can provide useful information in their own way, but either way we face the same problem; the non-linear dynamic regime is difficult to grasp. As a result there is a search for a fundamental principle that governs the dynamics of non-linear systems. To find the existence of such a principle would increase our understanding and simplify the calculations needed to predict the features of our climate system.

3.1 In search of an extremum principle

Chaotic systems, like the climate system, exhibit aperiodic behavior that depends sensitively on initial conditions, making long-term predictions impossible. Lorenz (1963) showed that tiny errors in measuring the current state of the atmosphere would be amplified rapidly, eventually leading to poor forecasts. Feigenbaum (1978, 1983) discovered that in spite of the disorder, there are certain universal laws (e.g. Feigenbaum's δ) governing the transition from regular to chaotic behavior. Completely different systems can become chaotic the same way. In this way Feigenbaum found a structure

[1] Julian Lang, *Listen With Mother*, BBC radio 1950-1982.

embedded in nonlinear systems.

Similarly, researchers have sought certain fundamental principles under which the nonlinear systems operate. These might help predict "climate", i.e. the mean state of the system. Several attempts have been made to find such a principle for the general circulation on Earth (Paltridge, 1975, 1978; Ziegler and Wehrli, 1987; Dewar, 2003, 2005; Kleidon, 2004, 2009), and for the atmospheric circulation in particular (Lorenz, 1955, 1960; Lin, 1982).

Edward N. Lorenz (1955; 1960) suggested that the general circulation of the atmosphere may be operating near its maximum possible rate, such that the generation of available potential energy (APE) is maximized. Charles A. Lin (1982) found that the principle of maximization of APE was reduced to a maximization of the correlation between heating and temperature deviation when applied to a one dimensional zonal ebm. G. W. Paltridge (1975; 1978) showed by using a one-dimensional zonal ebm that the climate system was working as to maximize the rate of entropy production. Paltridge (1979; 1981; 2001) also suggested that the energy flow actually was maximizing the rate of dissipation, instead of the entropy production, and argued that the maximization of one did not necessarily imply the maximization of the other.

One question arises; do these extremal states differ or are they different sides of the same grand thermodynamic potential? Figure 3.1 shows some of the processes considered in the articles mentioned in the previous paragraph. Diabatic effects, as radiative and frictional heating, generate the total potential energy in the atmosphere. The total potential energy is the sum of the internal and the potential energy. The kinetic energy dissipates by viscous forces with entropy production and frictional heating as a result. In a steady state all the arrows must be equal in magnitude. This implies that the generation of APE transformed into kinetic energy equals the rate of dissipation of energy by frictional forces, and the dissipation of energy is an irreversible process generating entropy. It is tempting to draw the conclusion that maximizing one means maximizing them all and that all the extremum principles suggested correspond to the same steady state.

Ozawa et al. (2003) showed that if the entire atmosphere is assumed to be in a steady state and that the viscous heating rate is negligible compared to the radiative heating (or cooling), the generation of APE is proportional to the entropy production and hence maximization of one would imply maximization of both. Ozawa et al. (2003) findings contradict the findings of Paltridge (1979, 1981, 2001). However, it is beyond the scope of this thesis to find the "true" answer for this question (but I hope it will occupy your thoughts after you finish reading.).

3.2 Maximum Entropy Production

In this thesis only one of the extremal principles is considered, namely the maximization of the rate of entropy production. The Maximum Entropy

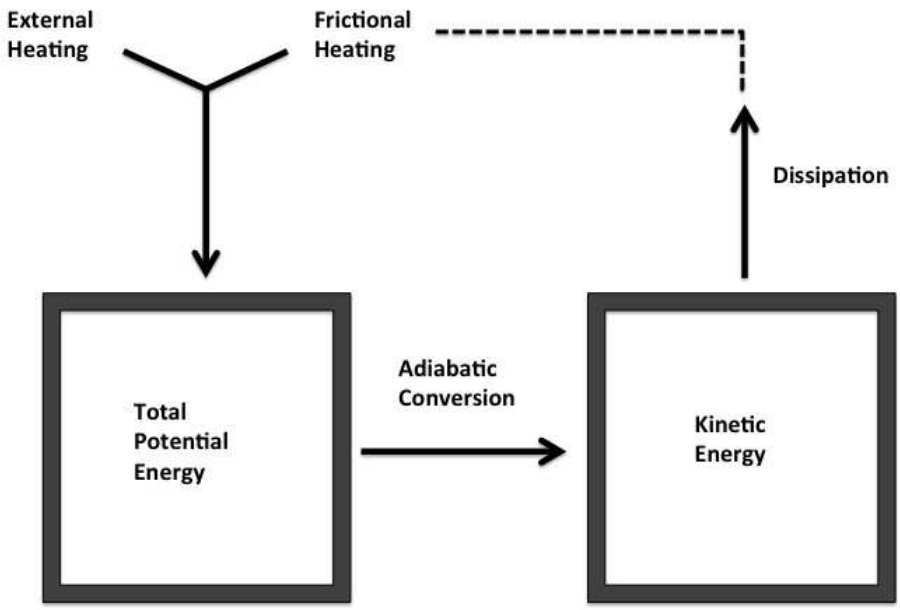

Figure 3.1: The energy cycle in the atmosphere. Diabatic heating generates internal and potential energy (Total potential energy). Parts of the total potential energy (i.e. APE) is converted into kinetic energy which dissipates due to viscosity. In a steady state all the arrows must equal in magnitude. Figure adapted from Lorenz (1955).

Production Principle states that *for a steady state system, the MEP state is the most probable state out of many possible non-equilibrium steady states.* The MEP principle arises from non-linear thermodynamics and is an attempt to extend the second law of thermodynamics to non-equilibrium systems.

3.2.1 The lack of proof

The MEP principle has not been proven, but many other principles we consider correct, like the first and second law of thermodynamics, (or most theories in social sciences) have never been proven either. All the successful applications of these laws have lead to a consensus of their validity. The same applies for the MEP principle. The only way to prove it seems to be applying it to numerous (climate) scenarios and judging the results obtained.

Many attempts have been made to relate the MEP principle to other existing principles, like the second law of thermodynamics, and in this way "prove" it (Ziegler and Wehrli, 1987; Dewar, 2003, 2005). The numerous attempts have not yet accomplished this goal and the assumptions made in the deductions have often been less obvious than the MEP principle itself (Martyushev,

2010).

Consequently no proof for the MEP principle is given in this chapter either. Instead a explanation of the fundamentals of non-linear thermodynamics and the assumptions made for the MEP theory is given.

3.2.2 Equilibrium and non-equilibrium thermodynamics

The theory of thermodynamics is based on two fundamental laws. The first law of thermodynamics states that the energy of an isolated system is conserved. The second law of thermodynamics states that any large system in equilibrium will be found in the state with the greatest entropy (Schroeder, 2000). Non-equilibrium thermodynamics describes transport processes in systems that are out of equilibrium and for such systems the second law of thermodynamic needs to be reformulated to make it more suitable for our purposes.

A brief explanation of the differences in the equilibrium and non-equilibrium regime of thermodynamics is given later on in this section, but first it is important to clarify what we refer to when we say *entropy*.

Entropy - one word, different meanings

By far the most abused word in science is entropy.[2]

Many definitions of entropy appear in literature and it is not always clear which definition is used. The *experimental entropy* S of Clausius, Gibbs and G. N. Lewis, S(T, P, N,...), is a function of the observed macroscopic quantities. Shannon defined an *information entropy* $S = -\sum p_i \ln(p_i)$ which is a property of any probability distribution. In quantum theory the entropy is defined as $S = -\mathrm{Tr}(\rho \ln(\rho))$, where ρ is the density matrix and Tr is the trace. Then there is the more common *Bolzmann, Einstein and Planck entropy* $S = \mathrm{k} \cdot \ln(\Omega)$, where k is the Bolzmann constant and Ω is the multiplicity of a given macrostate. At last we will mention *Gibbs entropy* which is similar to the information entropy, $S = -\mathrm{k} \cdot \sum p_i \ln(p_i)$. There are several more as well.

The expression for entropy used in this thesis is the classical thermodynamic definition of entropy based on the work of Rudolf Clausius (Clausius, 1865). *Clausius' Inequality* states that the following equation must be true for any cyclic process, reversible or irreversible,

$$\oint \frac{\mathrm{d}Q}{T} \leq 0 \tag{3.1}$$

[2] Jaynes (1980)

over any possible path, where dQ is the amount of heat added to the system and T is the absolute temperature of the system. The equality holds if the process is reversible, for which the expression is the called *Clausisus' Equality*, i.e.

$$\oint \frac{\mathrm{d}Q_{rev}}{T} = 0 \tag{3.2}$$

where dQ_{rev} is the amount of heat added quasi-statically to the system. The integral in equation 3.2 is path-independent of a quasi-static process, but is uniquely defined by the initial and final states of the system. Thus we can define a state function; the entropy S, which satisfies

$$0 = \oint \frac{\mathrm{d}Q_{rev}}{T} = \oint \mathrm{d}S \tag{3.3}$$

It follows that the entropy is defined with respect to some arbitrary constant, which defines zero entropy. The definition of this constant is ambiguous and will not be included, so the physical meaning is the *change* in entropy, rather than the absolute value of the entropy itself. The change in entropy is defined as

$$\Delta S \equiv \int \frac{\mathrm{d}Q_{rev}}{T} \tag{3.4}$$

for a reversible process.

There is no unique expression for irreversible processes. If we consider some process where the system changes from state A to state B along a path that may be irreversible and are restored to its initial state, A, along a reversible path, we can write the Clausius Inequality as

$$\int_A^B \frac{\mathrm{d}Q}{T} + \int_B^A \frac{\mathrm{d}Q_{rev}}{T} \leq 0 \tag{3.5}$$

where dQ is the heat added along the path from A to B and dQ_{rev} is the heat added along the reversible path, B to A. Since the path from B to A is reversible, it can be carried out in reverse, giving

$$\int_B^A \frac{\mathrm{d}Q_{rev}}{T} = -\int_A^B \frac{\mathrm{d}Q_{rev}}{T} = -\Delta S_{A\to B} \tag{3.6}$$

using the expression from 3.6 in 3.5, we get

$$\int_A^B \frac{\mathrm{d}Q}{T} - \Delta S_{A\to B} \leq 0 \tag{3.7a}$$

$$\Delta S_{A\to B} \geq \int_A^B \frac{\mathrm{d}Q}{T} \tag{3.7b}$$

for infinitesimal changes

$$\mathrm{d}S \geq \frac{\mathrm{d}Q}{T} \tag{3.8}$$

Equation 3.8 is the second law of thermodynamics for which

$$\mathrm{d}S = \frac{\mathrm{d}Q_{rev}}{T} \quad \text{(reversible process)} \tag{3.9}$$

$$\mathrm{d}S \geq 0 \quad \text{(irreversible process)} \tag{3.10}$$

Equilibrium thermodynamics

The second law of thermodynamics, i.e. equation 3.8, states that the entropy tends to increase (Schroeder, 2000). If a system has a different temperature from its surroundings, energy exchange between the system and its surroundings occurs spontaneously from the warmer to the cooler region. Dissipation of energy raises the temperature in the colder region and temperature gradients within the system dissipate in time. The dissipation of energy is an irreversible process and produces entropy. Thermodynamic equilibrium is achieved when the system has the same temperature as the surroundings and the energy exchange between the two, and hence production of entropy, stops. The entropy production for the system is

$$\frac{\mathrm{d}S}{\mathrm{d}t} = \dot{S}_{irr} \geq 0 \tag{3.11}$$

where $\dot{S}_{irr}$ is the production of entropy within the system due to irreversible processes. A system in thermodynamic equilibrium is in a state with maximum entropy; hence $\dot{S}$ will equal zero when the equilibrium state is achieved.

Non-equilibrium thermodynamics

Not all systems can reach a state of thermodynamic equilibrium. The Sun, space (e.g. surroundings) and the Earth (e.g. system) is one example of a system which is kept in a non-equilibrium state. Energy is continuously exchanged and dissipated between the system and its surroundings, and the state of thermodynamic equilibrium is never reached. According to Ziegler and Wehrli (1987) the total entropy production for a non-equilibrium system is changing as

$$\dot{S} = \dot{S}_{irr} - \dot{S}_{rev} \tag{3.12}$$

where $\dot{S}_{irr}$ is the entropy produced inside the system (see equation 3.11) and $\dot{S}_{rev}$ is the reversible contribution which represents the divergence of entropy fluxes, i.e. the net entropy exchange from the system with its surroundings, with the net entropy export defined as positive.

Here is worth noting

$$\dot{S}_{irr} = \dot{S} + \dot{S}_{rev} \geq 0 \tag{3.13}$$

so the second law is still fulfilled even if the entropy production within the system, i.e. $\dot{S}$, decreases in time.

A steady state of the system is reached when the generation rate of the potential energy is balanced by the energy dissipation rate (see figure 3.1), so no kinetic energy is stored in the system. Then the net production of entropy within the system (i.e. $\dot{S}_{irr}$) equals the net export of entropy from the system to its surroundings (i.e. $\dot{S}_{rev}$)

$$\dot{S} = 0 \rightarrow \dot{S}_{irr} = \dot{S}_{rev} = \frac{\mathrm{d}F}{T} \tag{3.14}$$

where

$$\mathrm{d}F = \frac{\mathrm{d}Q_{rev}}{\mathrm{dt}} \tag{3.15}$$

3.2.3 The entropy production for the climate on Earth

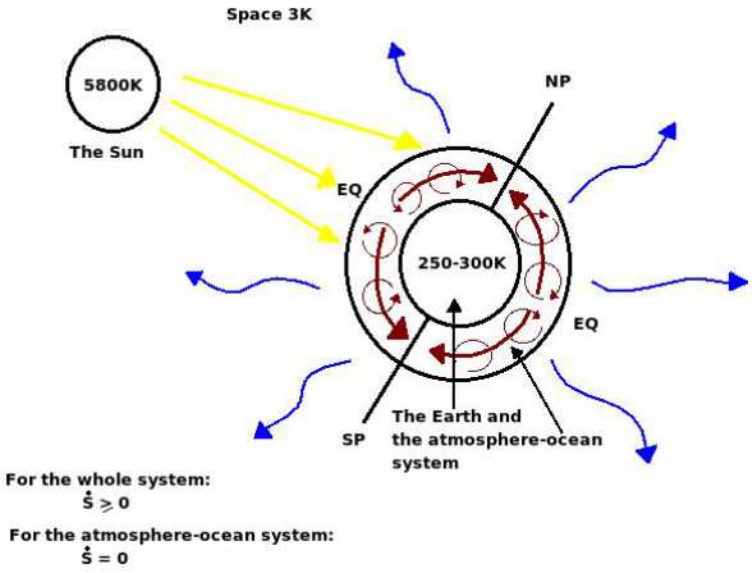

Figure 3.2: The Earth's climate system (i.e. the atmosphere-ocean system) and its surroundings. Given the assumption that the climate system is in a steady state, the entropy produced within the climate system equals the net entropy export from the system to its surroundings. This results in zero entropy production within the climate system and a positive entropy production of the surroundings, i.e. the Sun, the Earth and space. Figure adapted from Ozawa et al. (2003).

The climate system on Earth is a system far from thermodynamic equilibrium. The net inbalance in radiation between the tropics and the poles sustains temperature gradients and acts as a driving force for global circulation. The circulation in the atmosphere and in the ocean continuously transports heat from the tropics toward the poles and by doing so dissipates energy resulting in entropy production.

To use the MEP principle one needs a system in steady state. The climate system, with its seasonal variations, is not in a steady state. In addition, in a long term mean, the climate is warming. However, if one considers zonal and annual mean, the inflow rate of energy in the climate system equals the outflow rate of energy, since no heat is stored in the system and one can argue that in this case the climate system is in a steady state.

Given the assumptions above, one can consider the climate system as a system driven towards a MEP state and, consequently, a maximization of $\dot{S}_{irr}$ (see equation 3.12).

In what follows, expressions for the entropy production, $\dot{S}$, $\dot{S}_{irr}$ and $\dot{S}_{rev}$, are calculated and the quantity maximized representing the MEP state shown. The derivations in this section are based on those of Ziegler and Wehrli (1987); Ozawa et al. (2001) and Kleidon (2009)

The climate system, i.e. the atmosphere and the ocean, can be regarded as a small, dissipative system connected to two surrounding heat reservoirs, the Sun and the Earth, see figure 3.2. The entropy production of a dissipating system is given by

$$\dot{S} = \frac{dS}{dt}_{system} = \frac{d}{dt}\left[\int_V \rho s \,\mathrm{d}V\right] = \int_V \frac{\partial(\rho s)}{\partial t}\,\mathrm{d}V + \int_A \rho s \mathbf{v}\cdot\hat{n}\,\mathrm{d}A \tag{3.16}$$

where ρ is the density of the fluid, s is the entropy pr. unit mass, $\mathbf{v}$ is the velocity at surface A, V is the volume of the system, A is the surface bounding the system and $\hat{n}$ is the surface normal (positive outward).
Using the continuity equation

$$\frac{\partial(\rho s)}{\partial t} = \rho\frac{\partial s}{\partial t} + s\frac{\partial \rho}{\partial t} = \rho\frac{\partial s}{\partial t} - \nabla\cdot(\rho s\mathbf{v}) + \rho\mathbf{v}\cdot\nabla s \tag{3.17}$$

and Gauss' theorem

$$\int_A \rho s\mathbf{v}\cdot\hat{n}\,\mathrm{d}A = \int_V \nabla\cdot(\rho s\mathbf{v})\,\mathrm{d}V \tag{3.18}$$

the entropy production (equation 3.16) can be written as

$$\dot{S} = \int_V \rho\left[\frac{\partial s}{\partial t} + \mathbf{v}\cdot\nabla s\right]\mathrm{d}V \tag{3.19}$$

The expression in square brackets is the time derivative of the entropy pr. unit mass (ds/dt). Using the general thermodynamic relation

$$ds = \frac{\mathrm{d}q}{T} = \frac{\mathrm{d}u + p\,\mathrm{d}V - \sum \mu_j\,\mathrm{d}n_j}{T} \tag{3.20}$$

for which q is the heat gain pr. mass unit, we get

$$\dot{s} = \frac{1}{T}\left(\frac{\mathrm{d}u}{\mathrm{d}t} + p\frac{\mathrm{d}(1/\rho)}{\mathrm{d}t} - \sum \mu_j\frac{\mathrm{d}n_j}{\mathrm{d}t}\right) \tag{3.21}$$

where u is the internal energy pr. unit mass, p is pressure, μ_j is the chemical potential of component j, n_j is the number of the jth component pr. unit mass. Since we do not consider any change in the chemical composition in the climate system the last term is not included in further calculations. By substituting for the time derivative

$$\dot{s} = \frac{\partial s}{\partial t} + \mathbf{v} \cdot \nabla s \tag{3.22}$$

and using the continuity relation

$$\frac{\mathrm{d}(1/\rho)}{\mathrm{d}t} = -\frac{1}{\rho^2}\frac{\mathrm{d}\rho}{\mathrm{d}t} = \frac{1}{\rho}\nabla \cdot \mathbf{v} \tag{3.23}$$

equation 3.19 can be written as

$$\dot{S} = \int_V \left[\frac{1}{T}\left(\rho\frac{\partial u}{\partial t} + \rho\mathbf{v} \cdot \nabla u + p\nabla \cdot \mathbf{v}\right)\right] \mathrm{d}V \tag{3.24}$$

The terms in the parentheses can be rewritten using the relations

$$\rho\frac{\partial u}{\partial t} + \rho\mathbf{v} \cdot \nabla u = \frac{\partial(\rho u)}{\partial t} + \nabla \cdot (\rho u\mathbf{v}) \tag{3.25}$$

and

$$u = c_v T \tag{3.26}$$

where c_v is the specific heat constant per unit mass at constant volume, giving

$$\dot{S} = \int_V \left[\frac{1}{T}\left(\frac{\partial(\rho c_v T)}{\partial t} + \nabla \cdot (\rho c_v T\mathbf{v}) + p\nabla \cdot \mathbf{v}\right)\right] \mathrm{d}V \tag{3.27}$$

which is the rate of entropy change in the system (i.e. equation 3.12).

The entropy of the surrounding system (i.e. the Sun, the Earth and space) is changed by the net heat fluxes through the boundary surface (A), in our case the top of the atmosphere (TOA). The radiative heat exchange between the Sun, the Earth and space is irreversible and we do not know how to calculate entropy changes for irreversible processes, but it does not matter. Entropy is a state function and independent of path. We have to imagine a reversible path which will result in the same dQ and calculate the entropy change for this path using Clausius equation, which states that the entropy production by the net heat flux emitted through TOA is given by the net heat flux divided by the absolute temperature

$$\dot{S}_{rev} = \int_A \frac{\mathrm{d}F_{net}}{T}\,\mathrm{d}A \tag{3.28}$$

where F_{net} is the net heat flux pr. unit surface at TOA and defined positive outward. Note that we can not do this for $\dot{S}_{irr}$ since we do not have any

expression for dQ from irreversible processes.

Using equation 3.13, the entropy production due to irreversible processes, i.e. turbulent heat transfer, in the climate system can be written as

$$\dot{S}_{irr} = \dot{S} + \dot{S}_{rev}$$

$$= \int_V \left[\frac{1}{T} \left(\frac{\partial(\rho c_v T)}{\partial t} + \nabla \cdot (\rho c_v T \mathbf{v}) + p \nabla \cdot \mathbf{v} \right) \right] + \int_A \frac{\mathrm{d}F_{net}}{T} \, \mathrm{d}A \qquad (3.29)$$

If the climate system is in a steady state, the entropy of the system should remain unchanged, i.e. $\dot{S}$ =0. Hence, the entropy production due to turbulent heat transfer, $\dot{S}_{irr}$, becomes

$$\dot{S}_{irr} = \dot{S}_{rev} = \int_A \frac{\mathrm{d}F_{net}}{T} \, \mathrm{d}A \qquad (3.30)$$

So the MEP state for our climate system has

$$\dot{S}_{irr} = \int_A \frac{\mathrm{d}F_{net}}{T} \, \mathrm{d}A = \text{maximum} \qquad (3.31)$$

3.2.4 Entropy production due to radiation processes vs. turbulent heat transfer

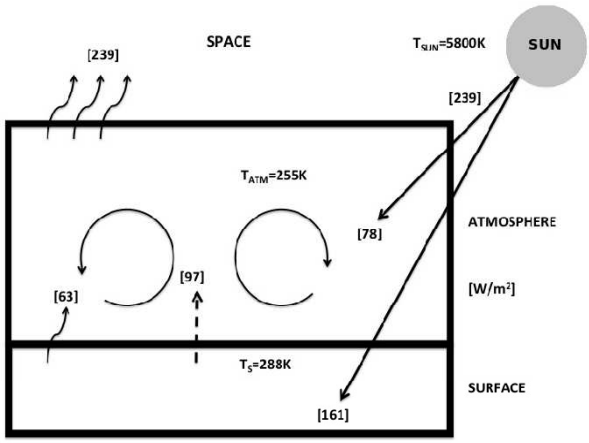

Figure 3.3: The energy budget for the Earth. Globally averaged energy fluxes given in [W/m2]. The flux values are taken from Trenberth et al. (2009) and are based on satellite retrievals from the CERES data sets. The net absorption of 0.9W/m2 for the surface resulting in global warming is included but will not be discussed (the purpose of including the figure is quite different).

A schematic of the global mean energy budget for the climate system is shown in figure 3.3. The values in brackets represent the energy fluxes in W/m2 and the temperatures are the brightness temperature of the Sun (5800K),

the global mean surface temperature (288K) and the global mean emission temperature of Earth (255K). The entropy production in the universe due to all irreversible processes in the climate system on Earth can be calculated as (Ozawa et al., 2003)

$$\begin{aligned}\dot{S}_{universe} \simeq \dot{S}_{surr} &= \big(\frac{1}{T_{ATM}} - \frac{1}{T_{SUN}}\big)\mathrm{d}F_{sun} \\ &= \big(\frac{1}{255K} - \frac{1}{5800K}\big)239\tfrac{W}{m^2} \simeq 0.9\tfrac{W}{Km^2}\end{aligned} \tag{3.32}$$

This entropy production can be partitioned into atmosphere, surface and atmosphere-surface interaction components

$$\dot{S}_{turb} = \big(\frac{1}{255K} - \frac{1}{288K}\big)97\tfrac{W}{m^2} = 0.04\tfrac{W}{Km^2} = 0.05\dot{S}_{universe} \tag{3.33}$$

$$\dot{S}_{\substack{sw\\surf}} = \big(\frac{1}{288K} - \frac{1}{5800K}\big)161\tfrac{W}{m^2} = 0.53\tfrac{W}{Km^2} = 0.59\dot{S}_{universe} \tag{3.34}$$

$$\dot{S}_{\substack{sw\\atm}} = \big(\frac{1}{255K} - \frac{1}{5800K}\big)78\tfrac{W}{m^2} = 0.03\tfrac{W}{Km^2} = 0.33\dot{S}_{universe} \tag{3.35}$$

$$\dot{S}_{\substack{lw\\atm}} = \big(\frac{1}{255K} - \frac{1}{288K}\big)63\tfrac{W}{m^2} = 0.28\tfrac{W}{Km^2} = 0.03\dot{S}_{universe} \tag{3.36}$$

The entropy produced due to absorption of solar radiation by the atmosphere and the surface are by far the greatest terms (equations 3.34 and 3.35), but it is not the entropy produced by radiative processes that is maximized according to the MEP theory.

In turbulent heat transfer there is a competing process between the heat flux and the temperature gradient. Changes in one of them alter the other, resulting in a non-linear entropy production (described in detail in section 3.2.6). In contrast, when radiation is absorbed, there are no feedback mechanisms between the radiative flux and the absorptivity of the absorbing matter. Ozawa et al. (2003) argued that absorption of radiation can in this context be considered a linear process and linear processes are not maximized. Consequently, it is only the entropy production from the turbulent heat transfer that tends to be maximized even if the contribution from this term is only 5% of the total entropy production (see equation 3.33).

Pujol and Llebot (1999, 2000a) used a one dimensional zonal ebm based on the MEP model made by Paltridge (1975; 1978) (described in chapter 4) to calculate annually- and zonally-averaged surface temperatures and cloud cover maximizing the entropy production. Pujol and Llebot; Pujol and Llebot

executed different runs including all of the entropy production components (eqn. 3.33-3.36) and only the entropy production produced from turbulent heat transfer (eqn. 3.33). The results for the different entropy production runs were the same, indicating that the entropy produced from turbulent processes is the one that tends to be maximized.

3.2.5 Maximum vs. minimum entropy production

The MEP principle differs from another well-known entropy principle proposed by Prigogine (1947), namely *The Principle of Minimum Entropy Production*. The principle states that stationary non-equilibrium states are characterized by a minimum entropy production. The theorem applies only to the linear regime of dynamics for fluids without any turbulent motions. The assumptions needed to apply this principle are numerous, making it not applicable for most systems. The relationship between the minimum entropy production principle and the MEP principle is not simple, but the two are absolutely different (Martyushev and Seleznev, 2006) and should not be mixed. The minimum entropy production principle is not discussed further in this work.

3.2.6 MEP for a two-box blackbody climate system

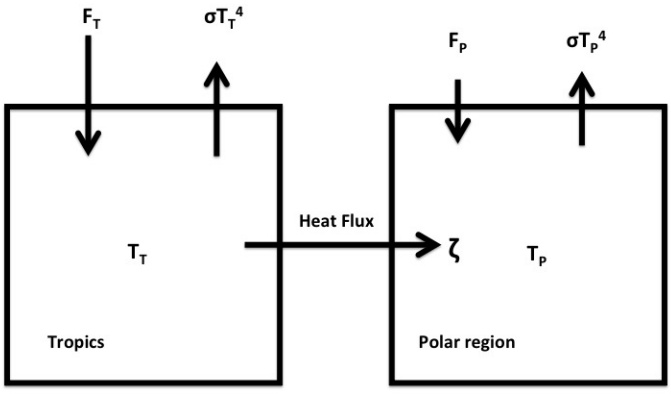

Figure 3.4: (a) A two-box blackbody model of the climate system is used to calculate the entropy production associated with the meridional heat flux, ζ, from the tropics to the polar region. One box represents the tropics and the other box represents the polar region. The solar insolation at TOA is F_T and F_P for the tropics box and the polar box, respectively. Both boxes emit radiation according to Stefan-Bolzmann law.

In the previous sections the MEP theory fundamentals are explained. This additional example is included with the intention of making the theory easier to understand and to explain the MEP calculation method used throughout this thesis.

Figure 3.4 shows a two-box representation of the climate system. One box represents the tropics and the other represents the polar region. There is an incoming flux of solar radiation, F, in each box, with greater insolation in the tropics. Both boxes emit radiation according to the Stefan-Boltzmann law. In addition to radiative fluxes, there is a meridional heat flux, ζ, representing turbulent heat transfer from the warmer to the colder regions in the system.

Assuming energy balance within each box provides two equations

$$F_T - \sigma T_T^4 - \zeta = 0 \tag{3.37}$$
$$F_P - \sigma T_P^4 + \zeta = 0 \tag{3.38}$$

Assuming the insolation in each box, F_T and F_P, are known, there are three unknowns, T_1, T_2 and ζ, but only two equations. To solve the system of equations we need a third condition. Assuming that the system is in a MEP state provides this condition. This can be written as

$$\dot{S}_{irr} = \dot{S}_{rev} = -\frac{\zeta}{T_T} + \frac{\zeta}{T_P} = \zeta\Big(\frac{1}{T_P} - \frac{1}{T_T}\Big) = \text{maximum} \tag{3.39}$$

The sign convention used is that the entropy production is positive when heat is added to the box, i.e. ζ for the polar region box, and negative when heat is removed from the box, i.e. ζ for the tropics box. For simplicity the subscript of $\dot{S}_{irr}$ is dropped hereafter

Defining

$$\zeta = \zeta_T = -\zeta_P \tag{3.40}$$

the energy balance equation for each box i={T,P} can be written as

$$F_i - \sigma T_i^4 - \zeta_i = 0 \tag{3.41}$$

where ζ_i is the meridional heat divergence of box i. The system can now easily be extended to contain an arbitrary number of boxes.

The maximization problem

If we first consider the continuous case, using infinitely many boxes, the energy balance equation at each latitude, ϕ, can be written as

$$F(\phi) - \sigma T(\phi)^4 - \zeta(\phi) = 0 \tag{3.42}$$

The total entropy production due to the meridional heat divergence is

$$\dot{S}_{total} = -\int_{-\frac{\pi}{2}}^{\frac{\pi}{2}} \frac{\zeta(\phi)}{T(\phi)} \mathrm{d}\phi = -\int_{-\frac{\pi}{2}}^{\frac{\pi}{2}} \frac{F(\phi) - \sigma T(\phi)^4}{T(\phi)} \mathrm{d}\phi \tag{3.43}$$

which is maximized with respect to the temperature, $T(\phi)$, to find the MEP state. This is a variational problem, and the integral is in the standard variational form

$$\int_{-\frac{\pi}{2}}^{\frac{\pi}{2}} \mathcal{F}(\phi, T, T') \mathrm{d}\phi \tag{3.44}$$

where $\mathcal{F}(\phi, T, T') = \frac{F(\phi) - \sigma T(\phi)^4}{T(\phi)}$ and T'=dT/dϕ. The corresponding Euler-Lagrange (E-L) equation is

$$\frac{\mathrm{d}}{\mathrm{d}\phi} \frac{\partial \mathcal{F}}{\partial \mathrm{T}'} - \frac{\partial \mathcal{F}}{\partial \mathrm{T}} = 0 \tag{3.45}$$

and since $\mathcal{F}$ is only a function of T the E-L equation is reduced to

$$\frac{\partial \mathcal{F}}{\partial \mathrm{T}} = 0 \tag{3.46}$$

This shows that maximizing the total entropy production is the same as maximizing the entropy production w.r.t. temperature at each latitude separately. So one may maximize the entropy production in each "box", instead of the total entropy production.

The solution method

To find the maximum entropy production, the method of Lagrange multipliers is used. The entropy production associated with the meridional heat divergence in the ith box model is

$$\dot{S}_i = -\frac{\zeta_i}{T_i} = -\frac{F_i - \sigma T_i^4}{T_i} \tag{3.47}$$

To find the maximal entropy production for each box, we need to find ζ_i such as to maximize $\dot{S}_i$ subject to the global radiative equilibrium constraint $\sum_i F_i - \sigma T_i^4 = 0$, which states that no energy is stored within the system. To solve this problem a Lagrangian cost function, $\mathscr{L}$, is used

$$\mathscr{L} = \sum_i -\frac{\zeta_i}{T_i} + \beta \sum_i F_i - \sigma T_i^4 = \sum_i \frac{F_i - \sigma T_i^4}{T_i} - \beta \sum_i F_i - \sigma T_i^4 \tag{3.48}$$

where β is the Lagrangian multiplier, constant for all boxes. The constrained maximum of the $\dot{S}$ can be found by maximizing $\mathscr{L}$ with respect to β and T_i. Thus to find the MEP state for the system, we need to solve the non-linear equation:

$$\frac{\partial \mathscr{L}}{\partial T_i} = \sigma T_i^4 \big(4\beta T_i - 3\big) - F_i = 0 \tag{3.49}$$

for each box separately, subject to the constraint

$$\frac{\partial \mathscr{L}}{\partial \beta} = -\sum_i F_i - \sigma T_i^4 = 0 \tag{3.50}$$

The solution is obtained numerically. Equation 3.49 is solved for each box separately, while β is adjusted until equation 3.50 is satisfied.

If we return to the two boxes seen in figure 3.4 we now have a method for solving the system of equations and to find the three unknowns T_T, T_P and ζ. For insolation F_T=300Wm^{-2} and F_P=170Wm^{-2}, we get T_T=262K , T_P=244K and ζ=32Wm^{-2}. These values are reasonable in light of the global mean emission temperature on Earth of 255K (Hartmann, 1994, Ch. 2) and the observed meridional heat divergence of 20-40Wm^{-2} (Lorenz et al., 2001). The two box models are investigated further in chapter 5.

3.2.7 The linear approach

Some assume a flux gradient relation between ζ and $T_T - T_P = \Delta T$, i.e.

$$\zeta = k \cdot \Delta T \tag{3.51}$$

with k being the effective conductivity. They then check for solutions, which depends on k, in relation to MEP. This approach is used in several studies (Lorenz et al., 2001; Kleidon, 2004, 2009) applying two-box blackbody systems like the one seen in figure 3.4.

Figure 3.5 shows the corresponding heat flux, ζ, the temperature difference, ΔT, and entropy production, $\dot{S}$, as the conductivity, k, varies between 0 and 100$Wm^{-2}K^{-1}$. Each value of k corresponds to a steady state for the two-box climate system. The entropy produced is a result of two competing processes; the horizontal heat flux and the temperature gradient between the boxes. Changes in one of them (i.e. ζ or ΔT) alters the other.

Having k=0 $Wm^{-2}K^{-1}$ gives ζ=0, making the entropy production, $\dot{S}$, zero. This state corresponds to a state of radiative equilibrium for each box separately. For k=100 $Wm^{-2}K^{-1}$, the heat flux erases the temperature gradient, resulting in ΔT=0, which also makes the entropy production zero. This state corresponds to a state of thermal equilibrium in the system. The state of our two-box climate system is somewhere in between those two extreme states of radiative and thermal equilibrium.

The entropy production exhibits a maximum at k$\simeq 2Wm^{-2}K^{-1}$(figure 3.6(b)) and it is this steady state the MEP theory predicts for our two-box climate system to evolve towards.

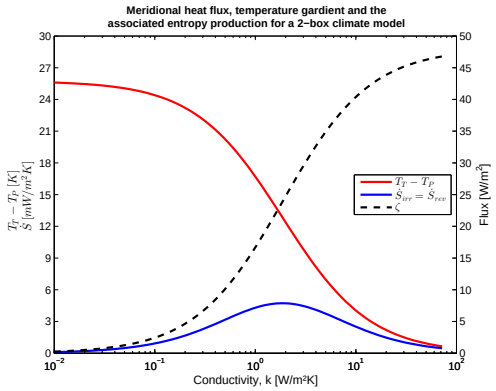

Figure 3.5: A number of possible steady states for the two-box climate system and the corresponding heat flux, ζ, (black, dashed line and right y-axis), the temperature difference, ΔT (red, solid line and left y-axis) and the associated entropy production,$\dot{S}$, (blue, solid line and left y-axis) for each steady state as the conductivity, k, is varied between 0-100$Wm^{-2}K^{-1}$. Each value of k corresponds to a steady state from the two-box climate system. A maximum in the entropy production is seen for k$\simeq 2Wm^{-2}K^{-1}$. The figure is based on work by Kleidon (2004, 2009).

Figure 3.6(a) shows the temperatures for the two boxes and the meridional heat flux as the two-box climate system evolves to a steady state. The system is in a non-equilibrium state since the temperature gradient is maintained. As the system reaches the steady state the entropy produced within the system equals the entropy exported to the surroundings resulting in a constant entropy in the system (see figure 3.6(b)). The entropy in the surroundings (i.e. the universe) still increases, fulfilling the second law of thermodynamics.

Lorenz et al. (2001) used the same method to study the atmospheres of Titan, Mars and Earth. They found the mean conductivity of the meridional heat transfer in the Earth's atmosphere to be in the range of 0.7-2.6$Wm^{-2}K^{-1}$ which is in line with the findings in Kleidon (2004, 2009).

We will later on show that the linear parametrization approach used in Lorenz et al. (2001); Kleidon (2004, 2009) only is valid for small temperature differences.

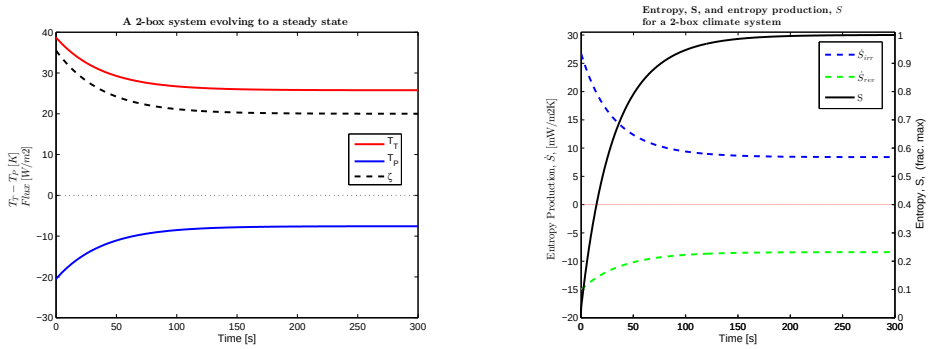

(a) (b)

Figure 3.6: The system reaching one of the possible steady states seen in figure 3.5. (a) Temperature and flux evolving in time for a system with conductivity k = 0.6 $Wm^{-2}K^{-1}$. The difference in the temperature in the tropics box (red, solid line) and the temperature in the polar box (blue, solid line) stabilizes, as the steady state is reached. A constant ΔT corresponds to constant heat flux (black, solid line).(b) Associated entropy production, entropy exportation and entropy for the system in (a). As the climate system reaches the steady state, the entropy production within the system (blue, dashed line) equals the net export of entropy from the system to the surroundings (green, dashed line) and consequently a constant entropy (black, solid line) within the system is obtained. The figure is based on work by Kleidon (2004, 2009).

Chapter 4

Paltridge's MEP Model

The first climate model based on the MEP principle was published by G. W. Paltridge in 1975 (Paltridge, 1975) and developed further in 1978 (Paltridge, 1978). Paltridge used a 10 box zonally averaged energy balance model and solved for 4 unknowns; the meridional heat flux, the surface temperature, the cloud cover and the vertical flux of sensible and latent heat. The results were remarkable. The model was later extended to include 20 boxes (Paltridge et al., 2007) and it is this model that will be discussed throughout this chapter.

Paltridge's model is based on two broad thermodynamical constraints; the maximization of the entropy produced in the system and the maximization of the vertical flux of sensible and latent heat from the surface to the atmosphere.

O'Brien and Stephens (1995) published an article where they described a method for solving the system of equations used in Paltridge's MEP model. The derivations made are to a great extent analytical and the method is easy to use. O'Brien and Stephens (1995) also proved that only one single MEP state solution exists.

Many of the MEP climate models used later on are based on Paltridge's model and provide the same results (Grassl, 1981; Wyant et al., 1988; Pujol and Llebot, 1999, 2000a,b). Since the MEP principle turned out to be difficult to prove, Paltridge's results are often used to demonstrate the exceptional prediction properties of the MEP principle for the climate on Earth.(Kleidon, 2009; Ozawa et al., 2003).

In this chapter Paltridge's MEP model (Paltridge, 1975, 1978; Paltridge et al., 2007) and Stephens and O'Brien's calculations (O'Brien and Stephens, 1995) are explained in detail and the model results are shown. Paltridge's model is a complex ebm and some of the calculations made can be difficult to grasp. They are discussed more in detail in the subsequent chapters. A sensitivity test of all the parameters used is included, followed by a conclusion regarding the suitability of Paltridge's model in a model intercomparison with CAM3.

4.1 Paltridge's MEP model

4.1.1 The overall model

Paltridge's MEP model is a 20-box energy balance model where each box represents the zonal mean condition of a latitude zone. Each box is divided into an atmosphere layer and a surface layer for which energy balance is assumed for each layer separately. All of the boxes have equal surface area. The adjacent boxes cover the globe, from the South Pole to the North Pole. The only transport between the boxes is the meridional heat flux (see figure 4.1). In addition to the horizontal flux, there are fluxes of radiation and convective heat within each box.

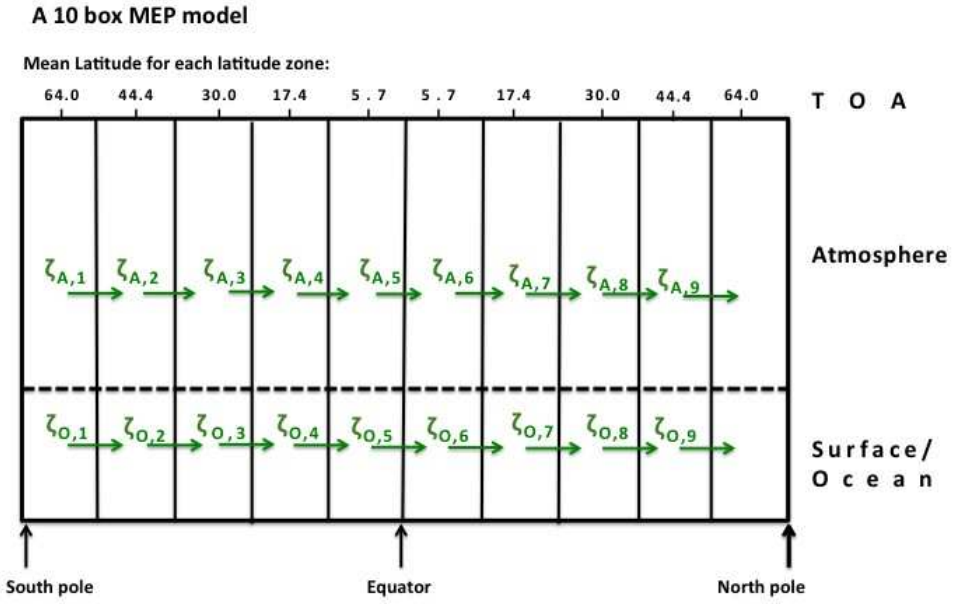

Figure 4.1: A 10 box conceptual MEP model. Each box represents one latitude zone and is divided into an atmosphere and a surface layer. There are 20 boxes in Paltridge's MEP model. Only 10 boxes are shown for the illustration. ζ_A and ζ_o are the atmospheric and the oceanic components of the normalized meridional heat convergence defined in section 4.1.2

4.1.2 The individual box

The solar radiation budget for one zonal latitude zone

Figure 4.2 shows the solar radiation budget for one latitude zone. The incoming solar flux at TOA is $F_0\xi$, where F_0 is the solar constant and $\xi = \pi/cos(\phi)$

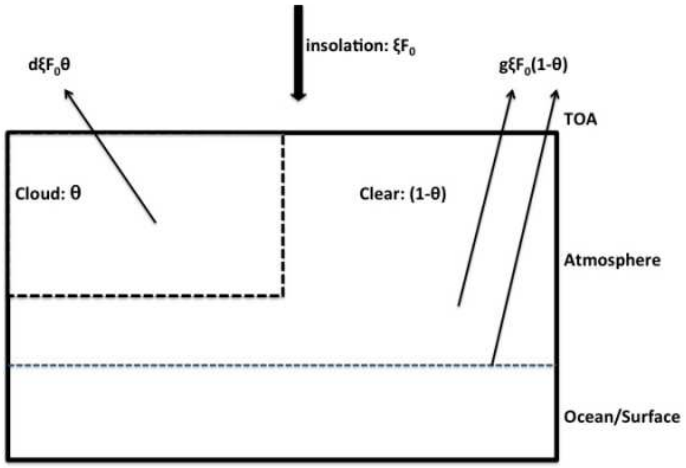

Figure 4.2: The solar radiation budget for one latitude zone. F_0 is the solar constant, $\xi = \pi/cos(\phi)$ and $F_0\xi$ = I, where I is the measured insolation at TOA, g is the planetary albedo in clear sky conditions (1-θ) and d is the planetary albedo in cloudy conditions (θ). See table 3.1 for exact values used in the model.

is the ratio of the actual surface area, at a latitude ϕ, to the projected area seen by the sun. The planetary albedos for clear and cloudy sky are g and d, respectively. The cloud fraction of a latitude zone is θ and the clear sky fraction is $(1-\theta)$.

The net solar flux at TOA,$F_{SW}(TOA)$, is the incoming solar flux minus the reflected solar flux and can be written as

$$F_{SW}(TOA) = F_0\xi - F_0\xi(1-\theta)g - F_0\xi\theta d = F_0\xi\big(1-g-\theta\big(d-g\big)\big)$$
$$= F_0\big(A - B\theta\big) \tag{4.1}$$

where $A = \xi\big(1-g\big)$ and $B = \xi(d-g)$.
The planetary albedo for clear sky, g, and cloudy sky, d, at TOA are defined as

$$g = g_0 + \alpha(1-g_0-k)(1-g_0) \tag{4.2}$$
$$d = d_0 + \alpha(1-d_0-kc)(1-d_0) \tag{4.3}$$

where g_0 and d_0 are the fractional atmospheric reflection in clear and cloudy sky, α is the surface albedo and k and k_c are the fractional solar absorption by clear and cloudy sky, respectively.

The net solar flux at the surface, $F_{SW}(0)$, is the net incoming solar flux minus the reflected solar flux from the atmosphere and the surface and the solar radiation absorbed by gasses in the atmosphere and by liquid water in clouds. The solar flux at the surface can be written as

$$
\begin{aligned}
F_{SW}(0) &= F_0\xi - F_0\xi(1-\theta)g_s - F_0\xi\theta d_s - F_0\xi k(1-\theta) - F_0\xi k_C\theta \\
&= F_0\xi\big(1-(g_s+k)-\theta\big(d_s+k_c-(g_s+k)\big)\big) \\
&= F_0\big(P-Q\theta\big) \qquad (4.4)
\end{aligned}
$$

where P $= \xi(1-(g_s+k))$ and $Q = \xi(d_s+k_c-(g_s+k))$. The fractional reflection and absorption of the atmosphere are defined as

$$g_s + k = 1 - (1-\alpha)(1-g_0-k) \qquad (4.5)$$

$$d_s + kc = 1 - (1-\alpha)(1-d_0-kc) \qquad (4.6)$$

which is the fraction of incoming solar radiation (which is 1) minus the fraction of solar radiation absorbed by the surface.

The longwave radiation budget for one zonal latitude zone

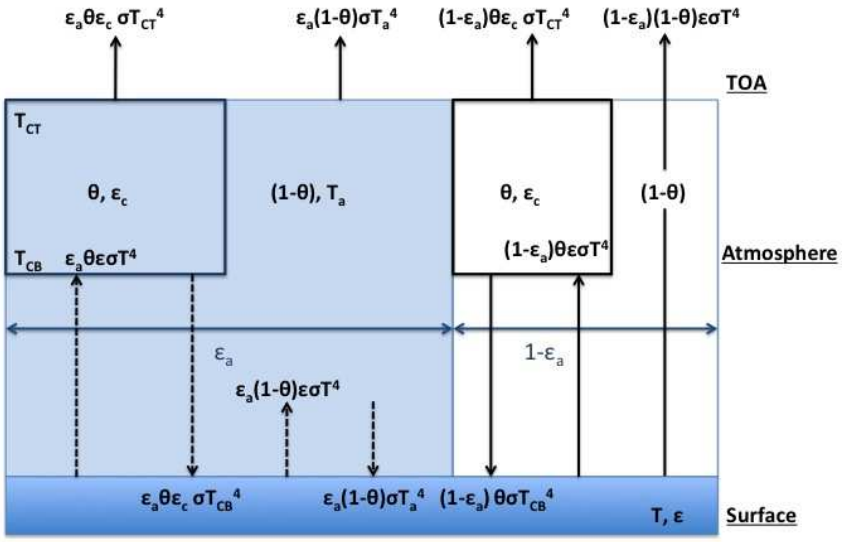

Figure 4.3: Longwave radiation budget for one zonal latitude zone. The figure shows the longwave radiation exchange between the surface, the atmosphere and space in the model. There are two bands, one 100% opaque with width ϵ_a and one 100% clear with width 1-ϵ_a. The squares represent the cloud covered area of the atmosphere, θ. The clear sky areas have a width 1-θ. T, T_a, T_{CB} and T_{CT} are the surface temperature, the atmospheric radiative temperature, the cloud base temperature and the cloud top temperature, respectively. The surface has a mean emissivity ϵ and the cloud emissivity is ϵ_c

A two band model is used in the longwave spectra of the model (see figure 4.3). One of the bands is 100% opaque and has a width ϵ_a. All the atmospheric clear sky emission and absorption takes place in this band. The other band is regarded 100% clear and has a width $1-\epsilon_a$. The clear band represents the atmospheric window. The atmospheric window, $8.5\mu\text{m} \leq \lambda \leq 12.5\mu\text{m}$ (Paltridge, 1974), is a region where the atmosphere is relatively transparent to longwave radiation. Transmission of radiation between the surface and space can only take place in the cloud free fraction of the clear band and downward radiation will only appear in the presence of clouds. Within the opaque band the absorbing atmospheric gases are regarded as a blanket, radiating upward with a blackbody temperature, T_a, and radiating downward with a blackbody temperature close to the surface temperature, so the net exchange of radiative energy between the surface and the opaque band is assumed to be zero (shown as dashed arrows in figure 4.3).

The net longwave flux at TOA, $F_{LW}(TOA)$, is

$$F_{LW}(TOA) = \epsilon_a\theta\epsilon_c\sigma T_{CT}^4 + (1-\theta)\epsilon_a\sigma T_a^4 + (1-\epsilon_a)\theta\epsilon_c\sigma T_{CT}^4 + (1-\epsilon_a)(1-\theta)\epsilon\sigma T^4 \tag{4.7}$$

To simplify the equations used in this model, the blackbody radiation of the atmosphere, the cloud base and the cloud top are expressed as fractions of the blackbody radiation of the surface

$$F = \frac{\sigma T_a^4}{\sigma T^4} \quad (4.8a) \qquad f' = \frac{\sigma T_{CB}^4}{\sigma T^4} \quad (4.8b) \qquad f = \frac{\sigma T_{CT}^4}{\sigma T_{CB}^4} \quad (4.8c)$$

Using these simplifications $F_{LW}(TOA)$ can be written as

$$\begin{aligned} F_{LW}(TOA) &= ff'\theta\epsilon_c\sigma T^4 + \epsilon_a(1-\theta)F\sigma T^4 + (1-\epsilon_a)(1-\theta)\epsilon\sigma T^4 \\ &= \sigma T^4\big(\epsilon_a F + \epsilon(1-\epsilon_a) - \theta\big(\epsilon_a F + \epsilon(1-\epsilon_a) - \epsilon_c f f'\big)\big) \\ &= \sigma T^4\big(C - D\theta\big) \end{aligned} \tag{4.9}$$

where $\mathrm{C} = \epsilon_a F + \epsilon(1-\epsilon_a)$ is the fractional atmospheric emission in clear sky plus the fractional surface emission attenuated by atmospheric absorption, and $\mathrm{D} = \epsilon_a F + \epsilon(1-\epsilon_a) - \epsilon_c f f'$ is the fractional longwave emission from clouds.

Assuming no energy exchange between the surface and the atmosphere in the opaque band, the net longwave flux at the surface, $F_{LW}(0)$, is

$$F_{LW}(0) = (1-\epsilon_a)\sigma\epsilon T^4 - (1-\epsilon_a)\theta\epsilon_c\sigma T_{CB}^4 \tag{4.10}$$

Applying the temperature simplifications, i.e. equations 4.8a,b,c, $F_{LW}(0)$ can be written as

$$\begin{aligned} F_{LW}(0) &= (1-\epsilon_a)\sigma\epsilon T^4 - (1-\epsilon_a)\theta f'\epsilon_c\sigma T = \sigma T^4\big(\epsilon(1-\epsilon_a) - \theta\big((1-\epsilon_a)\epsilon_c f'\big)\big) \\ &= \sigma T^4\big(R - S\theta\ \big) \end{aligned} \tag{4.11}$$

where $\mathrm{R}=\epsilon(1-\epsilon_a)$ is the fractional surface emission attenuated by atmospheric absorption and $\mathrm{S}=(1-\epsilon_a)\epsilon_c f'$ is the fraction of downward emission from the cloud base.

The total energy budget for one zonal latitude zone

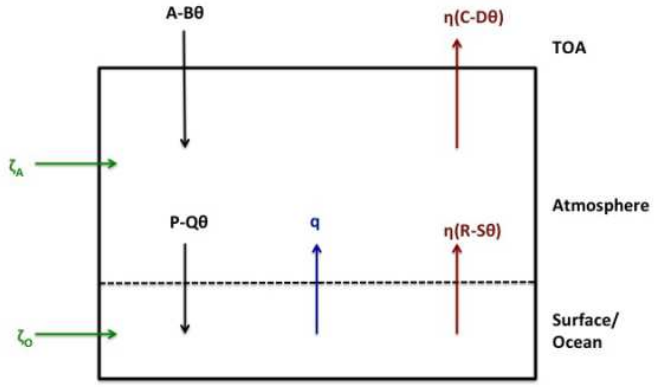

Figure 4.4: The total energy budget for one zonal latitude zone. The black arrows represent solar radiation, the brown arrows represent terrestrial radiation, the blue arrow represents flux of latent and sensible heat and the green arrows represent meridional heat convergence. See table 4.1 for explanation of the constants used.

In addition to radiative fluxes there are fluxes of latent and sensible heat, LE + H, and meridional heat convergence, ΔX, within each box (see figure 4.4). The meridional heat flux has an atmospheric component, ΔX_A, and an oceanic component, ΔX_o, such that $\Delta X = \Delta X_A + \Delta X_o$.

To ease the calculations the fluxes are normalized by the solar constant, F_0

$$\zeta = \frac{\Delta X}{F_0} \quad (4.12a) \qquad \eta = \frac{\sigma T^4}{F_0} \quad (4.12b) \qquad q = \frac{LE + H}{F_0} \quad (4.12c)$$

The energy balance for one box is

$$F_0(A - B\theta) - \sigma T^4(C - D\theta) + \Delta X = 0 \quad (4.13a)$$

$$(A - B\theta) - \eta(C - D\theta) + \zeta = 0 \quad (4.13b)$$

The energy balance for the surface layer only is

$$F_0(P - Q\theta) - \sigma T^4(R - S\theta) - (LE + H) + \Delta X_o = 0 \quad (4.14a)$$

$$(P - Q\theta) - \eta(R - S\theta) - q + \zeta_o = 0 \quad (4.14b)$$

where $\zeta_o = \zeta - \zeta_A$ is the oceanic part of the meridional heat convergence.

There are two energy balance equations for each box for which η, q, θ and ζ are the unknowns. To solve the system of equations two more constraints are needed.

4.1.3 The first maximization principle

The first maximization principle used in the model is the maximization of the vertical flux of latent and sensible heat (LE+H) from the ground to the atmosphere. The vertical heat flux is maximized w.r.t. both surface temperature and cloud cover. By using this principle it is possible to get an expression for the surface temperature and the cloud cover that satisfies the energy balance equations and which yields a maximum of LE+H. Assuming that the vertical heat flux exchange occurs on a much shorter timescale than the meridional heat exchange, the two processes are considered independent. The calculations made are based on the work of O'Brien and Stephens (1995).

The cloud faction, θ, can be eliminated from the surface layer equation using the equation for the total box, making the normalized flux of latent and sensible heat, q, a function independent of θ

$$\theta = \frac{\zeta + A - C\eta}{B - D\eta} \;\rightarrow\; q = \zeta_o + (P - R\eta) - (Q - S\eta)\left(\frac{\zeta + A - C\eta}{B - D\eta}\right) \quad (4.15a)$$

Note that η is the normalized blackbody radiation from the surface and a measure of the surface temperature. For that reason η will be referred to as the surface temperature throughout the calculations in this chapter.

The surface temperature can be eliminated in the same way making q a function independent of η

$$\eta = \frac{\zeta + A - B\theta}{C - D\theta} \;\rightarrow\; q = \zeta_o + (P - Q\theta) - (R - S\theta)\left(\frac{\zeta + A - B\theta}{C - D\theta}\right) \quad (4.15b)$$

To find an extreme of q with respect to η and θ, we need to calculate $\partial q/\partial\eta = 0$ and $\partial q/\partial\theta = 0$.
The calculations give the roots

$$D\eta - B = \pm\sqrt{\frac{BS - DQ}{CS - DR}}\sqrt{BC - AD - D\zeta} = \pm H\sqrt{\gamma} \quad (4.16)$$

$$D\theta - C = \pm\sqrt{\frac{CS - DR}{BS - DQ}}\sqrt{BC - AD - D\zeta} = \pm H^{-1}\sqrt{\gamma} \quad (4.17)$$

where H and γ are defined as

$$H = \sqrt{\frac{BS - DQ}{CS - DR}} \quad (4.18)$$

$$\gamma = BC - AD - D\zeta \tag{4.19}$$

To get a realistic solution we need

$$\frac{BS - DQ}{CS - DR} \geq 0 \text{ and } \gamma \geq 0$$

In their article, Stephen and O'Brien (1995) state that BS-DQ>0, CS-DR >0 and γ>0 for realistic parameter values which will guarantee a real solutions. Although this is satisfied for the parameters used in Paltridge's MEP model, it is not always the case (section 4.3).

To see whether the expression for θ and η are maxima or minima we need to calculate $\partial^2 q/\partial\eta^2$ and $\partial^2 q/\partial\theta^2$ at the zeroes of $\partial q/\partial\eta$ and $\partial q/\partial\theta$ respectively. The calculations show that

$$\frac{\partial^2 q}{\partial\eta^2} = \pm 2\frac{CS - DR}{H\sqrt{\gamma}} \tag{4.20a}$$

$$\frac{\partial^2 q}{\partial\theta^2} = \pm 2H\frac{BS - QD}{\sqrt{\gamma}} \tag{4.20b}$$

CS-DR and BS-QD are already assumed to be greater that zero, so to find the two maxima the roots with the negative sign are chosen. Consequently the maximization of vertical convection requires that

$$D\eta - B = -H\sqrt{\gamma} \tag{4.21}$$

$$\theta - C = -H^{-1}\sqrt{\gamma} \tag{4.22}$$

All the radiation constants A, B, C, D, P, Q, R and S are combinations of the parameters used for the zonal latitude zone, which means that both the surface temperature and the cloud fraction are constrained to be functions of the meridional energy convergence.

4.1.4 The second maximization principle

The second maximization principle used in Paltridge's model is the principle of maximization of entropy production. Paltridge defines the entropy production in the ith box to be

$$\mathscr{P}_i = -\frac{\Delta X_i}{T_{a,i}} \tag{4.23}$$

which is the entropy produced due to the meridional energy convergence. $T_{a,i}$ is the radiative temperature of the atmosphere. The total rate of entropy produced is the sum of the entropy production in each box

$$\mathscr{P} = \sum_i \mathscr{P}_i \tag{4.24}$$

The radiative atmospheric temperature, $T_{a,i}$, can be calculated from the OLR terms at TOA (see figure 4.3) for the ith box as

$$\begin{aligned}\epsilon_a \sigma T_{a,i}^4 &= \epsilon_a \epsilon_c f f_i' \theta_i \sigma T_i^4 + \epsilon_a (1-\theta_i) F \sigma T_i^4 \\ &= \epsilon_a \sigma T_i^4 \big(\epsilon_c f f_i' \theta_i + F(1-\theta_i)\big) \end{aligned} \tag{4.25}$$

$$T_{a,i} = \sqrt[4]{\frac{F_0 \eta_i}{\sigma}\big(F - \theta_i (F - \epsilon_c f f_i')\big)} \tag{4.26}$$

Because both η and θ can be expressed in terms of ζ, the atmospheric temperature can be written as

$$T_{a,i} = \left(\frac{F_0}{\sigma}\right)^{\frac{1}{4}} \mathcal{G}_i(\zeta_i)$$

$$\text{where } \mathcal{G}_i(\zeta_i) = \left[\left(\frac{B_i}{D_i} - \frac{H_i\sqrt{\gamma_i}}{D_i}\right)\left(F - \left(\frac{C_i}{D_i} - \frac{\sqrt{\gamma_i}}{H_i D_i}\right)\big(F - \epsilon_c f f_i'\big)\right)\right]^{\frac{1}{4}} \tag{4.27}$$

Note that $\mathcal{G}_i$ is a function of ζ_i alone and does not depend on other ζ_j, $j \neq i$.

Let $\mathscr{Q}$ denote the normalized entropy production

$$\mathscr{Q} = \frac{\mathscr{P}}{F_0^{\frac{3}{4}} \sigma^{\frac{1}{4}}} = \frac{1}{F_0^{\frac{3}{4}} \sigma^{\frac{1}{4}}} \sum_i \frac{\Delta X_i}{\tilde{T_{a,i}}} = \sum_i \frac{\zeta_i}{\mathcal{G}_i(\zeta_i)} \tag{4.28}$$

which is maximized subject to the constraint

$$\sum_i \zeta_i = 0 \tag{4.29}$$

which states that since the climate system is assumed to be in a steady state, no heat can be stored within the system.

The method of Lagrange multipliers, described in section 3.2.6, is used to solve this problem . Let $\mathscr{L}$ be the Lagrangian cost function and β the Lagrangian multiplier, then

$$\mathscr{L} = \mathscr{Q} - \beta \sum_i \zeta_i = \sum_i \left(\frac{\zeta_i}{\mathcal{G}_i(\zeta_i)} - \beta \zeta_i\right) \tag{4.30}$$

The constrained maximum of $\mathscr{Q}$ can be found by solving for the maximum of $\mathscr{L}$ with respect to β and ζ_i

$$\frac{\partial \mathscr{L}}{\partial \beta} = -\sum_i \zeta_i = 0 \tag{4.31}$$

$$\frac{\partial \mathscr{L}}{\partial \zeta_i} = \frac{1}{\mathcal{G}_i} - \frac{\zeta_i}{{\mathcal{G}_i}^2} \frac{d\mathcal{G}_i}{d\zeta_i} - \beta = 0 \tag{4.32a}$$

Equation 4.31 is the energy constraint already assumed to be true.

To get the MEP state we need to solve the non-linear equation

$$\zeta_i \frac{d\mathcal{G}_i}{d\zeta_i} - \mathcal{G}_i + \beta {\mathcal{G}_i}^2 = 0 \tag{4.32b}$$

for each zonal latitude zone in the model. The equation is solved numerically and the solution obtained is proved to be unique by Stephens and O'Brien (O'Brien and Stephens, 1995).

In the 2007 version of the MEP model (Paltridge et al., 2007), Paltridge also includes a tuning parameter of the atmospheric temperature, z_0. The use of the radiative atmospheric temperature to calculate the entropy production results in values that are too small for the meridional energy convergence, ζ (Paltridge, 1975, 1978). To compensate for this, a tuning factor, which increases the atmospheric temperature and hence alters the entropy production and the solution, is included, i.e. $T_{a,i} = z_0 T_{a,i}$, where $z_0 = 1.07$.

Since all boxes are defined to have the same surface area, the meridional heat transport is calculated as

$$F_\phi = \frac{4\pi R_E^2}{20} \int_{-\frac{\pi}{2}}^{\frac{\pi}{2}} \zeta(\phi) \mathrm{d}\phi \tag{4.33}$$

where R_E is the radius of the Earth, ϕ is the mean latitude for the box and $\mathrm{d}\phi$ is the horizontal width of each box. The fraction $4\pi R_E^2/20$ is the mean surface area of each box.

4.1.5 The results from Paltridge's MEP model

The results from Paltridge's MEP model are shown in figure 4.5 (blue, solid line). Also included are control run results from CAM3 (black, solid line). Given its simplicity, the MEP model results are quite impressive.

The results from the MEP model are more zonally symmetric about the equator than the data used in the comparison. The parameters used in Paltridge model are weighted by the appropriate land/sea fraction for the given latitude zone, although it seems like the differences are not captured properly when compared to surface temperatures in CAM3.

The surface temperature comparison is remarkable (figure 4.5(a)). The only place where the surface temperatures from the MEP model do not follow

Name	Value	Represents
I	*	The mean insolation
g_0	*	The atmospheric albedo in clear sky
d_0	*	The atmospheric albedo in cloudy sky
α	*	The surface albedo
ϵ	*	The surface emissivity
f'	*	The ratio T_{CT}^4/T_{CB}^4
k	*	The fractional atmospheric absorption in clear sky
k_c	0.20	The fraction of atmospheric absorption in cloudy sky
F	0.55	The ratio Ta^4/T^4
f	0.80	The ratio T_{CB}^4/T^4
ϵ_a	0.75	The atmospheric clear sky emissivity
ϵ_c	1.00	The cloud emissivity
z_0	1.07	The tuning factor for the atmospheric temperature
SW:	All constants are fractional values of F_0	
A	$\xi(1-g)$	Net solar flux at TOA in clear sky
B	$\xi(d-g)$	Net solar flux at TOA in cloudy sky
P	$\xi(1-(g_s+k))$	Net solar flux at the surface in clear sky
Q	$\xi(d_s+k_c-(g_s+k))$	Net solar flux at the surface in cloudy sky
LW:	All constants are fractional values of $F_0\eta$	
ma	$\epsilon_a F$	fractional atmospheric emission in clear sky
mg	$\epsilon(1-\epsilon_a)$	fractional surface emission attenuated by atmospheric absorption
mc	$\epsilon_c f f'$	fractional upward emission from cloud top
nc	$\epsilon_c f'(1-\epsilon_a)$	fractional downward emission from cloud base
C	ma + mg	Net longwave flux at TOA in clear sky
D	ma + mg - mc	Net longwave flux at TOA in cloudy sky
R	mg	Net longwave flux at the surface in clear sky
S	nc	Net longwave flux at the surface in cloudy sky
Other:		
$\tilde{T}_a$	$\sqrt[4]{\frac{F_0\eta_i}{\sigma}\left(F-\theta_i(F-\epsilon_c f f_i')\right)}$	the radiative temperature of the atmosphere used to calculate the production of entropy

Table 4.1: The different parameters and radiation constants used in Paltridge's MEP model. All parameters are weighted by the appropriate land/sea fraction of the given latitude zone. * values listed in Table 4.2

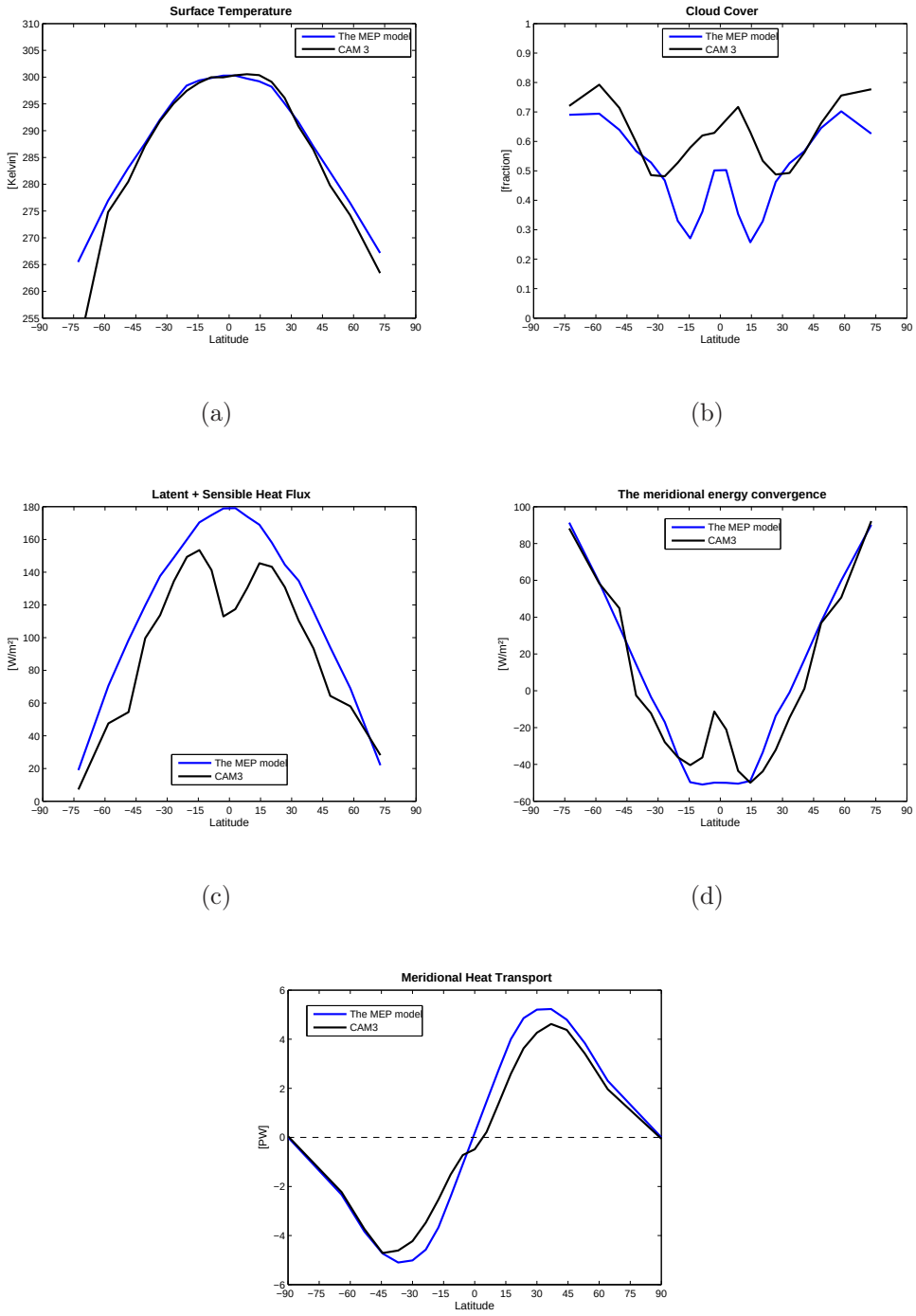

Figure 4.5: The results from Paltridge's MEP model (blue, solid lines). (a) Surface Temperature, (b) The Cloud Cover, (c) The Convective Heat Flux, (d) The Meridional Heat Convergence, ζ, (e) the Meridional Heat Transport, F_ϕ. Results from CAM3 (black, solid lines) are also included.

Lat.	I, W/m^2	g_0	d_0	α, SH	α, NH	f'	ϵ, SH	ϵ, NH	k, SH	k, NH
72.8°	186	0.130	0.57	30	25	0.80	0.99	0.99	0.1468	0.1880
58.4°	242	0.095	0.43	7.3	9.8	0.80	0.99	0.98	0.1877	0.1866
48.7°	288	0.080	0.39	6.2	10.4	0.80	0.99	0.98	0.1896	0.1859
40.6°	324	0.070	0.37	6.1	9.3	0.80	0.99	0.98	0.1898	0.1832
33.4°	355	0.060	0.35	6.7	9.6	0.78	0.99	0.97	0.1887	0.1814
26.8°	376	0.055	0.34	7.8	10.8	0.75	0.98	0.97	0.1868	0.1835
20.5°	393	0.050	0.33	8.3	9.8	0.71	0.98	0.97	0.1859	0.1841
14.5°	406	0.047	0.32	7.5	8.3	0.70	0.99	0.99	0.1873	0.1821
8.6°	413	0.045	0.31	7.4	7.9	0.70	0.99	0.99	0.1875	0.1832
2.9°	420	0.045	0.30	7.2	7.1	0.70	0.99	0.99	0.1878	0.1558

Table 4.2: Parameter values used in Paltridge's MEP model. The Lat column represents the mean latitude of the zonal latitude zone. What the other parameters represents are explained in Table 4.1

the CAM3 data, is near Antarctica, where the surface temperatures are extremely cold.

Perhaps the most fascinating result of Paltridge's MEP model is the cloud cover fraction (figure 4.5(b)). This is especially true since the cloud cover fraction is a function of the meridional energy convergence and is based on a not well known principle: the principle of maximum convection. A comparison with CAM3 is not straightforward since there are great uncertainties associated with cloud cover data in GCMs in general, but the main features of the cloud cover are captured in a satisfactory way. The local maxima in the cloud cover fraction at the equator, associated with the ITCZ, and at mid latitudes, due to storms, are seen. Also seen are the two minima in the cloud cover, associated with the descending branches of the Hadley circulation.

The flux of latent and sensible heat is greater and smoother compared to the CAM3 result. The local minimum in the latent heat flux at the equator is not captured in the MEP model (figure 4.5(c)) . This may not be too surprising since the reasons for this minimum are complex.

Also the meridional heat convergence and the meridional heat transport resembles the CAM3 results (figure 4.5(d)-(e)). Note that the meridional heat convergence and the transport, calculated from CAM3 data (see chapter 2 for details), are only the atmospheric components and hence smaller compared to results from a fully coupled climate model.

4.2 A sensitivity test of Paltridge's MEP model

Lord Kelvin once said: *With three parameters, I can fit an elephant.* Paltridge is using thirteen parameters in his model. If you can fit an elephant using

three parameters, imagine what you can do using thirteen! One of the main questions asked in this thesis is if a MEP model is able to capture shifts in the meridional heat transport in response to altered SST. In trying to answer this question, it is essential to know if the accurate model results are a consequence of good parameter choices, or if the model actually is capable of capturing the main features of our climate. Therefore, to get a better understanding of Paltridge's MEP model, a sensitivity test of the parameters is included and discussed.

4.2.1 The sensitivity test

There are thirteen parameters in Paltridge's MEP model, but only twelve of them are tested. The cloud emissivity is assumed to equal 1 in all the calculations. Changing it would mean changing the equations used in the model, which is not in our interest. It is arguable whether the cloud emissivity even is a parameter at all in this model.

Each of the twelve remaining parameters have been tested separately, so while altering one parameter value (or values if the parameter value changes with latitude) the others remain unchanged. How much it is possible to change the value(s) differs from one parameter to another. Changes that are too big either cause complex solutions or unrealistic cloud cover fraction for which, $\theta < 0$ or $\theta > 1$, and these results are not included.

4.2.2 The sensitivity test results

Figure 4.6 and 4.7 show the results of the sensitivity test. The test results are presented as fractional changes in the global mean values of the solutions from the perturbed MEP model run to the global mean values of the solution from the original run. The solution presented from the MEP model includes the cloud cover (black, solid line), the surface temperature (dark blue, solid line), the convective heat flux, H+LE, (light blue, solid line) and the meridional heat transport for the Southern hemisphere (red, dashed line) and for the Northern hemisphere (green, dashed line). The y-axis is the mean fractional change in the MEP model solutions relative to the original run. The x-axis is the fractional change in the parameter value(s) relative to the original value(s). The point (1,1) represents the original run.

The mean surface temperature is not very sensitive to parameter changes. There are hardly any changes seen at all except for altered insolation (see figure 4.6(a)). Also the mean value of the vertical flux of sensible and latent heat, H+LE, does not exhibit any great changes, except for changes in the surface albedo (figure 4.6(f)) and changes in the surface emissivity (figure 4.7(a)). The meridional heat transport shows higher parameter dependency than what is seen for both the surface temperature and the convective heat flux. High values are especially seen for the longwave radiation parameters

F, f, f' and z_0 (figure 4.6(b) and (e) and figure 4.7(e) and (f))

What really stands out though are the large changes in the cloud cover fraction as a response to parameter changes. This is true for nearly all of the parameters and shows that the cloud cover acts as the main contributor in restoring energy balance within each box. E.g. if a box gains too much energy, an increased cloud cover fraction will increase the albedo for which a smaller amount of solar radiation is absorbed, resulting in a new the energy balance state in the box. As a response to this, O'Brien and Stephens (1995) wrote in their article: *If so, the best procedure for modeling clouds in a general circulation model (GCM) might be to introduce them as regulating elements, rather than to attempt to predict cloud condensation nuclei, water vapor, entrainment and all the microphysics of cloud formation.* Using a simple energy balance model does not provide many ways to restore energy balance. An adjustment of the cloud cover is one of very few options. To suggest that the clouds on Earth act in order to restore energy balance, is probably an overstatement.

The main conclusions drawn from this test is that the cloud cover fraction acts as the restoring energy balance force and as a consequence small changes in the parameters cause huge changes in the cloud cover. This is a characteristic of the MEP model and not necessarily a negative one, but it is very important keep in mind of when the proper use of Paltridge's MEP model is considered. A further discussion of this is included in the last section of this chapter.

A comment on how to present the sensitivity test results

Most of the sensitivity tests done on Paltridge's model (Grassl, 1981; Pujol and Llebot, 1999, 2000a) use the ratio of changes in the global mean value. The same is done in figure 4.6 and 4.7. This way of presenting the results does not give the full picture. The results can change quite substantially due to parameter changes without changing the global mean value of the results. One example is the sensitivity test of the atmospheric tuning factor, z_0. Figure 4.8(a) shows that the global mean value of the cloud cover fraction (black, solid line) does not change much as z_0 changes. Figure 4.8(b) gives a different picture. Huge changes occur in the cloud cover fraction with up to 80% increase in the tropics and up to 40% decrease at high latitudes. Since there are both great increases and decreases of the cloud cover happening for the same parameter change, the mean global value stays almost the same as in the original run.

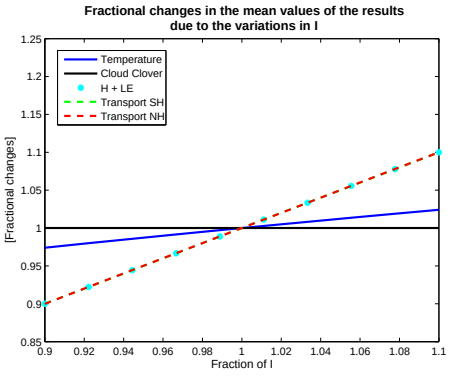

(a) I: insolation at TOA

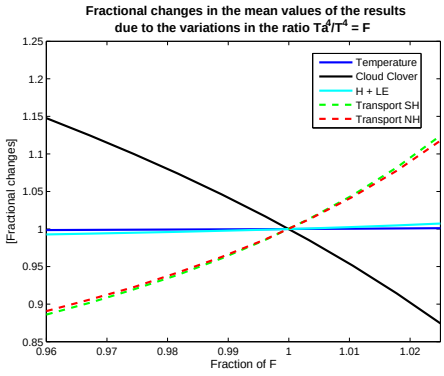

(b) F: ratio Ta^4/T^4

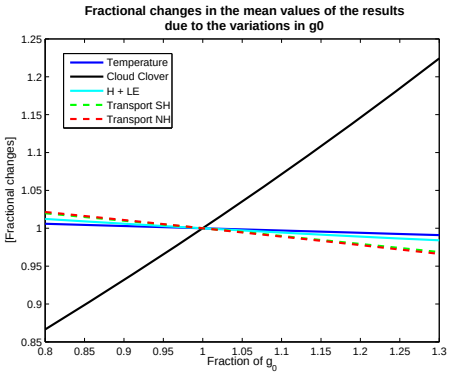

(c) g0: atmospheric albedo, clear

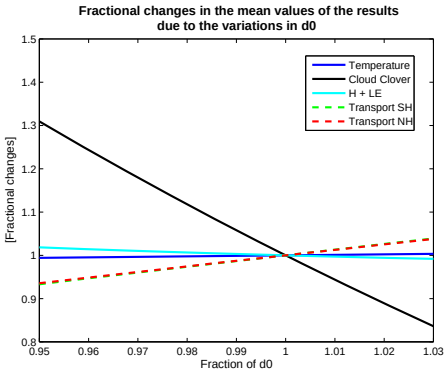

(d) d0: atmospheric albedo, cloudy

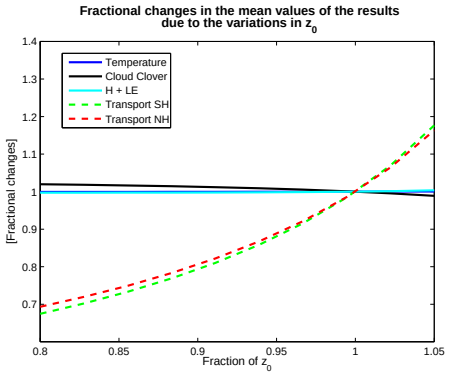

(e) z_0: tuning factor for Ta

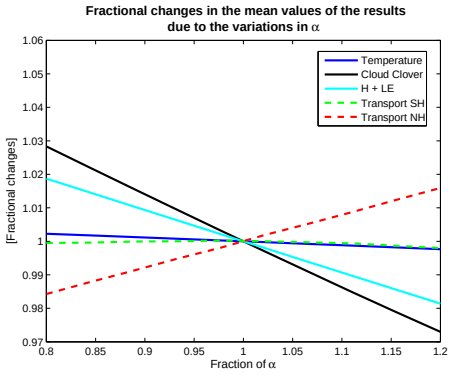

(f) α: surface albedo

Figure 4.6: The sensitivity test of the parameters used in Paltridge's MEP model. The figures show the fractional changes in the MEP model global mean results relative to the global mean results from the original run which are: The Cloud Cover (black, solid line), The Surface Temperature (dark blue, solid line), The Convective Heat Flux, H+LE, (light blue, solid line), The Meridional Heat Transport for the Southern hemisphere (red, dashed line) and for the Northern hemisphere (green, dashed line).

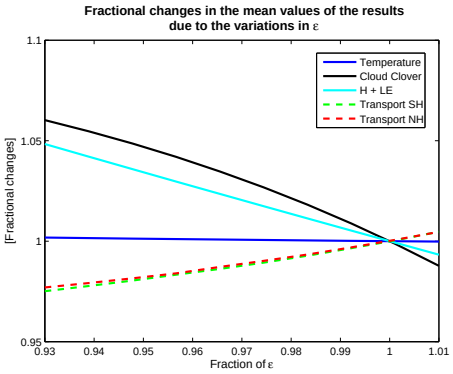

(a) ϵ: surface emissivity

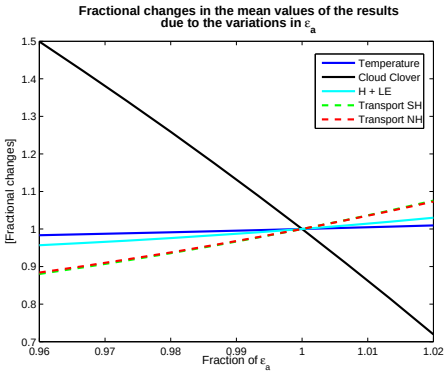

(b) ϵ_a: atmospheric emissivity

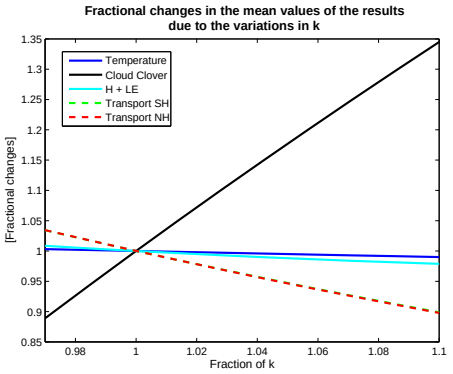

(c) k: atmospheric absorption, clear

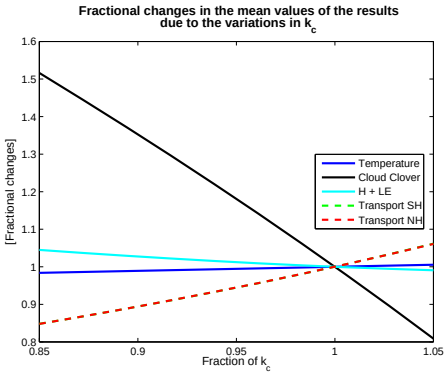

(d) k_c: atmospheric absorption, cloudy

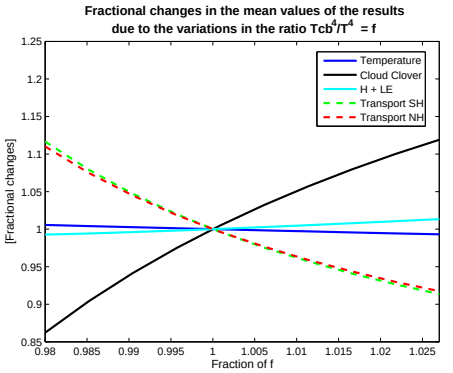

(e) f: ratio Tcb^4/T^4

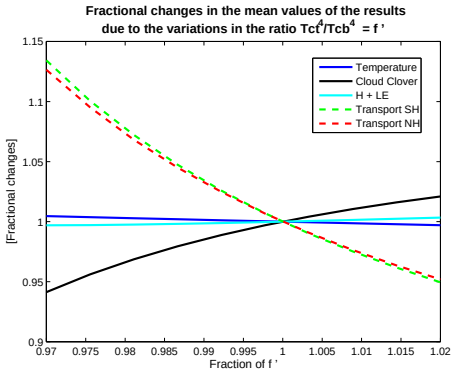

(f) f': ratio Tct^4/Tcb^4

Figure 4.7: The sensitivity test of the parameters used in Paltridge's MEP model. The figures show the fractional changes in the MEP model global mean results relative to the global mean results from the original run which are: The Cloud Cover (black, solid line), The Surface Temperature (dark blue, solid line), The Convective Heat Flux, H+LE, (light blue, solid line), The Meridional Heat Transport for the Southern hemisphere (red, dashed line) and for the Northern hemisphere (green, dashed line).

On the other hand, including 60 sensitivity figures such as figure 4.8(b) in order to give the complete picture is not a good option either. The sensitivity test of the cloud cover due to changes in z_0 is an extreme case and most of the changes are captured in a satisfactory way by figure 4.6 and 4.7. For this reason the global mean value is chosen, with a gentle warning.

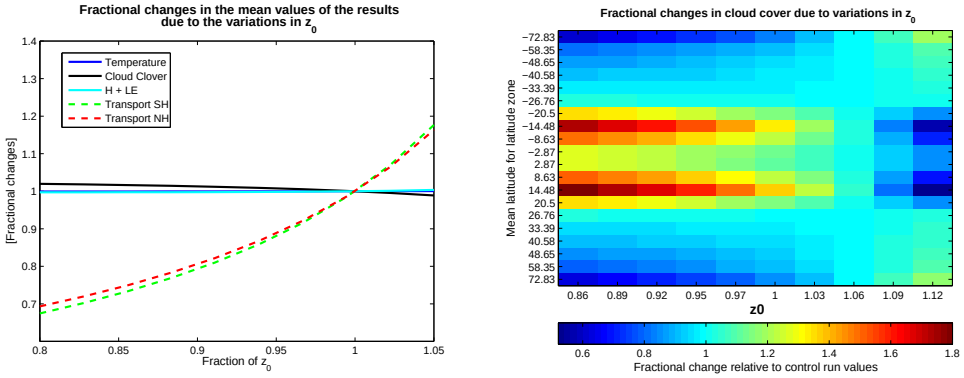

(a) (b)

Figure 4.8: Sensitivity test of the tuning factor of the atmospheric temperature, z_0. The figures show the fraction of changes in the cloud cover relative to the original run. (a) Fractional changes in the global mean value of the cloud cover (black, solid line) does not change much, but great zonal changes in the cloud cover fraction still occur as seen in (b).

4.3 The radiation constants

The sensitivity test provides interesting information about changes in the results as a consequence of changes in the parameters, but cannot say anything about the parameter value(s) chosen in the first place. It is difficult to tell if the values used in Paltridge's MEP model are reasonable. Some disregard Paltridge's MEP model due to his parameter definitions (Martyushev and Seleznev, 2006) and maybe they do so for good reasons. A parameter like the fraction of the OLR from the cloud top to the OLR from the surface (i.e. $f \cdot f'$) is not straightforward to calculate.

The radiation constants used, (i.e. A, B, C...etc. See figure 4.10 for details) which are combinations of the parameters, are easier to handle. Net flux data at TOA and the surface from CAM3 are used to calculate the same constants. E.g. $A = F_{SW,clear}(TOA)/F_0$, where $F_{SW,clear}(TOA)$ is the net solar flux at the top of the atmosphere for clear sky conditions.

The constants calculated from CAM3 will not necessarily denote the same physical properties as in the MEP model, but will represent the same fractional radiation flux. For instance, S represents the fractional downward

radiation flux from the cloud base in the clear band in the MEP model and is the net longwave flux between the atmosphere and the surface under cloudy conditions as a fraction of the black body radiation emitted by the surface. The S calculated from CAM3 will also represent the net longwave flux at the surface under cloudy conditions and is given as a fraction of the black body radiation emitted by the surface, but is not only the downward radiation from the cloud base since the radiation exchange processes in CAM3 are much more complex.

The results are shown in figures 4.9 and 4.10. The MEP results are shown as solid lines while the dashed lines are the CAM3 results. The H defined in equation 4.18 can be seen in figure 4.9. H is real for the parameters used in the MEP model, but complex at low and middle latitudes as a result of CS-DR < 0 for the CAM3 data, contrary to the assumptions made when H was defined.

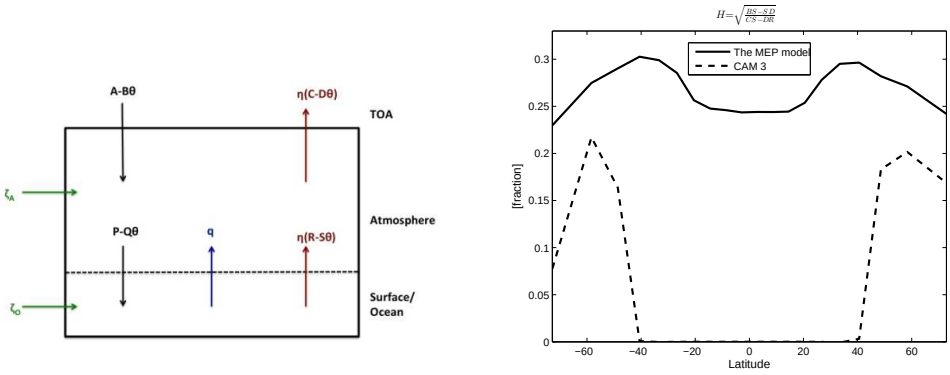

(a) (b)

Figure 4.9: (a) Schematic showing the radiation constants described in the text. The figure shows the total energy budget for one box in Paltridge's MEP model. (b) H is defined as $\sqrt{\frac{BS-DQ}{CS-DR}}$ and represents no physical quantity. H is complex in CAM3 at low latitudes due to CS-DR < 0.

Figure 4.10(a) shows the annual-mean absorbed solar radiation at TOA. Paltridge's MEP model represents the absorbed solar radiation well. The radiation constants representing the solar flux fractions are also similar in the two models (figure 4.10(c) and (d)), especially the clear sky values, A and P.

Figure 4.10(b) shows the emitted longwave radiation at TOA. The MEP model overestimates the OLR for all latitudes and at equator in particular, compared to CAM3. The most striking feature is the constant values used for the fractional

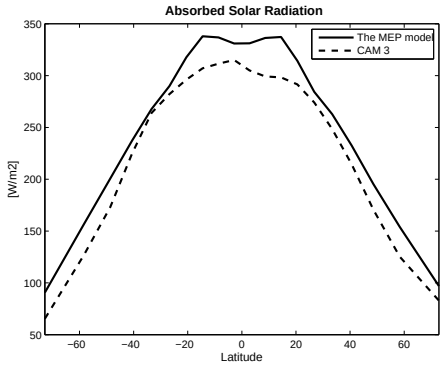

(a) Absorbed Solar Radiation

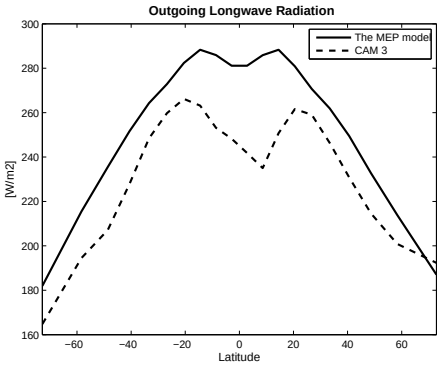

(b) OLR

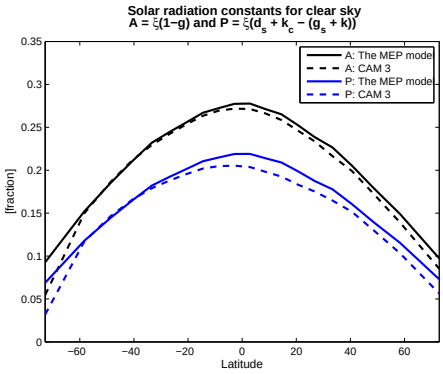

(c) A and P: Net solar flux in clear sky at TOA and at the surface, respectively.

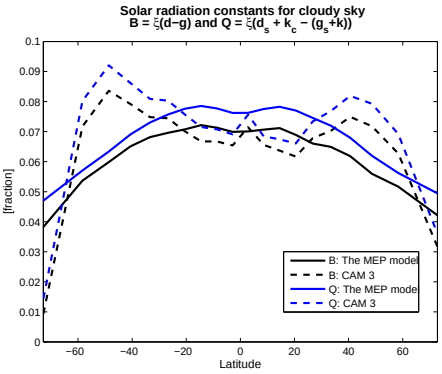

(d) B and Q: Net solar flux in cloudy sky at TOA and at the surface.

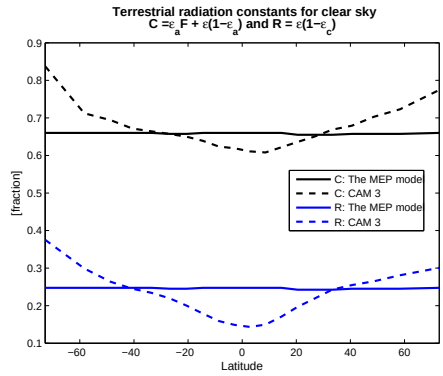

(e) C and R: Net longwave flux in clear sky at TOA and at the surface.

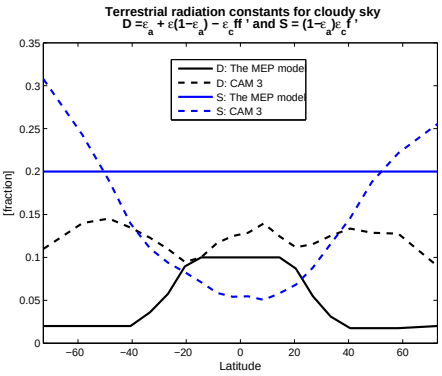

(f) D and S: Net longwave flux in cloudy sky at TOA and at the surface.

Figure 4.10: A comparison of the radiation constants (see figure 4.4 and text for details) used in the MEP model and the ones calculated from CAM3 data. The shortwave and longwave constants are fractional values of F_0 and $F_0\eta$ respectively

longwave fluxes in the MEP model (see figure 4.10(e) and (f)). Zonal variations in the longwave radiation fluxes are expected, especially for cloudy conditions. It is for cloudy conditions that the MEP model shows the greatest difference from CAM3.

The parameters used in the MEP model capture the solar fluxes much better than the longwave fluxes. Extinction of solar radiation in the atmosphere can be described by a simple exponential function (Beer's law) while it gets much more complicated in the longwave spectra since both absorption and emission processes are occurring simultaneously. As a result, solar fluxes are in general much easier to parametrize than longwave fluxes, as seen for the radiation constants used in the MEP model.

4.4 Conclusions

The results from Paltridge's MEP model are impressive, but the underlying causes of these results are not clear. A fair question to ask is if Paltridge's results are *a lucky accident* (Dewar, 2009) and actually a consequence of good parameter choices more than a demonstration of exceptional MEP predictions? Without a clear answer to this question, it is hard to justify the further use of his model.

Another problem is that Paltridge's model has an active surface layer, whereas CAM3 is an atmosphere-only model. Further comparisons require a more simplified model. This model is developed in the subsequent chapters. Such a model requires that the surface temperature, which will be prescribed, is decoupled from the atmospheric temperature. In Paltridge's model the atmospheric temperature is fixed to the surface temperature through the parameter F. Thus, setting the surface temperature determines the atmospheric temperature. This is undesirable when testing a sensitivity to SST.

The sensitivity tests show that the cloud fraction is the main restoring force in the MEP model. This is probably not the case in CAM3 for which the cloud cover fraction only shows small changes (see figure 9.3) between the different SST runs. Also the use of twelve parameters is in itself a problem. All the parameters used make it hard to distinguish the good from the bad in this model. Using a model which is not fully understood is not a desirable option.

The next two chapters examine the process of building an AMEP model. It is desirable to fully understand the AMEP model, so the aim is to make it as simple as possible. To do that, we start out with a very simple model and then add complexity. The simplest MEP model possible is a two-box MEP model, so we start with that.

Chapter 5

Two-box MEP models

The sciences do not try to explain...they mainly make models[1]

The advantages of two-box models are first that they are instructive. The results are easy to grasp and a lot of the calculations can be done analytically. Second, two box models have been used to study planetary atmospheres before (e.g. Lorenz et al. (2001)). Third, the two-box atmospheric MEP model developed in this chapter lay the foundation for the AMEP model finally used in the comparison with CAM3.

In the process of making an AMEP model, horizontal box models and vertical box models are developed and investigated, independently at first and in combination later on. Initially, the box models are considered to be closed systems, i.e. both the atmosphere and the surface are considered together. Later, only the atmosphere layer is analyzed.

In Paltridge's MEP model only the entropy associated with the meridional heat transport is maximized. Entropy is also produced due to vertical heat transfer, like convection of latent and sensible heat. Paltridge did not consider the entropy production from these processes. Instead he employed the principle of maximum convection (e.g. Busse (1978)). The principle of maximum convection will no longer be used in this thesis. Instead the entropy production is maximized in both vertical and horizontal direction.

5.1 The horizontal box models

Several two-box models are used to represent the climate system on Earth in different ways and to find the MEP states for the systems (i.e. the two boxes). Box 1 represents the tropics and Box 2 represents higher latitudes and the entropy production of the system is associated with the horizontal heat transport between them. The insolation at TOA for Box 1 and Box 2

[1] John von Neumann (1903-1957)

are F_1 and F_2, and are assumed known. The temperatures of the boxes and the horizontal heat flux between them, are unknowns.

The total entropy production for the system is defined as

$$\dot{S} = \frac{\mathrm{d}F_{heat,1}}{T_1} + \frac{\mathrm{d}F_{heat,2}}{T_2} \tag{5.1.1}$$

where $\mathrm{d}F_{heat,1}$ and $\mathrm{d}F_{heat,2}$ are the heat convergence and T_1 and T_2 are the absolute temperatures in Box 1 and Box 2, respectively. As discussed in section 3.2.4, it is the entropy production associated with turbulent motion alone that is maximized, i.e.

$$\dot{S} = -\frac{\zeta_1}{T_1} + \frac{\zeta_2}{T_2} = \zeta\big(\frac{1}{T_2} - \frac{1}{T_1}\big) = \text{maximium} \tag{5.1.2}$$

where $\zeta_1 = -\zeta_2 = \zeta$.

5.1.1 The blackbody model

The blackbody model described in this section is the same as described in section 3.2.6. The model is included in order to investigate parameter dependence and to add completeness to the models descriptions made in this chapter. The only difference between this model and the model from section 3.2.6 is the subscripts. Instead of a tropics (T) and a polar (P) box, the boxes are labeled 1 and 2.

The Earth-atmosphere system is assumed to be a blackbody, so the only processes considered in this model are the absorption of solar radiation and the emission of longwave radiation, as well as the horizontal heat flux between the two boxes. A steady state of thermal equilibrium is assumed for each box separately. The energy balance equation for each box can be written as

$$F_i - \sigma T_i^4 - \zeta_i = 0 \qquad (\text{Box } i) \tag{5.1.3}$$

for i={1,2}.

The system (i.e. the two boxes together) is assumed to be in global radiative equilibrium, hence the sum of the incoming solar radiation equals the sum of the OLR, which provide the constraint

$$F_1 + F_2 - \sigma T_1^4 - \sigma T_2^4 = 0 \tag{5.1.4}$$

The entropy production in box i can be written as

$$\dot{S}_i = -\frac{\zeta_i}{T_i} = -\frac{F_i - \sigma T_i^4}{T_i} \tag{5.1.5}$$

To find the maximal entropy production possible for this system, we need to find ζ_i such as to maximize $\dot{S}_i$ subject to the equilibrium constraint in

equation 5.1.4. The method of Lagrangian multipliers described in section 3.2.6 is used with

$$\frac{\partial \mathscr{L}}{\partial T_i} = 4\beta\sigma T_i^5 - 3\sigma T_i^4 - F_i = 0 \tag{5.1.6}$$

$$\frac{\partial \mathscr{L}}{\partial \beta} = -\sum_{i=1,2} F_i - \sigma T_i^4 = 0 \tag{5.1.7}$$

The result is shown in figure 5.1. The insolation in Box 2, F2, is set constant to $200 Wm^{-2}$, while the insolation in Box 1, F1, varies from $200 Wm^{-2}$ to $600 Wm^{-2}$. The blue, solid line is the temperature in Box 1 and the black, solid line is the temperature in Box 2 (figure 5.1(a)). The horizontal heat flux between the two boxes is seen as the red, solid line in figure 5.1(b).

The two boxes are in thermal equilibrium for F1=F2=$200 Wm^{-2}$, which causes zero horizontal heat flux, i.e. ζ=0. As the insolation in Box 1 increases, the temperature in Box 1 increases much more rapidly than in Box 2. The increased temperature gradient between the two boxes results in an increased horizontal heat flux.

Kleidon (2004) and Lorenz et al. (2001) used similar two-box models (see example used in section 3.2.6). As noted, the horizontal heat flux between the boxes was expressed as a linear function $\zeta = k \cdot (T_1 - T_2) = k \cdot \Delta T$, with k being the effective conductivity. Both studies showed that for the atmosphere on Earth the maximum entropy production occurred for k$\simeq 2\ Wm^{-2}K^{-1}$. Figure 5.1(b) shows that k$\simeq 2\ Wm^{-2}K^{-1}$ (black, solid line) is a reasonable result, but the linear flux parametrization is only valid for small values of ΔT

5.1.2 The grey atmosphere and black surface model

The next step is to extend the model into a more realistic representation of the climate system. A surface layer with fixed temperatures is included in each box. The surface layer is considered a blackbody. The atmosphere is no longer considered a blackbody, but radiates as a grey body, $\epsilon\sigma T^4$, where ϵ is the mean global atmospheric emissivity. Using Kirchhoff's law, which states that the atmospheric emissivity equals the atmospheric absorptivity for an atmospheric layer in thermal equilibrium, a fraction, ϵ, of the longwave radiation emitted from the surface is absorbed by the atmosphere, while the remaining fraction, $(1 - \epsilon)$, is emitted to space.

The energy balance equation for box i is

$$F_i - \epsilon\sigma T_i^4 - (1-\epsilon)\sigma T_{si}^4 - \zeta_i = 0 \qquad \text{(Box } i\text{)} \tag{5.1.8}$$

where i={1,2}.

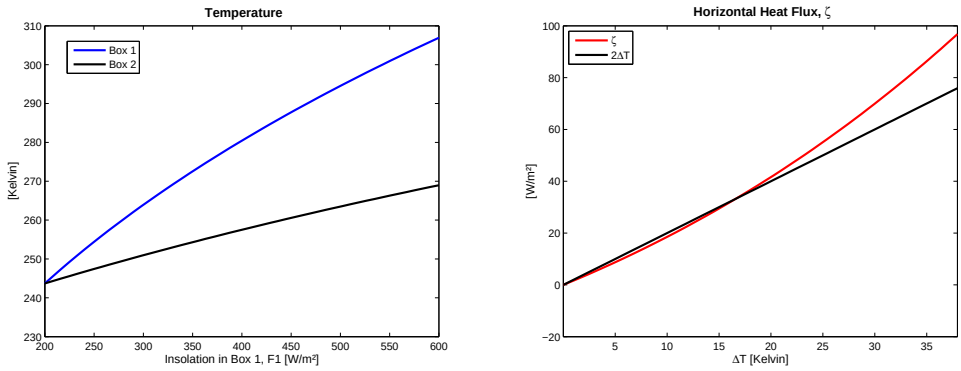

(a) (b)

Figure 5.1: (a) The resulting temperatures corresponding to the MEP state in Box 1 (blue line) and in Box 2 (black line) for the two box model . The insolation in Box 1 varies between $200Wm^{-2}$ and $600Wm^{-2}$, while the insolation in Box 2 is constant and equals $200Wm^{-2}$. (b) The horizontal heat flux, ζ, as a function of the temperature difference between the two boxes, $\Delta T = (T_1 - T_2)$. Also included is the $2\Delta T$ parametrization (see text for details).

The system is assumed to be in global radiative equilibrium, which provides the constraint

$$F_1 + F_2 - \epsilon\sigma T_1^4 - (1-\epsilon)\sigma T_{s1}^4 - \epsilon\sigma T_2^4 - (1-\epsilon)\sigma T_{s2}^4 = 0 \tag{5.1.9}$$

Defining the cost function as before, we obtain

$$\frac{\partial \mathscr{L}}{\partial T_i} = \epsilon\sigma T_i^4(4\beta T_i - 3) - F_i + (1-\epsilon)\sigma T_{si}^4 = 0 \tag{5.1.10}$$

$$\frac{\partial \mathscr{L}}{\partial \beta} = -\sum_{i=1,2} F_i - \epsilon\sigma T_i^4 - (1-\epsilon)\sigma T_{si}^4 = 0 \tag{5.1.11}$$

The insolation in Box 2 is kept constant and equal to $200Wm^{-2}$, while the insolation in Box 1 varies between $200Wm^{-2}$ and $600Wm^{-2}$. The emissivity equals 0.9, calculated from Trenberth et al. (2009), in both boxes. The surface temperatures are fixed and equal to 290K and 265K in Box 1 and Box 2, respectively.

The results are shown in figure 5.3. For equal or nearly equal values of the insolation in the boxes, the temperature in Box 1 is colder than in Box 2, which causes a negative heat flux. This is a consequence of a greater OLR surface term loss in Box 1 due to a warmer surface temperature than in Box 2. As the insolation in Box 1 increases, the temperature in Box 1 becomes much warmer than the temperature in Box 2 which causes an increased heat

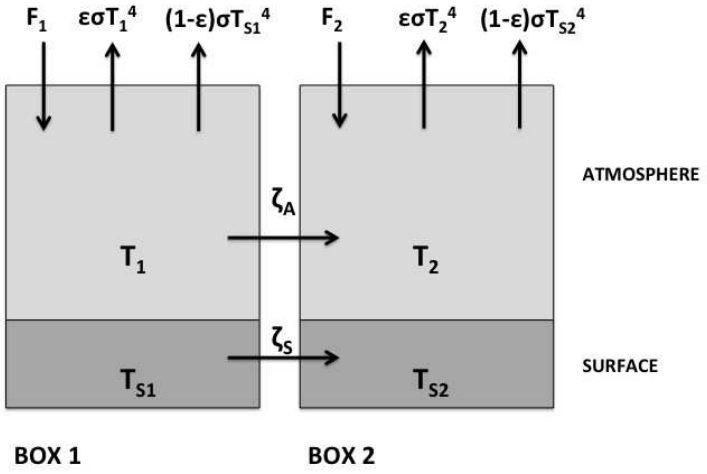

Figure 5.2: A two-box model representing the climate system on Earth. The surface layers are assumed blackbodies with fixed temperatures, while the atmosphere layers are assumed grey bodies radiating with an emissivity ϵ. F1 and F2 are the insolation at the top of Box 1 and Box 2, respectively.

flux from Box 1 to Box 2.

The results are not too different from the blackbody results from the previous section, due to the high value of ϵ. Also included in figure 5.3(a) are the fixed surface temperatures for the two boxes (dashed lines). As the insolation increases the atmosphere gets warmer than the surface in both boxes. Because the surface temperatures stay fixed, only the atmosphere heats as a response to the increased insolation.

The atmospheric emissivity, ϵ

In the real atmosphere the emissivity will vary in magnitude, as well as between "boxes". Variations in the atmospheric emissivity has a great impact on the solution as shown in figure 5.4. Here the insolation is set constant to $300 Wm^{-2}$ in Box 1 and $200 Wm^{-2}$ in Box 2, while ϵ varies between 0 and 1. The surface temperatures stay fixed.

As seen in the temperature plot, figure 5.4(a) there is no solution for $\epsilon < 0.29$. The reason for this is not due to the MEP assumption, but a consequence of fixed surface temperatures and the assumption of a system in global radiative balance. An emissivity smaller than 0.29 will require negative OLR terms in order to keep the energy balance at TOA, which is impossible.

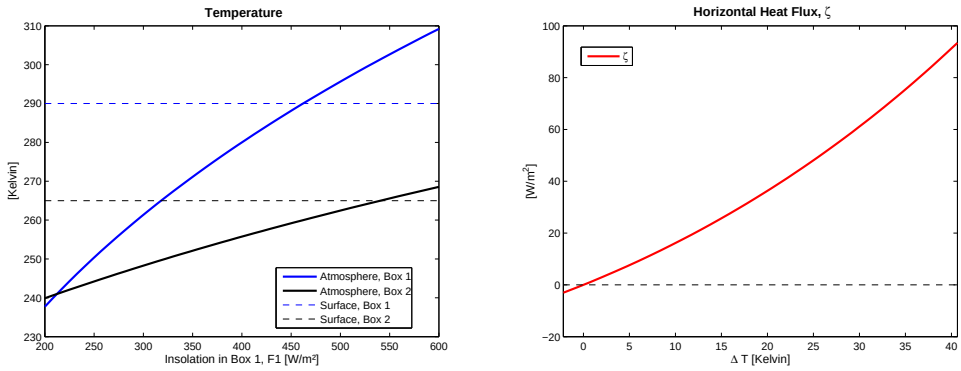

(a) Atmospheric temperature

(b) The horizontal heat flux, ζ

Figure 5.3: (a) The resulting atmospheric temperatures in Box 1 (blue, solid line) and for Box 2 (black, solid line) for the two box model as the insolation in Box 1 varies between $200Wm^{-2}$ and $600Wm^{-2}$, while the insolation in Box 2 is constant and equals $200Wm^{-2}$. The atmospheric emissivity is set equal to 0.9 in both boxes. Also included is the fixed surface temperatures for Box 1 (blue, dashed line) and for Box 2 (black, dashed line). (b) The corresponding horizontal heat flux, ζ, as a function of the temperature difference between the two atmospheric layers.

If we consider the case where $\epsilon = 0.25$, the insolation in Box 1 equals the OLR from the surface term, i.e. $(1-\epsilon)\sigma T_{s1}^4$. In Box 2 the OLR from surface term is 10W/m2 greater than the insolation term. To keep the global radiative equilibrium constraint, one of the atmospheric radiation terms, $\epsilon\sigma T_i^4$, must become negative which is impossible, so no solution exists. For the atmosphere on Earth, ϵ is in general greater than 0.3.

Both atmospheric layers gain energy as the emissivity increases (see figure 5.4(a)). This is a consequence of an increased energy supply to the atmosphere from the surface layer, ϵT_s^4, which is greater than the increased loss of radiation from the atmosphere to space, ϵT^4, since both atmosphere layers stay colder than their respective surface layers. The atmosphere layer in Box 1 gains more energy due to a warmer surface temperature than the atmosphere layer in Box 2, causing an increased horizontal heat flux as the emissivity approaches 1 (see figure 5.4(a)).

5.1.3 A two-box atmospheric MEP model

As seen in section 5.1.2, keeping the surface temperatures fixed has a great impact on the solution. The surface temperatures are not fixed in CAM3, but act as a boundary which is allowed to change in response to the heat exchange with the atmosphere. The surface temperature forcing on the other hand can be fixed in the model. Later on, perturbed SST runs are performed

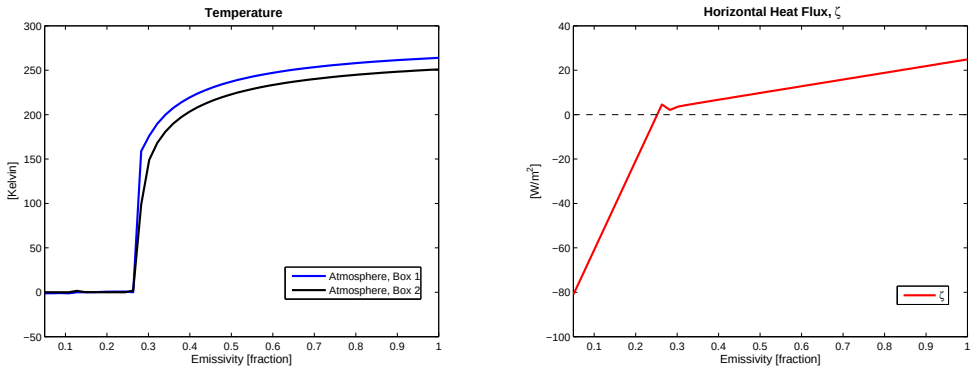

(a) (b)

Figure 5.4: Temperature and heat flux responses to changes in the emissivity, $0 \leq \epsilon \leq 1$. The insolation and surface temperatures in both boxes are set constant and equal to $300 W m^{-2}$, 290K and $200 W m^{-2}$, 265K in Box1 and Box 2 respectively. There is no solution for $\epsilon \leq 0.29$ due to the failing of the equilibrium constraint.

for both CAM3 and the MEP model. To compare the two models, the MEP model needs to act as an atmosphere model, using the surface temperature as a boundary forcing.

A more complete two-box MEP model is seen in figure 5.5. In this, the atmosphere absorbs a fraction A of the incoming solar radiation and a fraction, ϵ, of the terrestrial radiation emitted from the surface. The atmosphere emits a fraction ϵ of longwave radiation in two directions, to space and to the surface. The other constants are as described in the previous sections. In this section only the radiation processes are considered. Convective fluxes between the surface and the atmosphere will be added subsequently (see section 5.2).

The MEP model will be run with different surface layer temperatures later on (chapter 6). The increased surface temperatures act as an energy forcing at the surface boundary. Because the surface itself is not in equilibrium, the global radiative equilibrium constraint at TOA and the energy balance assumption in the surface layer will no longer be valid.

Each atmospheric box is assumed to remain in energy balance, independent of the surface temperatures used, providing the equation

$$F_i A - 2\epsilon\sigma T_i^4 + \epsilon\sigma T_{si}^4 - \zeta_i = 0 \qquad \text{(Box } i\text{)} \qquad (5.1.12)$$

for each box i={1,2}

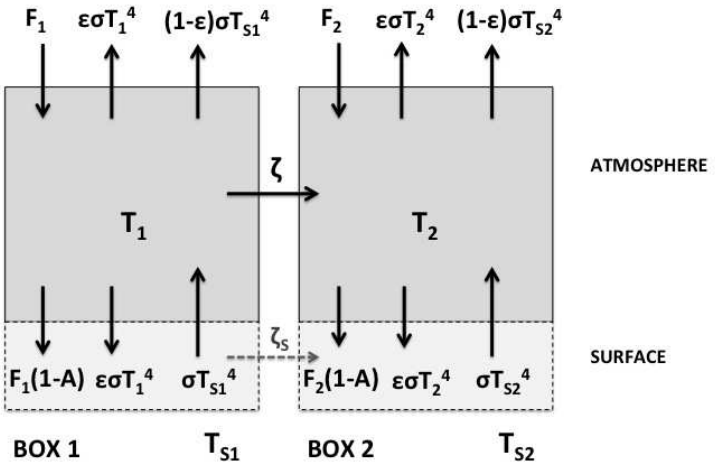

Figure 5.5: A two-box model representing the atmosphere. The surface layers act as an energy forcing boundary and the horizontal heat flux considered is only the atmospheric component. The atmosphere absorbs a fraction A of the solar radiation and the atmosphere emits energy as a grey body with an emissivity ϵ. F1 and F2 are the insolation at the top of Box 1 and Box 2, respectively.

ζ is now only the atmospheric component of the horizontal heat flux. The equilibrium constraint used is

$$\sum_{i=1,2} \zeta_i = 0 \tag{5.1.13}$$

which states that no heat is stored within the atmosphere.

With the analogous cost function, the constraints become

$$\frac{\partial \mathscr{L}}{\partial T_i} = \epsilon\sigma T_i^4(8\beta T_i - 6) - F_i A - \epsilon\sigma T_{si}^4 = 0 \tag{5.1.14}$$

$$\frac{\partial \mathscr{L}}{\partial \beta} = -\sum_{i=1,2} F_i A - 2\epsilon\sigma T_i^4 + \epsilon\sigma T_{si}^4 = 0 \tag{5.1.15}$$

The resulting atmospheric temperatures and heat flux can be seen in figure 5.6. A is constant and equals 0.3 (calculated from Trenberth et al. (2009)) in both layers. The other constants are as described in the previous section.

The atmospheric temperature in both boxes and the horizontal heat flux between them show less variation than in the previous model results. The reason is mostly because of the specified atmospheric absorptivity of solar radiation, A, resulting in a much smaller energy gain in the boxes. The heat

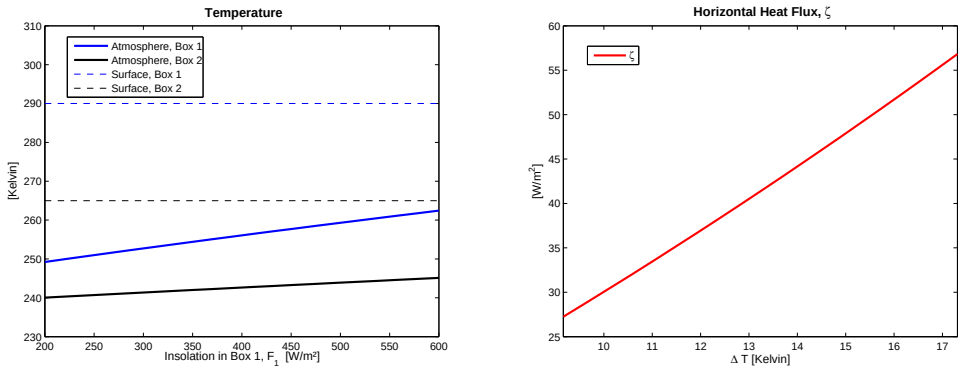

(a) (b)

Figure 5.6: (a) The resulting atmospheric temperatures in Box 1 (blue, solid line) and Box 2 (black, solid line) for the atmosphere only MEP model. The insolation in Box 1 varies between $200Wm^{-2}$ and $600Wm^{-2}$, while the insolation in Box 2 is constant and equals $200Wm^{-2}$. The surface temperatures in both boxes are set constant and equal 290K and 265K in Box1 (blue, dashed line) and Box 2 (black, dashed line), respectively. The atmospheric emissivity is set equal to 0.9 and the atmospheric absorptivity equals 0.3, in both boxes. (b) The atmospheric component of the horizontal heat flux, ζ, as a function of the temperature difference between the two atmospheric layers.

flux appears linear. This is a result of the reduced temperature difference between the two layers, ΔT. As seen in the previous sections, the heat flux is almost linear for small ΔT values.

The atmospheric absorptivity, A

Increasing the absorptivity of solar radiation increases the atmospheric temperature in both boxes because of the extra energy gain. This can bee seen in figure 5.7, which shows the response to variations in the atmospheric absorptivity for constant insolation, emissivity and surface temperatures. For equal values of A, Box 1 gains more energy than Box 2 because of the greater insolation in Box 1. This causes the temperature in Box 1 to warm more than in Box 2, which increases the temperature gradient between the boxes, resulting in a greater heat flux.

The atmospheric emissivity, ϵ

In comparison with the previous models, the atmosphere now emits radiation in two directions causing a doubling of the atmospheric loss of longwave radiation. Decreasing the emissivity makes the atmospheric temperatures increase (see figure 5.8(a)) due to reduced radiation loss. The reduced emissivity also causes the temperature difference in the two boxes to decrease,

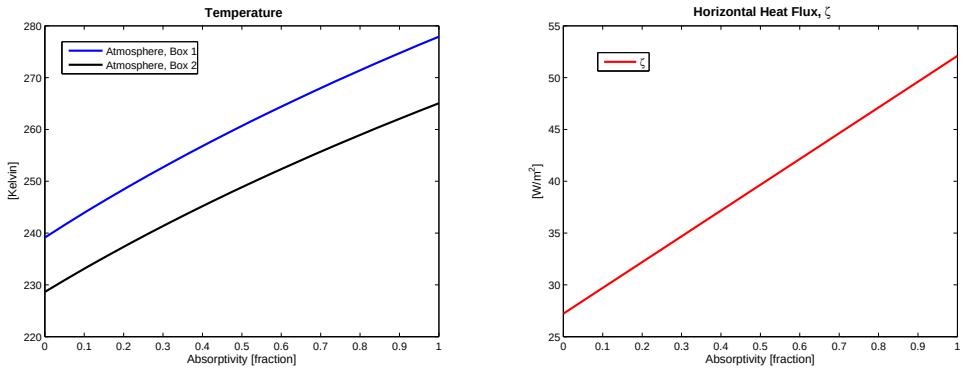

(a) (b)

Figure 5.7: Temperature (a) and heat flux (b) responses to changes in the atmospheric absorptivity, $0 \leq A \leq 1$. The insolation and surface temperatures in both boxes are set constant and equal to $300Wm^{-2}$, 290K and $200Wm^{-2}$, 265K in Box1 and Box 2, respectively.

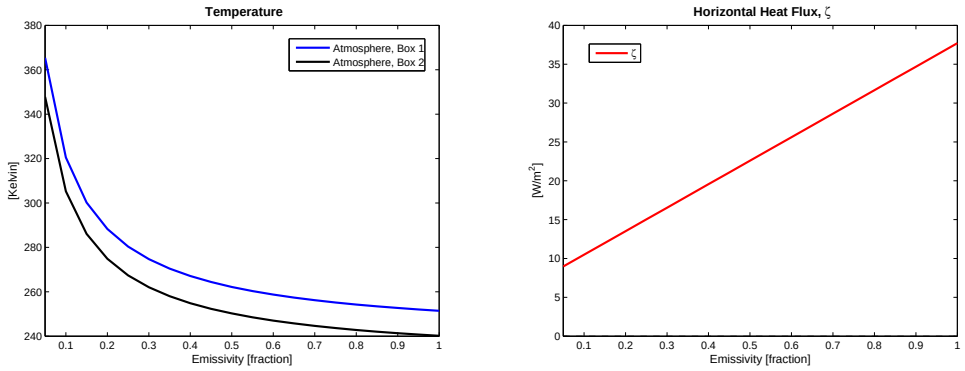

(a) (b)

Figure 5.8: Temperature (a) and heat flux (b) responses due to variations in the emissivity, $0 \leq \epsilon \leq 1$. The insolation and surface temperatures in both boxes are set constant and equal to $300Wm^{-2}$, 290K and $200Wm^{-2}$, 265K in Box1 and Box 2, respectively.

resulting in a smaller heat flux between the boxes.

This result is quite the opposite of that obtained from the model in section 5.1.2, where the temperatures of the atmosphere layers, within each box, increased as the emissivity increased, resulting in a greater heat flux for ϵ approaching 1. The same values for the fixed surface temperatures were used in both models. The difference is that in the model in section 5.1.2 the

atmosphere-surface system was considered together. As such, increasing the surface temperature causes a decrease in the atmospheric temperature. In this model, where the energy balance of the surface is relaxed, the surface temperature actually warms the atmosphere. This is in line with the CAM3 results, presented hereafter.

5.2 The vertical box model

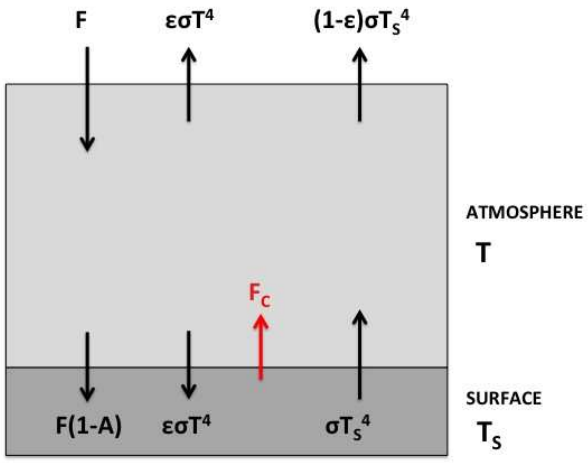

Figure 5.9: A two box model representing the atmosphere and the surface layer. The atmosphere absorbs a fraction A of the incoming solar radiation, F. The remaining part is absorbed by the surface. The atmosphere radiates in both directions with an emissivity ϵ and a radiative temperature T. The surface radiates as a blackbody with a radiative temperature T_S. There is also a convective flux of latent- and sensible heat, F_c, between the surface and the atmosphere layer.

Only radiative processes have been considered so far. There is also an additional heat flux that needs to be taken into consideration, namely the convective fluxes of sensible and latent heat between the surface and the atmosphere. To see how to include those, we consider a two-box *vertical* model. The approach is to use the model to see how the convective fluxes depend on the temperature difference between the atmospheric and surface layer. This will allow us to parametrize the convective fluxes in the preceding box model.

In constructing an atmospheric MEP model, only the energy balance equation for the atmospheric layer remains (see section 5.1.3). When the convective heat flux is added to the system, there are too many unknowns to find a MEP solution. One way to solve this problem is to parametrize the

convective heat flux. In this section a parametrization method based on the MEP principle is shown.

The transport processes of convective heat between the atmosphere and the surface are also turbulent processes; thus a steady state of MEP can be found for the convective heat transfer as well as for the horizontal heat flux. The entropy produced from the convective heat flux is

$$\dot{S} = F_c\left(\frac{1}{T} - \frac{1}{T_s}\right) \tag{5.2.1}$$

where F_c is the convective heat flux, T is the absolute temperature of the atmosphere and T_s is the absolute temperature of the surface. F_c is defined as positive if the atmosphere gains heat from the surface. The entropy produced from the convective heat flux is the only entropy production considered in this section.

5.2.1 A vertical two-box MEP model

The model consists of two boxes, representing the atmospheric and the surface layer (see figure 5.9). The layers are assumed to be in thermal equilibrium separately, i.e. there is no temperature gradient within one layer. The total system is also assumed to be in global radiative equilibrium, hence the incoming solar radiation equals the OLR at TOA. There is no horizontal energy exchange in the model.

The atmosphere absorbs a fraction A of the incoming solar radiation, while the remaining fraction, 1-A, is absorbed by the surface. The atmosphere radiates equally in both directions with an emissivity ϵ. A fraction, ϵ, of the longwave radiation emitted from the surface is absorbed by the atmosphere, while the remaining fraction, $(1-\epsilon)$, is emitted to space. In addition there is a convective flux of latent and sensible heat, F_c, between the surface and the atmosphere.

Assuming thermal equilibrium within each layer separately, the energy balance equations for the atmosphere and the surface can be written as

$$FA + F_c + \epsilon\sigma T_s^4 - 2\epsilon\sigma T^4 = 0 \qquad \text{(Atmosphere)} \tag{5.2.2a}$$

$$F(1-A) + \epsilon\sigma T^4 - F_c - \sigma T_s^4 = 0 \qquad \text{(Surface)} \tag{5.2.2b}$$

with the radiative equilibrium constraint

$$F = \epsilon\sigma T^4 + (1-\epsilon)\sigma T_s^4 \tag{5.2.3}$$

Equation 5.2.3 is used to express the surface temperature as a function of the insolation and the atmospheric temperature. Assuming F, A and ϵ to be known, the entropy production is now only a function of the atmospheric

temperature, T. To find the MEP state the entropy is maximized w.r.t. the atmospheric temperature alone.

Since the two terms expressing F_c in the energy balance equations 5.2.2a,b denote the same quantity, a necessary condition is that the two terms must be equal, i.e.

$$\sum_{\substack{i= \\ Atmosphere \\ Surface}} F_{c,i} = 2\epsilon\sigma T^4 - FA - \epsilon\sigma T_s^4 + F(1-A) + \epsilon\sigma T^4 - \sigma T_s^4$$

$$= 3\epsilon\sigma T^4 + F(1-2A) - \frac{1+\epsilon}{1-\epsilon}(F - \epsilon\sigma T^4) = 0 \qquad (5.2.4)$$

which provides the cost function

$$\mathscr{L} = \frac{2\epsilon\sigma T^4 - FA - \left(\frac{\epsilon}{1-\epsilon}\right)(F-\epsilon\sigma T^4)}{T} - \beta\Big(3\epsilon\sigma T^4 + F(1-2A) - \frac{1+\epsilon}{1-\epsilon}(F-\epsilon\sigma T^4)\Big) \qquad (5.2.5)$$

To find the maximum entropy production we need to find T_i and β s.t.

$$\frac{\partial\mathscr{L}}{\partial T} = 3\epsilon\sigma T^4\Big(2+\frac{\epsilon}{1-\epsilon}\Big) + F\Big(A+\frac{\epsilon}{1-\epsilon}\Big) - 4\beta\epsilon\sigma T^5\Big(3+\frac{1+\epsilon}{1-\epsilon}\Big) = 0 \qquad (5.2.6)$$

$$\frac{\partial\mathscr{L}}{\partial\beta} = -\Big(3\epsilon\sigma T^4 + F(1-2A) - \frac{1+\epsilon}{1-\epsilon}(F-\epsilon\sigma T^4)\Big) = 0 \qquad (5.2.7)$$

The resulting T and F_c is shown in figure 5.10. The incoming solar radiation, F, varies between $200 Wm^{-2}$ and $600 Wm^{-2}$. As in the previous sections, the atmospheric absorptivity of solar radiation, A, equals 0.3, and the atmospheric emissivity, ϵ, equals 0.9. The temperatures of the atmospheric layer (blue, solid line) and the surface layer (black, solid line) can be seen in figure 5.10(a). The convective heat flux, F_c, is seen as red dots in figure 5.10(b). Also included in figure 5.10(b) is the parametrization of F_c seen as a black solid line.

Both the surface and the atmospheric temperatures increase as the insolation, F, increases. The surface temperature increases faster than the atmospheric temperature, making the convective heat flux increase as well.

The convective heat flux is proportional to $(T_s - T)^4$ with a proportionality constant k = $9.6 \cdot 10^{-4} Wm^{-2}K^{-4}$ for the given values of F, A and ϵ. k=k(F,A,ϵ) and will vary for different values of F, A and ϵ than the one used in this example. The ΔT^4 dependence may not seem too surprising since the longwave fluxes also radiate proportional to T^4, but in most climate models the convective heat flux is parametrized proportional to $(T_s - T)$, where the proportionality constant includes other factors such as wind speed, surface roughness, specific humidity, air density, etc. The convective heat flux in

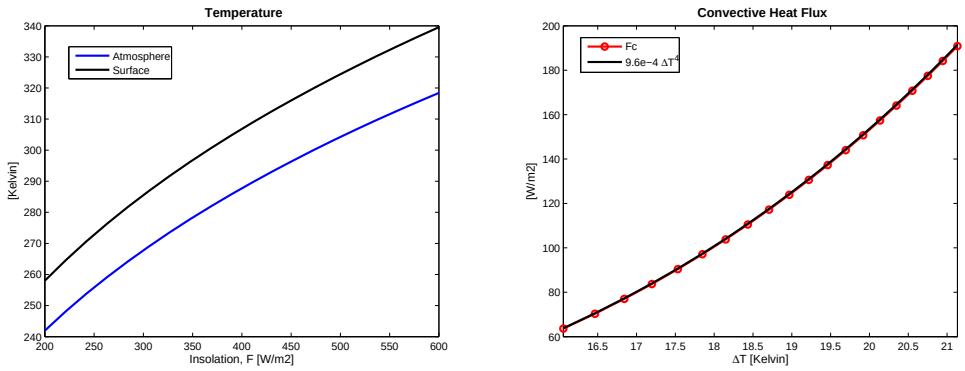

(a) (b)

Figure 5.10: (a) The resulting atmospheric (blue line) and surface (black line) temperatures due to changes in the insolation, $200Wm^{-2} \leq F \leq 600Wm^{-2}$. The atmospheric parameters are kept constant, ϵ=0.9 and A=0.3. (b) The corresponding vertical flux of latent and sensible heat, F_c, as a function of the temperature difference between the two boxes, $\Delta T = (T_s - T)$. Also included is a ΔT^4 parametrization of F_c (see text for details).

CAM3 is based on such a linear dependence.

Changes in the atmospheric absorptivity and emissivity will cause changes in the temperatures for both the atmospheric and the surface layer, which also affects the convective heat flux.

The emissivity, ϵ

Figure 5.11 shows the temperature in the atmospheric layer and the surface layer for different values of the atmospheric emissivity and the corresponding convective heat flux. In the limit of a white atmosphere, i.e. $\epsilon = 0$, all the OLR originates from the surface. Without any greenhouse effect, the temperature in the atmospheric layer is determined solely by the insolation, F. For A$\neq$ 0, the atmosphere gains solar energy without losing any longwave energy to the surroundings, resulting in a very warm atmospheric temperature. The corresponding convective heat flux is negative indicating an energy flow from the atmosphere to the surface.

As the emissivity increases the atmosphere has an additional radiative sink resulting in a decreasing temperature while the surface gains more and more radiative energy from the atmosphere. Hence the temperatures in the two layers approach each other and are equal for $\epsilon = 0.3$ (figure 5.11(a)). For $\epsilon > 0.3$ the surface temperature is warmer than the atmospheric temperature, and the temperature gradient between the layers intensifies as ϵ becomes greater, resulting in a positive and increasing convective heat flux.

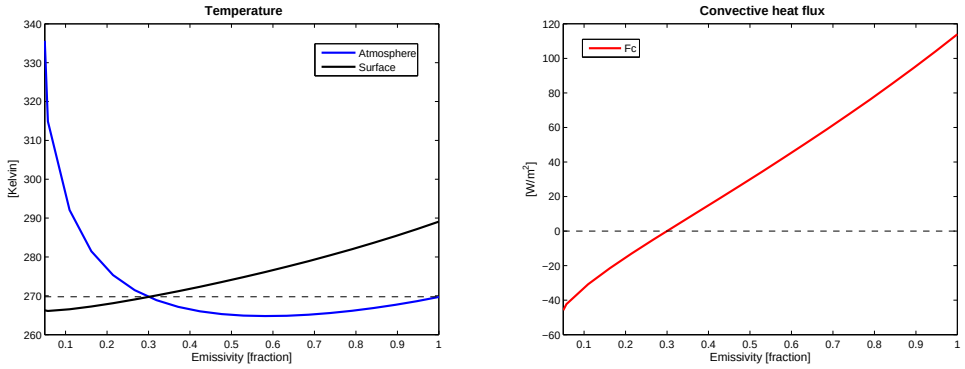

(a) (b)

Figure 5.11: Variations in temperatures (a) and the convective heat flux (b) due to changes in the atmospheric emissivity,ϵ. A=0.3, $F = 300W/m^2$ and $0 \leq \epsilon \leq 1$.

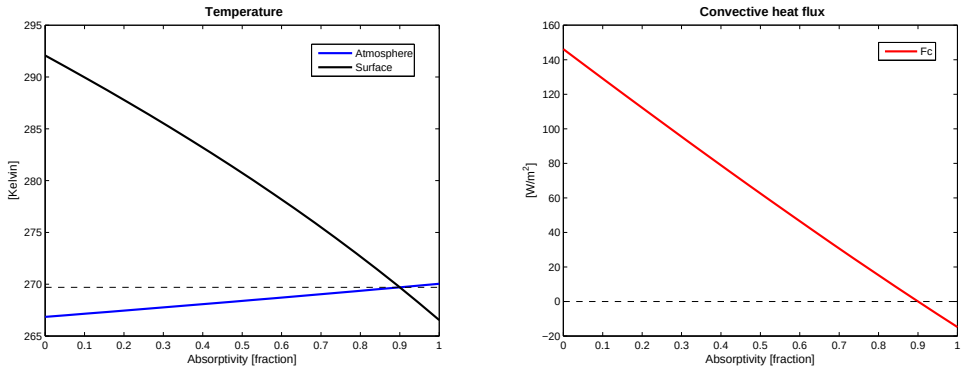

(a) (b)

Figure 5.12: Variations in temperatures (a) and the convective heat flux (b) due to changes in the atmospheric absorptivity, A, of solar radiation. $0 \leq A \leq 1$, $\epsilon = 0.9$, $F = 300W/m^2$

The absorptivity of solar radiation, A

Increasing A results in an increased energy supply to the atmosphere and a decreased energy supply to the surface. For A = 0 the surface layer absorbs all of the incoming solar radiation resulting in a very warm surface (figure 5.12(a)) and a large convective flux from the surface to the atmosphere (figure 5.12(b)). As A increases the atmospheric layer warms while the surface layer cools, resulting in a reduced convective heat flux. The atmosphere gets warmer than the surface, causing a negative heat flux for A approaching 1.

For small values of ϵ and large values of A, the atmosphere becomes warmer than the surface. In the climate system on Earth, the value of A is relatively small and the value of ϵ is relatively large in general. Therefore this will not cause problems in the AMEP model described in the next chapter.

Chapter 6

AMEP

6.1 The AMEP box model

For comparison with results from CAM3, we require more resolution than in a two-box model. The atmospheric MEP model discussed in the previous chapter (section 5.1.3), is extended here to include 64 boxes. This gives a latitudinal resolution of approximately 2.8 degrees, the same resolution used in CAM3. Also included are fluxes of sensible and latent heat, discussed in section 5.2. Each box represents the zonal mean conditions for an atmospheric column and the adjacent boxes cover the globe from the South Pole to the North Pole. The annually- and zonally-averaged surface temperatures from CAM3 are used as a boundary forcing in the model.

In this section the focus is on the expression for ζ, defining the Lagrangian cost function. Reflectivity of solar radiation, R, and zonal variations of the atmospheric parameters, R, A and ϵ, are discussed in the subsequent section. For now the $F_i A$ term in the energy balance equations represents the energy gain from solar insolation in the ith atmospheric column, denoted as Box i, and the subscripts for the A and ϵ are dropped to ease the following calculations.

Assuming that the vertical heat exchange occurs on a much shorter timescale than the meridional heat exchange, the two processes are treated independently. The parametrization for the convective heat flux

$$F_c = k(T_{si} - T_i)^4 \,\mathrm{sign}(T_{si} - T_i) \tag{6.1}$$

calculated in section 5.2 is used. The additional term $\mathrm{sign}(T_{si} - T_i)$ is added to the parametrization to include $T_{si} < T_i$ conditions, but is dropped hereafter to simplify the equations. The horizontal heat flux, ζ, is from now referred to as the meridional heat divergence.

The energy balance for each atmospheric column can be written as

$$F_i A + k(T_{si} - T_i)^4 - 2\epsilon\sigma T_i^4 + \epsilon\sigma T_{si}^4 - \zeta_i = 0 \qquad \text{(Box } i\text{)} \tag{6.2}$$

Since the convective heat flux is parametrized, it is only the entropy production associated with the meridional heat divergence that is maximized (see section 3.2.4). It is the entropy production from this heat transfer which is considered in all calculations throughout the chapter.

The energy constraint for the atmosphere is

$$\sum_{i=1}^{64} \zeta_i \, cos(\phi_i) = 0 \tag{6.3}$$

which states that there is no heat stored within the atmosphere. The $cos(\phi)$ term is included to account for the different areas of the latitude zones the atmospheric columns cover, with larger areas covered for columns at low latitudes than at higher latitudes.

The total entropy production associated with the horizontal heat divergence is

$$\dot{S} = -\sum_{i=1}^{64} \frac{\zeta_i}{T_i} cos(\phi) \tag{6.4}$$

The Lagrangian cost function, $\mathscr{L}$, used to maximize the entropy production can be written as

$$\mathscr{L} = \sum_{i=1}^{64} \left(\frac{\zeta_i}{T_i} - \beta \zeta_i \right) cos(\phi_i) \tag{6.5}$$

To find the MEP state we need to find T_i and β s.t.

$$\frac{\partial \mathscr{L}}{\partial \beta} = -\sum_{i=1}^{64} \zeta_i \, cos(\phi_i) = 0 \tag{6.6}$$

$$\frac{\partial \mathscr{L}}{\partial T_i} = \left(T_i \frac{\partial \zeta_i}{\partial T_i} (1 - \beta T_i) - \zeta_i \right) cos(\phi_i) = 0 \tag{6.7a}$$

which means that

$$\frac{\partial \mathscr{L}}{\partial T_i} = T_i \frac{\partial \zeta_i}{\partial T_i} (1 - \beta T_i) - \zeta_i = 0 \tag{6.7b}$$

where

$$\frac{\partial \zeta_i}{\partial T_i} = -\left(4k(T_{si} - T_i)^3 + 8\epsilon\sigma T_i^3 \right) \tag{6.8}$$

$\partial \mathscr{L} / \partial T_i$ is solved numerically for each box separately, while $\partial \mathscr{L} / \partial \beta$ provides the energy constraint for the total model.

6.2 Parameters

In a complex model like CAM3, it is not easy to understand the response to altered SST because of all the changes that occur in the different model runs. Parameters like the emissivity, ϵ, the absorptivity, A, and the reflectivity, R, of the atmosphere are changed in CAM3 when the SST is altered. Different water vapor content in the atmosphere and altered cloud cover fraction are two of the changes that modify the parameters; ϵ, A and R. With this in mind, the parameters used in AMEP are not changed between the different SST runs, in order to rule out some of the feedback mechanisms. Adjusting the parameters so that they mimic the changes observed in the perturbed SST runs in CAM3, will contradict the main reason for choosing a simple model in the first place.

First a AMEP run is performed (section 6.2.2) where the parameters are kept constant between runs and boxes. Secondly, the parameters are varied zonally while being kept constant between the runs (section 6.2.3). By using the same parameters for all runs, changes in the results are only a consequence of changes in T_s. This makes the AMEP results even easier to grasp. However, AMEP is a zonally-averaged model and changes in the parameters as a function of latitude are expected. Using parameters that vary zonally provides a more realistic situation.

Before presenting the AMEP results using the two parameter options, it is necessary to determine the proportionality constant, k, used in the parametrized convective heat flux.

6.2.1 The proportionality constant k

The results from the AMEP model will be compared with output from CAM3 later on. It is therefore important to see if the $(T_s - T)^4$ parametrization also is valid for the latent- and sensible heat flux in CAM3. In CAM3, air-sea turbulent fluxes are calculated from the bulk formulas (Collins et al., 2004):

$$LH = L\rho_a C_E U \Delta q \qquad \text{(latent heat)} \tag{6.1}$$

$$SH = c_p \rho_a C_H U \Delta\theta \qquad \text{(sensible heat)} \tag{6.2}$$

where ρ_a is the air density, U is the wind speed, c_p is the specific heat at constant pressure and L is the latent heat of vaporization. $\Delta\theta$ and Δq are the potential temperature difference and the difference in specific humidity between the sea surface and the lowest model level. C_H and C_E are aerodynamic transfer coefficients for temperature and humidity, respectively.

The vertical MEP model has one atmospheric layer. CAM3 has 26 atmospheric layers. To do a comparison it is necessary to use one atmospheric temperature that represents the mean atmospheric temperature in CAM3.

This temperature is chosen to be the density-weighted average atmospheric temperature

$$T \equiv \frac{\int_V \overline{T}(x,y,z) \cdot \overline{\rho}(x,y,z) \mathrm{d}V}{\int_V \overline{\rho}(x,y,z) \mathrm{d}V} \tag{6.3}$$

where $\overline{T}(x,y,z)$ is the temporally-averaged atmospheric temperature and $\overline{\rho}(x,y,z)$ is the temporally-averaged atmospheric density in CAM3.

Figure 6.1 shows the latent and sensible heat output from CAM3 as red and blue dots. The blue dots represent values from the SH and the red dots are values from the NH. $\Delta T = (T_s - T)$ is the temperature difference between the surface and the density-weighted average atmospheric temperature. Also included are the linear (green, solid line) and the ΔT^4 (black, solid line) parametrization of the heat fluxes. The linear fit for the latent heat is $4.97 W m^{-2} K^{-1} \Delta T - 77.28 W m^{-2}$ and for the sensible heat $1.18 W m^{-2} K^{-1} \Delta T - 17.49 W m^{-2}$. The corresponding ΔT^4 fit are $7.5 \cdot 10^{-5} W m^{-2} K^{-4} \Delta T^4$ and $2 \cdot 10^{-5} W m^{-2} K^{-4} \Delta T^4$ for the latent and sensible heat, respectively.

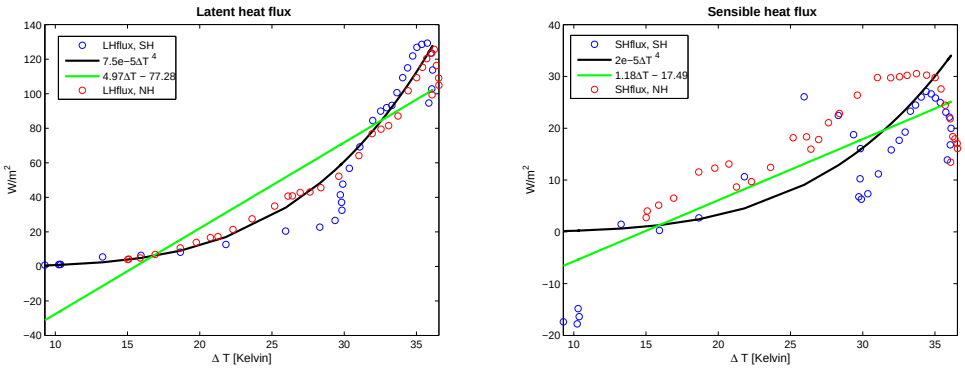

(a) Latent heat flux

(b) Sensible heat flux

Figure 6.1: Annually- and zonally-averaged latent and sensible heat calculated in CAM3 (red and blue dots). (a) Blue dots are southern hemisphere(SH) values and red dots are northern hemisphere(NH) values. (a) and (b) A linear fit (green solid line) and a ΔT^4 fit (black solid line) are also included. For the linear fit the proportionality constants are $4.97 W m^{-2} K^{-1} \Delta T - 77.28 W m^{-2}$ and $1.18 W m^{-2} K^{-1} \Delta T - 17.49 W m^{-2}$ for the latent and sensible heat respectively, and for the ΔT^4 fit the proportionality constants are $7.5 \cdot 10^{-5} W m^{-2} K^{-4}$ and $2 \cdot 10^{-5} W m^{-2} K^{-4}$

The ΔT^4 parametrization of the latent heat is remarkably accurate (see figure 6.1(b)), especially for the NH flux values. This result is surprising considering the linear specific humidity dependence and the many constants used in

the parametrization of the latent heat in CAM3. Here it is worth noting that the ΔT^4 parametrization only requires one constant. For the sensible heat flux neither the linear nor the ΔT^4 fit have much accuracy, but the linear fit is somewhat better than the ΔT^4 fit.

The total convective heat flux, i.e. the latent plus the sensible heat flux, is shown in figure 6.2. The results are presented as described for the latent and sensible heat flux results. The linear fit is $6.15 W m^{-2} K^{-1} \Delta T - 94.77 W m^{-2}$ and the ΔT^4 fit is $9 \cdot 10^{-5} W m^{-2} K^{-4} \Delta T^4$ for the total heat flux. The latent heat flux, being the larger, dominates the sensible heat flux, making the ΔT^4 parametrization of convective heat flux more suitable than the more common linear approach (figure 6.2(a)).

Both the linear fit and the ΔT^4 fit are less accurate at the equator (see figure 6.2(b)). The reasons for the local minimum in the convective heat flux at the equator are complex and related to the extensive deep clouds associated with the ITCZ, the weaker winds in the area and warm SSTs (Seager et al., 2003). Such processes are too complex to capture with a simple temperature dependence.

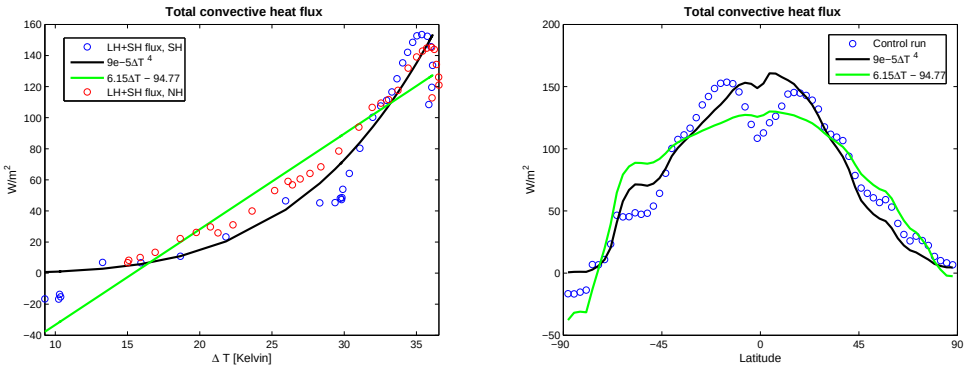

(a) Total convective heat flux vs. ΔT

(b) Total convective heat flux vs. latitude

Figure 6.2: Annually- and zonally-averaged total convective heat flux (latent plus sensible heat) from CAM3 (red and blue dots). Blue dots are Southern Hemisphere (SH) values and red dots are Northern Hemisphere (NH) values. (b) Blue dots are CAM3 values. A linear fit (green solid line) and a ΔT^4 fit (black solid line) are also included. The proportionality constants are $6.15 W m^{-2} K^{-1} \Delta T - 94.77 W m^{-2}$ and $9 \cdot 10^{-5} W m^{-2} K^{-4}$ for the linear and the ΔT^4 fit, respectively

Perturbed SSTs

The convective heat flux changes between the different runs in CAM3 as a result of the altered SST. Table 6.1 shows the different parametrization

of the convective heat for all the CAM3 runs. The 2K run, 2K-lowlat run and the 2K-tropics run have almost the same values for the proportionality constants. The same is the case for the control run, the 2K-highlat run and the Minus 2K-highlat run. Since we do not want to take feedback mechanisms into account when choosing parameter values, the value of the proportionality constant, k, is set to equal the control run value. Thus we take k=$9 \cdot 10^{-5} Wm^{-2}K^{-4}$ for all the AMEP runs.

6.2.2 The constant parameter option

Trenberth et al. (2009) made a global annual mean energy budget for the Earth using satellite measurements from the CERES data sets. The CERES data are from the March 2000 to May 2004 period.

The emitted radiation from the surface was calculated to be $396 Wm^{-2}$ and the OLR at TOA was calculated to be $239 Wm^{-2}$ of which $40 Wm^{-2}$ came from surface radiation passing through the atmospheric window. Assuming the surface radiates as a blackbody, the global annual mean atmospheric emissivity, ϵ, can be calculated as

$$\sigma T_s^4 = 396 Wm^{-2}$$

$$(1-\epsilon)\sigma T_s^4 = 40 Wm^{-2}$$

$$\epsilon = 1 - \frac{40 Wm^{-2}}{396 Wm^{-2}} = 0.90$$

The incoming solar radiation equals $341 Wm^{-2}$ for which $79 Wm^{-2}$ is reflected back to space by clouds and the atmosphere. This gives an atmospheric reflectivity R = 0.23.

$78 Wm^{-2}$ of the remaining part of the incoming solar radiation, i.e. $262 Wm^{-2}$, is absorbed by the atmosphere, corresponding to an atmospheric absorptivity A = 0.298≃0.3

For the convective heat flux parametrization, the proportionality constant k, is set to $9 \cdot 10^{-5} Wm^{-2}K^{-4}$ determined in section 6.2.1.

Assuming the calculated parameters stay constant for all latitudes, the energy balance equation for the atmospheric column in Box i can be written as

$$F_i(1-R)A + k(T_{si} - T_i)^4 - 2\epsilon\sigma T_i^4 + \epsilon\sigma T_{si}^4 - \zeta_i = 0 \qquad \text{(Box } i\text{)} \qquad (6.4)$$

where ϵ=0.9, R=0.23, A=0.3 and k=$9 \cdot 10^{-5} Wm^{-2}K^{-4}$.

The calculations used to find the maximum entropy production are as described in the previous section where

$$\zeta_i = F_i(1-R)A + k(T_{si} - T_i)^4 - 2\epsilon\sigma T_i^4 + \epsilon\sigma T_{si}^4 \qquad \text{(Box } i\text{)} \qquad (6.5)$$

Run	Latent Heat	Sensible Heat	Total Convective Heat
Control			
linear fit	$4.97_{Wm^{-2}K^{-1}}\Delta T$-$77.28_{Wm^{-2}}$	$1.18_{Wm^{-2}K^{-1}}\Delta T$-$17.49_{Wm^{-2}}$	$6.15_{Wm^{-2}K^{-1}}\Delta T$-$94.77_{Wm^{-2}}$
ΔT^4 fit	$7.5{\cdot}10^{-5}{}_{Wm^{-2}K^{-4}}\Delta T^4$	$2{\cdot}10^{-5}{}_{Wm^{-2}K^{-4}}\Delta T^4$	$9{\cdot}10^{-5}{}_{Wm^{-2}K^{-4}}\Delta T^4$
2K			
linear fit	$5.56_{Wm^{-2}K^{-1}}\Delta T$-$89.62_{Wm^{-2}}$	$1.28_{Wm^{-2}K^{-1}}\Delta T$-$20.89_{Wm^{-2}}$	$6.83_{Wm^{-2}K^{-1}}\Delta T$-$110.51_{Wm^{-2}}$
ΔT^4 fit	$8.4{\cdot}10^{-5}{}_{Wm^{-2}K^{-4}}\Delta T^4$	$2.3{\cdot}10^{-5}{}_{Wm^{-2}K^{-4}}\Delta T^4$	$1.07{\cdot}10^{-4}{}_{Wm^{-2}K^{-4}}\Delta T^4$
2K-Lowlat			
linear fit	$5.55_{Wm^{-2}K^{-1}}\Delta T$-$88.73_{Wm^{-2}}$	$1.28_{Wm^{-2}K^{-1}}\Delta T$-$20.89_{Wm^{-2}}$	$6.83_{Wm^{-2}K^{-1}}\Delta T$-$109.08_{Wm^{-2}}$
ΔT^4 fit	$8.2{\cdot}10^{-5}{}_{Wm^{-2}K^{-4}}\Delta T^4$	$2.3{\cdot}10^{-5}{}_{Wm^{-2}K^{-4}}\Delta T^4$	$1.07{\cdot}10^{-4}{}_{Wm^{-2}K^{-4}}\Delta T^4$
2K-Tropics			
linear fit	$5.45_{Wm^{-2}K^{-1}}\Delta T$-$87.09_{Wm^{-2}}$	$1.30_{Wm^{-2}K^{-1}}\Delta T$-$20.44_{Wm^{-2}}$	$6.75_{Wm^{-2}K^{-1}}\Delta T$-$107.53_{Wm^{-2}}$
ΔT^4 fit	$8.2{\cdot}10^{-5}{}_{Wm^{-2}K^{-4}}\Delta T^4$	$2.2{\cdot}10^{-5}{}_{Wm^{-2}K^{-4}}\Delta T^4$	$1.05{\cdot}10^{-4}{}_{Wm^{-2}K^{-4}}\Delta T^4$
2K-Highlat			
linear fit	$4.95_{Wm^{-2}K^{-1}}\Delta T$-$77.28_{Wm^{-2}}$	$1.17_{Wm^{-2}K^{-1}}\Delta T$-$17.60_{Wm^{-2}}$	$6.12_{Wm^{-2}K^{-1}}\Delta T$-$94.88_{Wm^{-2}}$
ΔT^4 fit	$7.7{\cdot}10^{-5}{}_{Wm^{-2}K^{-4}}\Delta T^4$	$2{\cdot}10^{-5}{}_{Wm^{-2}K^{-4}}\Delta T^4$	$9.6{\cdot}10^{-5}{}_{Wm^{-2}K^{-4}}\Delta T^4$
Minus 2K-Highlat			
linear fit	$4.98_{Wm^{-2}K^{-1}}\Delta T$-$76.72_{Wm^{-2}}$	$1.17_{Wm^{-2}K^{-1}}\Delta T$-$16.89_{Wm^{-2}}$	$6.14_{Wm^{-2}K^{-1}}\Delta T$-$93.62_{Wm^{-2}}$
ΔT^4 fit	$7.7{\cdot}10^{-5}{}_{Wm^{-2}K^{-4}}\Delta T^4$	$2{\cdot}10^{-5}{}_{Wm^{-2}K^{-4}}\Delta T^4$	$9.7{\cdot}10^{-5}{}_{Wm^{-2}K^{-4}}\Delta T^4$

Table 6.1: Parametrization of latent and sensible heat flux in CAM3 for the control run and all perturbed SST runs, using linear and ΔT^4 approximations.

is used for the meridional heat divergence.

The atmospheric meridional heat transport is calculated as

$$F_\phi = 2\pi R_E^2 \int_{-\frac{\pi}{2}}^{\frac{\pi}{2}} \zeta \; cos(\phi) \; \mathrm{d}\phi \tag{6.6}$$

where F_ϕ is the meridional heat transport as a function of latitude. F_ϕ is given in petawatts (PW).

Here it is worth noting that this definition is slightly different than the one defined in Paltridge's model (section 4.1.4), for which the boxes were defined to have the same surface area. In this model the boxes have the same latitudinal width, dϕ.

The AMEP result using constant parameters

The AMEP results using constant parameters, are shown in figure 6.3. The mean properties of the atmosphere are captured in a satisfactory way.

The atmospheric temperature (black, solid line) is seen in figure 6.3(a). Also included are the surface temperatures from CAM3 used as the boundary forcing in AMEP (blue, solid line). The atmospheric temperature is much colder than the surface temperature. This is to be expected since the mean radiative atmospheric temperature of 255K is much colder than the surface temperature of 288K (Hartmann, 1994, Ch. 2) The only exception is over Antarctica where the surface temperatures are extremely cold. The atmospheric temperature profile is also flatter, showing less latitudinal variation than the surface temperature profile.

The convective heat flux, F_c, is seen in figure 6.3(b). The convective heat flux is bell-shaped, with maximum values of $95 W m^{-2}$in the tropics. The flux is not quite symmetric about the equator, with larger values in the NH. The characteristic local minimum in latent heat at the equator does not appear. This was not expected though since the parametrization method failed to capture this minimum as well.

The meridional heat divergence, ζ, is seen in figure 6.3(c). The shape of ζ is dominated by the convective heat flux. This is also observed in the real atmosphere (Hartmann, 1994, Ch. 6).

Figure 6.3(d) shows the northward heat transport (eqn. 6.6). Two maxima are seen at 35°N/S with a transport of approximately 7PW. The transport is expected to peak with a maximum of approximately 4-5PW(Hartmann, 1994, Ch. 6) . The high values seen in figure 6.3(d) indicates that the atmosphere gains too much heat at low latitudes. This is a consequence of the radiation budget in AMEP, as explained in the following section.

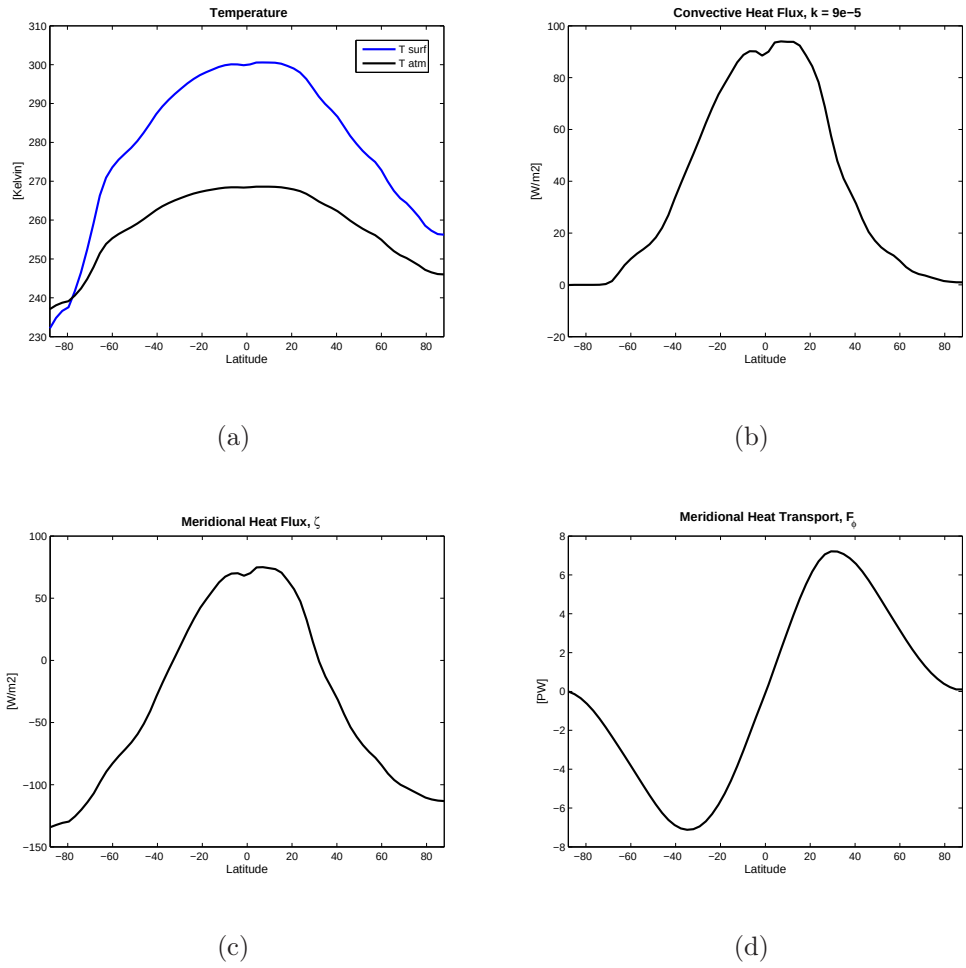

Figure 6.3: (a) The Atmospheric (black line) and surface (blue line) temperature,(b) the convective heat flux, (c) the meridional heat divergence,ζ, and (d) the meridional heat transport calculated using AMEP with constant parameters A, R, ϵ and k. The surface temperature acts as a boundary forcing and is the same regardless of the parameters used.

The radiative energy budget

In the real atmosphere the stratosphere is in approximately radiative equilibrium while the troposphere has a net radiative cooling rate of about $1.5 K day^{-1}$ (Hartmann, 1994, Ch. 3). Considering the atmosphere as one layer, a radiative loss is expected. The radiative loss is balanced by the convective heat flux from the surface and the meridional heat transport from low to high latitudes. The radiation budget for AMEP is shown in figure 6.4(a). The figure shows the total sum of emitted radiation from the atmosphere and the total absorbed radiation, which is the sum of the absorbed solar radiation and the absorbed radiation emitted from the surface. Calculated values from Trenberth et al. (2009) show that the atmosphere emits $502 W m^{-2}$ and

absorbs $434 W m^{-2}$ annually- and globally-averaged. The numbers are not too different from what is seen in figure 6.4(a), but indicate that too much radiation is absorbed in AMEP.

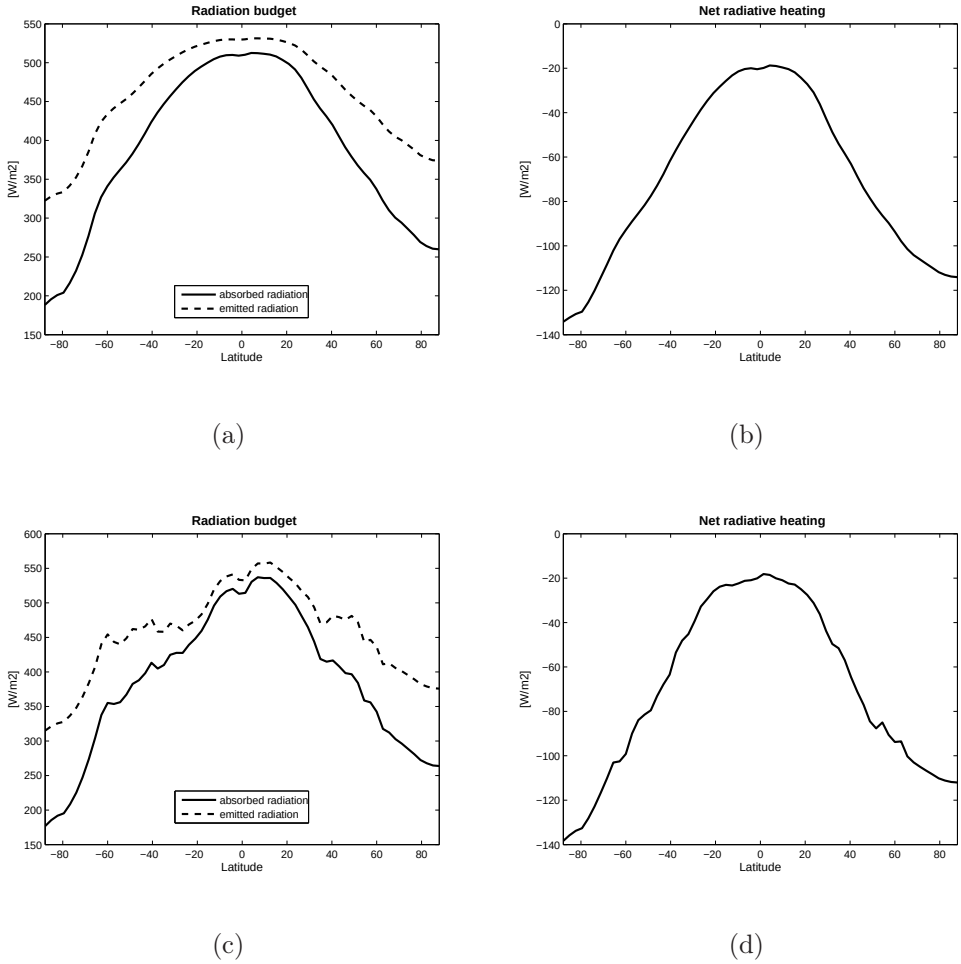

Figure 6.4: (a) The radiation budget in AMEP using constant parameter values for all boxes. The absorbed radiation (solid line) is the sum of the absorbed solar radiation and the absorbed terrestrial radiation in the atmosphere. The emitted radiation (dashed line) is the total radiation emitted from the atmosphere in both directions. (b) The radiative heating budget is the absorbed radiation minus the emitted radiation in AMEP. The atmosphere experiences a radiative cooling for all latitudes. (c) and (d) The radiation budget as described above, using zonally-varying parameter values in AMEP.

The large latitudinal variation in the radiation budget is unexpected. The profile of the total radiation budget in AMEP is similar to the surface temperature profile. In the real atmosphere the radiation loss is approximately $100 W m^{-2}$ (Hartmann, 1994) and does not exhibit great variation between

latitudes. The same is true of CAM3 (see section 7.1.2). The latitudinal deviation in the radiation budget causes too small radiative loss at low latitudes, resulting in large heat transport.

6.2.3 The zonally-varying parameter option

The numbers calculated from the work by Trenberth et al. (2009) are globally- and annually-averaged values, while AMEP is a zonally- and annually-averaged model. Applying parameters calculated from global mean conditions to zonal mean conditions can cause errors since the emissivity, the absorptivity and the reflectivity of the atmosphere are not expected to stay constant over different latitude zones. Using a single layer solar radiation model and data from CAM3 provides another method of calculating the parameters, ϵ, A and R, used in the AMEP model.

The shortwave parameters

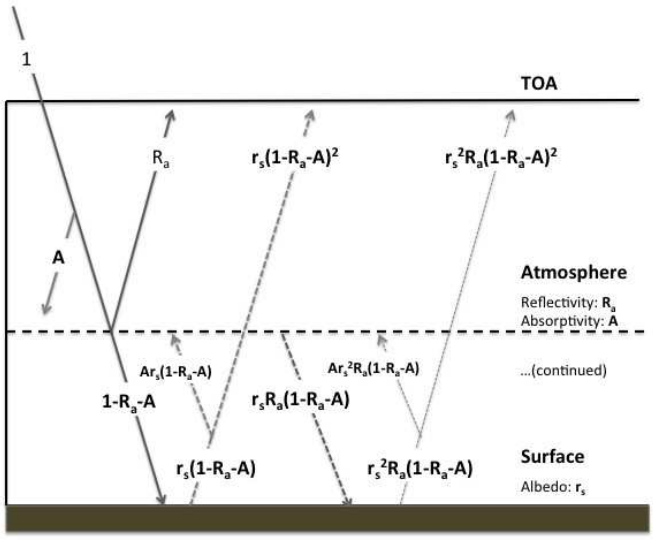

Figure 6.5: Schematic representing the first two reflections in a single layer solar radiation model. Moving from left to right, the arrows represent the radiative fluxes associated with the incident solar radiation, first reflection, and second reflection. A, R_a, and r_s are the atmospheric absorption fraction during a single pass through the atmosphere, the fraction of reflection, and the surface albedo respectively. Figure adapted from Donohoe and Battisti (2010).

The short wave parameter calculations are based on the work of Donohoe and Battisti (2010). Figure 6.5 shows a single layer atmosphere-surface system for a given latitude zone. Three processes are accounted for: the atmospheric reflection (R_a), the atmospheric absorption (A) and surface reflection (r_s).

Each process is assumed isotropic. The incoming solar radiation in each latitude zone equals one unit and R_a, A and r_s are fractions of the insolation unit. Only two reflections are shown in figure 6.5, but these processes are repeated infinitely. Using the one layer model, the total fraction of reflected radiation at TOA,$f\uparrow_{TOA}$, can be written as a sum

$$\begin{aligned} f\uparrow_{TOA} &= R_a + r_s(1-R_a-A)^2 + {r_s}^2 R_a(1-R_a-A)^2 + {r_s}^3 {R_a}^2(1-R_a-A)^2 + ... \\ &= R_a + r_s(1-R_a-A)^2\big[1 + r_s R_a + (r_s R_a)^2 + ...\big] \\ &= R_a + r_s\frac{(1-R_a-A)^2}{1-R_a r_s} \end{aligned} \tag{6.7}$$

Similar infinite series can be obtained for the total fraction of downwelling,$f\downarrow_{surf}$, and upwelling flux,$f\uparrow_{surf}$, of solar radiation at the surface

$$\begin{aligned} f\downarrow_{surf} &= (1-R_a-A) + r_s R_a(1-R_a-A) + {r_s}^2 {R_a}^2(1-R_a-A) + ... \\ &= (1-R_a-A)\big[1 + r_s R_a + (r_s R_a)^2 + ...\big] \\ &= \frac{(1-R_a-A)}{1-R_a r_s} \end{aligned} \tag{6.8}$$

$$\begin{aligned} f\uparrow_{surf} &= r_s(1-R_a-A) + {r_s}^2 R_a(1-R_a-A) + {r_s}^3 {R_a}^2(1-R_a-A) + ... \\ &= r_s(1-R_a-A)\big[1 + r_s R_a + (r_s R_a)^2 + ...\big] \\ &= r_s\frac{(1-R_a-A)}{1-R_a r_s} = r_s f\downarrow_{surf} \end{aligned} \tag{6.9}$$

If **F** is the insolation in for a given latitude zone, the upwelling solar flux at TOA is $F(TOA)\uparrow = \mathbf{F}f\uparrow_{TOA}$, the downwelling solar flux at the surface and the upwelling solar flux at the surface are $F(0)\downarrow = \mathbf{F}f_{surf}\downarrow$ and $F(0)\uparrow = \mathbf{F}f\uparrow_{surf}$, respectively. For the upwelling and downwelling fluxes, data from CAM3 is used. The result is shown in Figure 6.6

The longwave parameter

An estimate for the atmospheric emissivity can be calculated from the OLR at TOA using CAM3 data. The OLR from CAM3 for a given latitude zone i can be written as

$$OLR_i = \epsilon_i \sigma T_i^4 + (1-\epsilon_i)\sigma T_{si}^4 \tag{6.10}$$

where T is the mean radiative temperature of the atmosphere and T_s is the surface temperature. OLR data from the control run and the 2K run were used. The data are from the first day of the CAM3 run in which the SST differs between the two runs, while all the other parameters are assumed to be unchanged. The assumption is justified because of the short running time of the model (6hrs) compared to the typical adjustment time of the

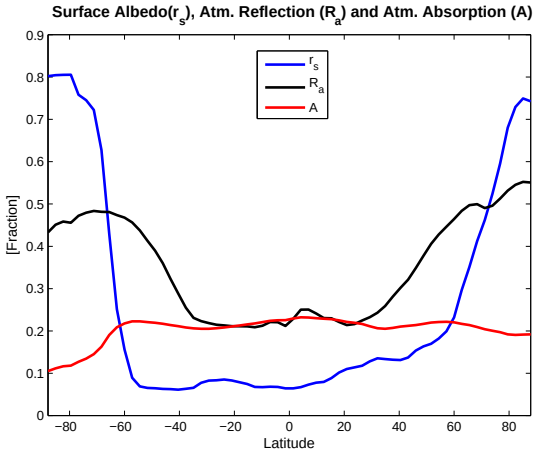

Figure 6.6: Annually- and zonally-averaged surface albedo r_s, atmospheric reflection R_a and atmospheric absorption A. The parameter values are derived from CAM3 using a single layer solar radiation model (see text for details)

atmosphere ($\mathcal{O}$(day)). For a given latitude zone i, the difference in OLR can be written as

$$OLR_{i,2K} - OLR_{i,control} = \left(\epsilon_i \sigma T_i^4 + (1-\epsilon_i)\sigma T_{si}^4\right)_{2K} - \left(\epsilon_i \sigma T_i^4 + (1-\epsilon_i)\sigma T_{si}^4\right)_{control}$$

$$= \left((1-\epsilon_i)\sigma T_{si}^4\right)_{2K} - \left((1-\epsilon_i)\sigma T_{si}^4\right)_{control}$$

$$\epsilon_i = 1 - \frac{OLR_{i,2K} - OLR_{i,control}}{\sigma(T_{si,2K}^4 - T_{si,control}^4)} \tag{6.11}$$

Although this is a crude estimate, the mean value equals 0.9 and coincides with the value determined from Trenberth et al. (2009). The emissivity result is shown in Figure 6.7. The calculation method fails when the surface temperature, T_s, in the two runs equal, which happens at high latitudes. For those areas the mean value is used.

The AMEP result using zonally varying parameters

The energy balance equation for the atmospheric column in Box i using this approach is

$$F_i\left(A_i + A_i r_{si}\frac{(1-R_{ai}-A_i))}{1-r_{si}R_{ai}}\right) + k(T_{si}-T_i)^4 - 2\epsilon_i\sigma T_i^4 + \epsilon_i\sigma T_{si}^4 - \zeta_i = 0 \quad \text{(Box } i\text{)} \tag{6.12}$$

The calculations used to find the maximum entropy production will be as described in the section 6.1, using

$$\zeta_i = F_i\left(A_i + A_i r_{si}\frac{(1-R_{ai}-A_i))}{1-r_{si}R_i}\right) + k(T_{si}-T_i)^4 - 2\epsilon_i\sigma T_i^4 + \epsilon_i\sigma T_{si}^4 \quad \text{(Box } i\text{)} \tag{6.13}$$

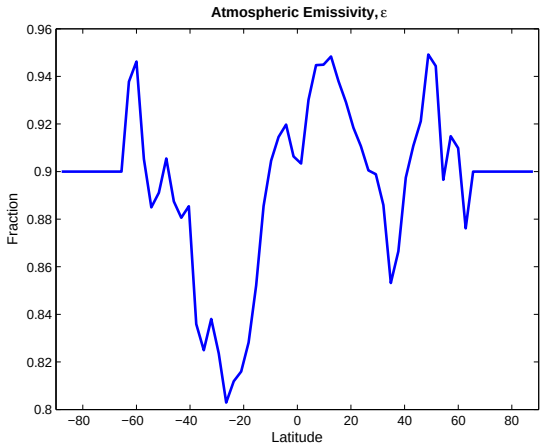

Figure 6.7: The zonally averaged atmospheric emissivity. The calculation used fails for the highest latitudes due to equal T_s in the two runs. For those latitudes the mean value of 0.9 is used

for the meridional heat divergence. The difference plot for AMEP between using the zonally-varying parameters and the constant parameters, are shown in figure 6.8. The differences between the two runs are small for all outputs. The reason for the small changes can be seen in figure 6.4. The parameters, ϵ, A and R, influence the radiation budget in each box. In spite of the differences in the radiation budget for the constant parameter AMEP run and the zonally-varying parameter AMEP run (see figure 6.4(a) and (c)), the net radiative cooling stays the same in both runs (see figure 6.4(b) and (d)).

When comparing the different results between the two parameter options in the altered SST run (not shown), no significant difference between the two options are seen. Due to the small changes in the results using zonally-varying parameters, instead of constant parameters, the constant parameters are used from now on. The reason for choosing the constant parameter option is that it makes the results derived from AMEP even easier to understand.

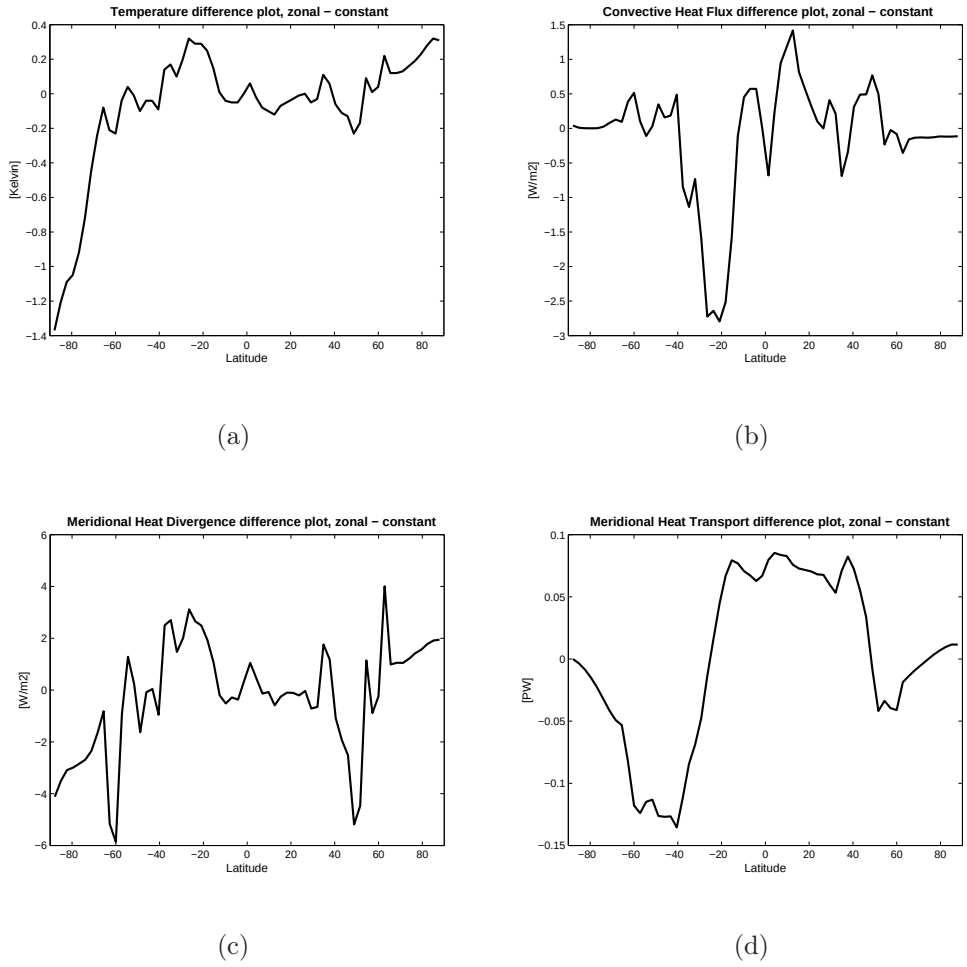

Figure 6.8: The difference between the zonally-averaged parameter run and the constant parameter AMEP run in (a) atmospheric temperature, (b) convective heat flux, F_c, (c) the meridional heat divergence, ζ, and (d) the meridional heat transport, F_ϕ. The differences are all small.

Chapter 7

Results

In order to conduct a perturbed SST comparison it is essential to determine comparable fields between AMEP and CAM3 (sections 7.1.1 and 7.1.2). The following examination of a control run comparison of the two models (section 7.1.3) will provide grounds for the subsequent perturbed SST comparison (section 7.2).

7.1 The control run comparison

AMEP is an annually- and zonally-averaged model, which is necessary because the atmosphere needs to be in approximately steady state, in order to apply the MEP principle. Consequently the fields from CAM3 used in the comparison need to be annually- and zonally-averaged fields too.

7.1.1 The atmospheric temperature and the convective heat flux in CAM3

The atmospheric temperature and the convective heat flux are default fields in CAM3. CAM3 has 26 atmospheric temperature fields; one for each vertical layer. To make a comparison with the atmospheric temperature in AMEP, the density-weighted average atmospheric temperature, defined in section 5.2, is used. This temperature represents the mean atmospheric temperature in CAM3 and is necessary to use because AMEP only has one mean atmospheric temperature for each atmospheric column. The density-weighted average atmospheric temperature, henceforth referred to as the atmospheric temperature, is shown in figure 7.1(a). Also shown in 7.1(a) is the surface temperature, T_s. The latent heat flux (LH), the sensitive heat flux (SH) and the total convective heat flux (LH + SH) are shown in figure 7.1(b). All fields are 20 year time- and zonally- averaged fields.

The meridional heat divergence and the meridional heat transport in the atmosphere are not field values in CAM3. To make a model intercomparison between AMEP and CAM3, these values need to be determined. To do that, values from the atmospheric energy budget in CAM3 are used.

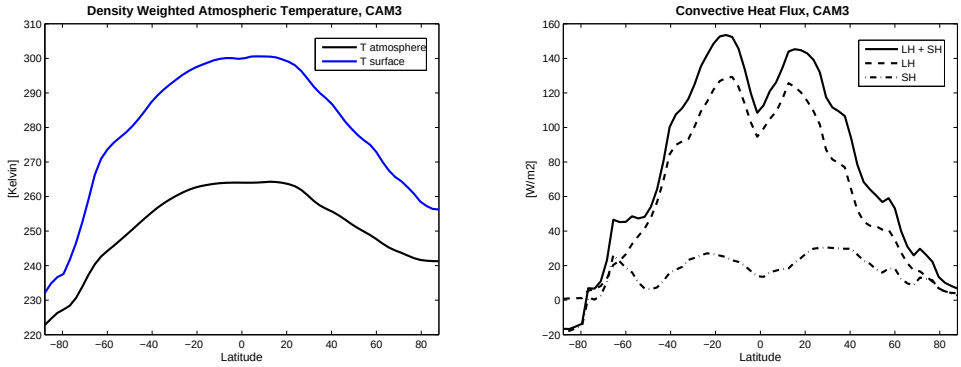

(a) (b)

Figure 7.1: (a) The annually- and zonally-averaged surface temperature (blue line) and density-weighted atmospheric temperature (black line). (b) The annually- and zonally-averaged latent heat flux, LH, (dashed, black line), sensible heat flux, SH, (black, dash-dotted line) and total convective heat flux, LH+SH, (black, solid line).

7.1.2 The energy budget in CAM3

The atmospheric energy balance calculations used in this section are based on the calculations of Hartmann (1994, Ch. 6). The local energy balance of an atmospheric column can be written as

$$\frac{\partial E}{\partial t} = R_A + LH + SH - \zeta \tag{7.1}$$

where $\partial E/\partial t$ is the change of the energy content of an atmospheric column with time, R_A is the net radiative heating, LH is the latent heat release, SH is the sensible heat and ζ is the horizontal energy divergence.

The net radiative heating, R_A, is the difference between the net radiative heating at TOA and the net radiative heating at the surface, i.e.

$$R_A = R_{TOA} - R_{surface} \tag{7.2}$$

The data used from CAM3 is a 20-year annual average, so every atmospheric column is considered to be in energy equilibrium, which means that no energy is stored within the column, i.e.

$$\frac{\partial E}{\partial t} = 0 \tag{7.3}$$

This is used to get an estimate of ζ

$$\zeta = SH + LH + R_A \tag{7.4}$$

The resulting atmospheric energy budget is shown in figure 7.2(a). The atmosphere experiences a net radiative cooling of approximately $100Wm^{-2}$ with only small latitudinal variations. The energy loss is partly balanced by the flux of sensible and latent heat from the surface. The atmosphere gains energy at low latitudes, since the convective heat flux exceeds the radiative energy loss, and loses energy at middle and high latitudes where the convective heat flux is greatly reduced. The energy budget is balanced by the meridional energy transport. The atmospheric energy transport is

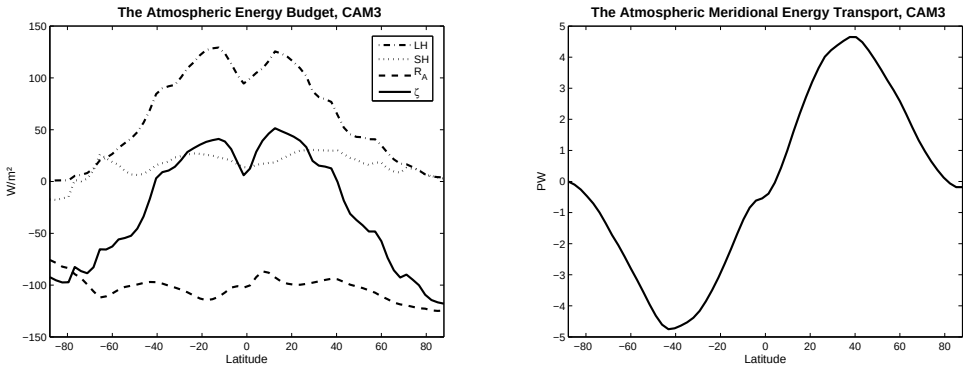

(a) (b)

Figure 7.2: (a) The atmospheric energy budget from the control run in CAM3 includes the latent heat flux, LH,(dash-dotted line), the sensible heat flux, SH, (dotted line), the net radiative heating, R_A, (dashed line) and the horizontal energy divergence, ζ, (solid line) which is calculated as a sum of the other energy budget components. (b) Total meridional energy transport in the atmosphere.

calculated the same way as for the AMEP model (see section 6.2.2), i.e.

$$F_\phi = 2\pi R_E^2 \int_{-\frac{\pi}{2}}^{\frac{\pi}{2}} \zeta \; cos(\phi) \; \mathrm{d}\phi \tag{7.5}$$

where R_E is the radius of the Earth. F_ϕ is a function of latitude, ϕ, given in petawatts(PW) and shown in figure 7.2(b).

7.1.3 AMEP vs. CAM3; a control run comparison

In order to make a comparison between AMEP and CAM3, it is essential to account for differences in the control run results in the two models. The control run fields for AMEP were described in section 6.2.2 and shown in figure 6.3. The difference plots between the AMEP and CAM3 control run results are shown in figure 7.3.

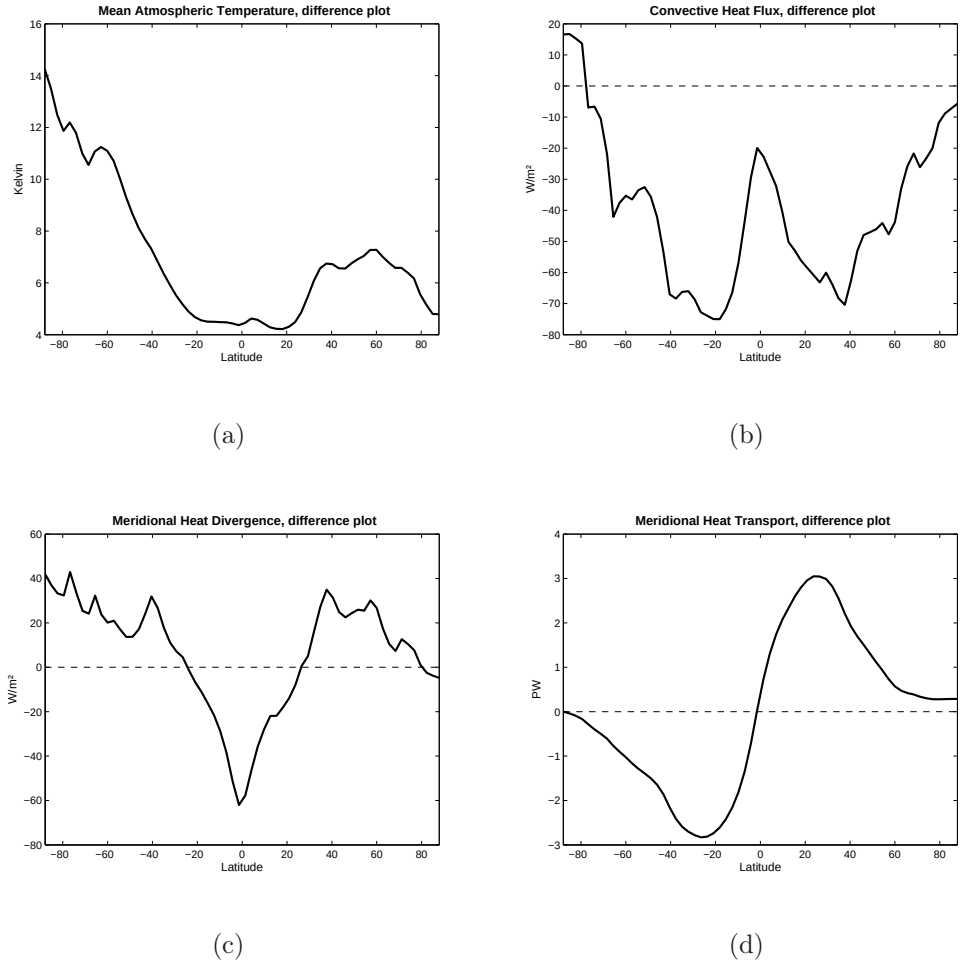

Figure 7.3: AMEP minus CAM3 difference plot. (a) Temperature, (b) Convective heat flux, (c) Meridional heat divergence, (d) Meridional heat transport.

The atmospheric temperature difference plot is seen in figure 7.3(a). The mean atmospheric temperature for AMEP is warmer for all latitudes. The AMEP temperature profile is also much flatter, which results in a greater difference at middle and high latitudes. The greatest differences occur close to Antarctica, where the CAM3 temperatures are extremely cold.

The difference plot for the convective heat flux is seen in figure 7.3(b). The convective flux is smaller and more confined in the tropics in AMEP than in CAM3, which causes large differences at mid-latitudes between the two models. The local minimum in the convective heat flux at the equator seen in CAM3, was not captured in the parametrized heat flux. This results in significant differences between the two models close to the equator as well.

The differences in the atmospheric temperatures and the convective heat fluxes are closely connected. In the parametrization of the convective heat

flux used in the AMEP model, $k(T_s - T)^4$, the same k value as calculated from CAM3 is used. The k value was obtained using precisely the density-weighted atmospheric temperature used in this temperature comparison. The fact that the temperatures in AMEP are warmer than in CAM3 for all latitudes, makes the $k(T_s - T)^4$ term smaller in the AMEP model at all latitudes. This is especially true at middle and high latitudes where the temperature differences are greater. This is reflected in the convective heat flux difference plot which shows such large values, due to the fourth power of the temperature difference used in the parametrization.

The difference in the meridional heat divergence results from the two models is seen in figure 7.3(c). The shape of the meridional heat divergence is highly dependent on the convective heat flux, so the reasons for these differences are the same as the ones mentioned above. For a more thorough discussion of the relation between the changes in the convective heat flux and the changes in ζ see section 7.2.3.

Although the atmosphere gains more convective heat in CAM3 compared to AMEP, the atmosphere gains more heat in total in AMEP due to less radiative cooling (see figure 6.4) at low latitudes as explained in section 6.2.2. The increased energy gain in AMEP is reflected in the meridional transport difference plot (see figure 7.3(d)) for which the AMEP transport is much larger than the transport calculated from CAM3.

Thus there are significant differences between the two models' results. These are especially seen in the convective heat flux, the meridional heat divergence and the meridional heat transport. Although the results differ between AMEP and CAM3, it is the *differences between the perturbed temperature runs and the control run for each model separately* we are interested in. The changes in the models, in response to the altered SST for CAM3 and the altered T_s for the AMEP model, are the most important part of the comparison. The underlying causes for the differences seen above are easily understood and should not hinder the model intercomparison.

7.2 The perturbed SST comparison

To see if AMEP is able to detect shifts in the maximal meridional heat transport due to altered SST, five perturbed surface temperature runs are conducted. The results from each run are then compared to results from the corresponding runs in CAM3.

The different SST runs executed in the study of Graff and LaCasce (2012) are described in detail in section 2.1. For AMEP, the temporally- and zonally-averaged surface temperature fields, T_s, from CAM3 are used in the different runs. The changes in T_s differ from the SST changes imposed. The surface

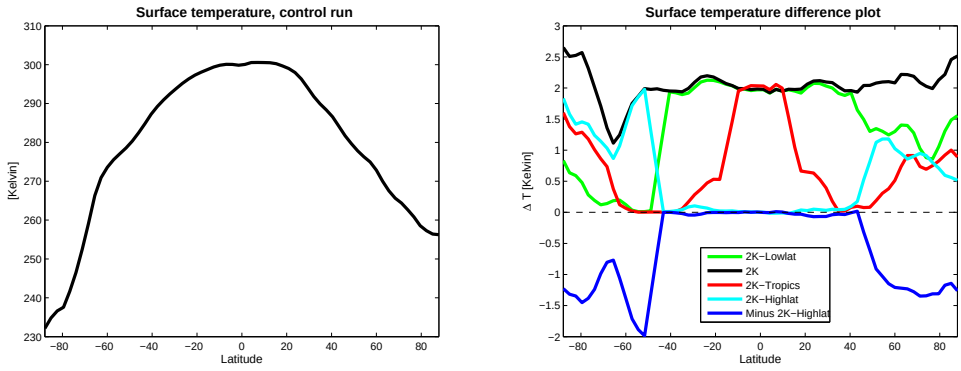

(a) (b)

Figure 7.4: The surface temperatures used as a boundary forcing in AMEP are the temporally and zonally averaged surface temperature fields from CAM3. (a) Temporally- and zonally-averaged surface temperature profile used in the AMEP control run. (b) The difference between the surface temperatures used in the other runs and the control run .

temperatures over the continents and over sea ice are not forced in the CAM3 runs. Some of the energy gained in the atmosphere due to the SST forcing is transported by the atmospheric circulation, resulting in modified surface temperatures also over continents and ice, but the changes are not as distinct as the SST forcing. Also, the changes in the surface temperatures are more evident in the SH due to the greater fraction covered by sea. CAM3 is run until a new equilibrium state is achieved. It is the annually- and zonally-averaged surface temperatures from this state that is used as the T_s forcing in AMEP.

The T_s used in the AMEP control run is seen in figure 7.4(a). The differences in the T_s profiles used in the perturbed T_s runs and the control run are seen in figure 7.4(b). The changes in T_s are not as well defined as the differences seen for the altered SST, but the temperature tendency in the runs is clearly captured.

The perturbed surface temperatures act as a lower boundary forcing in both models. The greatest forcing is in the SH where the fraction covered by ocean is much greater in the NH. For this reason the changes in the results are expected to be greater in the SH than in the NH, which is also seen.

Figures 7.5, 7.6, 7.8 and 7.10 show the differences in the mean atmospheric temperature, the convective heat flux, the meridional heat divergence and the meridional heat transport between the perturbed SST runs and the control run in CAM3 and the perturbed T_s runs and the control run in AMEP.

The results for both models are included in the figures. The differences in the CAM3 results are seen as green, solid lines in all figures and the corresponding AMEP results are seen as blue, solid lines.

The 2K-Lowlat run, the 2K run and the 2K-Tropics run are all heated in the tropics and exhibit some of the same features. The runs are referred to as the *lowlat heating runs* when all of them are included in the description. Also the changes seen in the 2K-Highlat run and the Minus 2K-Highlat run are similar and are described together as the *±2K-Highlat runs*.

7.2.1 The mean atmospheric temperature difference

Figure 7.5 shows the difference between the perturbed runs and the control run in the mean atmospheric temperature for both models. The atmospheric temperature used for the CAM3 results is the density-weighted averaged atmospheric temperature defined in section 5.2. Also included is the differences in T_s, which is the same for both models (red, dashed line).

The 2K-Lowlat run (7.5(a))
The increase in the SST by 2K equatorward of 45°N/S is reflected in T_s. The T_s heating effect is present at all latitudes in the NH, while it is small at high latitudes in the SH, except over Antarctica. The imposed T_s gradient at 45° is much sharper in the SH compared to the NH. The mean atmospheric temperatures in CAM3 warm by 2.6 K in the tropics and decrease smoothly at higher latitudes. The temperatures in AMEP warm less, with a constant warming of 1.6K equatorward of 45°N/S. At higher latitudes, the warming in AMEP equals the warming seen for T_s in the NH and is greater than what is seen for T_s in the SH.

The 2K run (7.5(b))
There is a nearly constant 2K warming in T_s for all latitudes, except at high latitudes in the SH. The changes seen in the 2K run resemble the 2K-Lowlat run. The warming in the two models is exactly the same as seen in the 2K-Lowlat run, except that the warming occurs over a larger area. The reduction in heating at high latitudes is also less than what was seen in the 2K-Lowlat run and is less than the warming in T_s for both models.

The 2K-Tropics run (7.5(c))
T_s is increased by 2K in the tropics, with the imposed SST gradient at 15°N/S clearly seen. The change in the T_s is nearly zero at mid-latitudes, with an increase at high latitudes. The changes seen in the atmospheric temperature in the tropics resemble the changes seen in the heated area in the two previous runs except that the heating is less in AMEP, approximately 1.3K. All temperature profiles show warming at high latitudes.

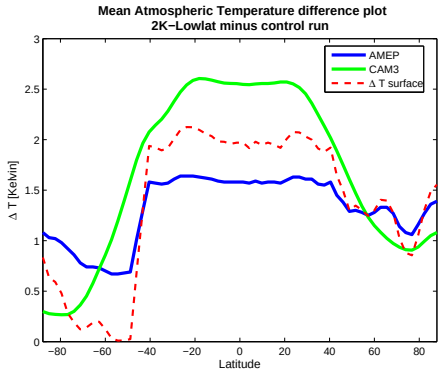

(a) 2K-Lowlat

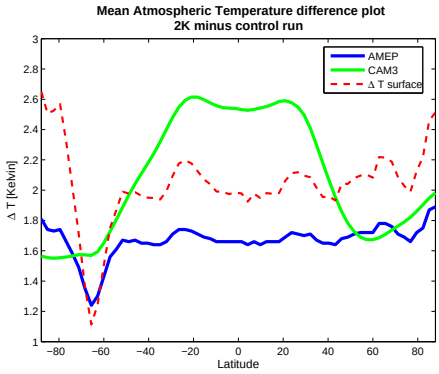

(b) 2K

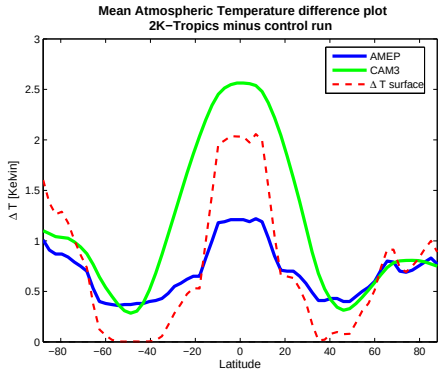

(c) 2K-Tropics

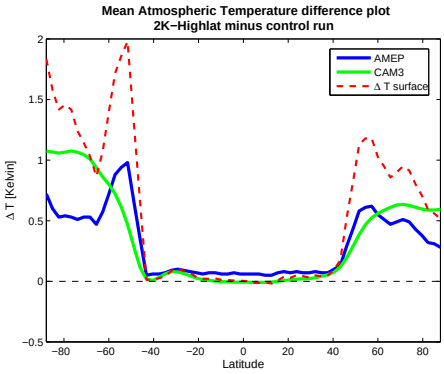

(d) 2K-Highlat

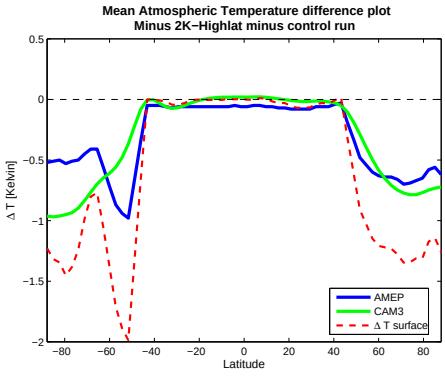

(e) Minus 2K-Highlat

Figure 7.5: The difference in the mean atmospheric density-weighted temperature between the perturbed SST runs and the control run for CAM3 (green, solid line). The difference in the atmospheric temperature between the perturbed T_s runs and the control run for the AMEP model (blue, solid line). Also included is the difference in the zonal mean surface temperature field, T_s, from CAM3 (red, dashed line).

The ±2K-Highlat runs (7.5(d),7.5(e))
The changes seen in the 2K-Highlat and the Minus 2K-Highlat run look almost exactly the same, except for the sign difference. T_s is increased (decreased for the Minus 2K-Highlat run) by 2K at 45°S and by approximately 1.2K at 45°N. The changes in T_s are less at high latitudes. Temperatures in AMEP also exhibit greater warming (cooling) in the SH than in the NH, but the changes are less than in T_s, with approximately 1K warming (cooling) at 45°S and 0.6K at 45°N. The CAM3 temperatures also increase (decrease) at 45°N/S, but the changes are not as sharp as in the surface temperature profiles. There is a 1K warming (cooling) south of 45°S and 0.6K warming (cooling) north of 45°N. The CAM3 temperatures do not decrease (increase) at high latitudes. None of the temperature profiles show any changes equatorward of 45°N/S.

Generally the atmospheric temperature in AMEP exhibits the same shape as the changes in T_s, although the changes in the AMEP model are somewhat smaller. The changes in CAM3 exhibit a smoother profile than what is seen for both AMEP and T_s. The lowlat heating runs all show a greater atmospheric temperature warming than the increase in the surface temperature in the CAM3 runs. This feature is not seen in AMEP. For the ± 2K-Highlat runs both AMEP and CAM3 show smaller changes than seen in T_s.

7.2.2 The convective heat flux difference

The differences in convective heat flux (CHF) are shown in figure 7.6. Also included are the changes in T_s (red, dashed line) described in the previous section.

The 2K-Lowlat run (7.6(a))
The CHF is increased equatorward of 45°N/S and reduced poleward of 45°N/S in both models. The reduction is seen in both hemispheres for CAM3 and only in the SH for AMEP. The strong gradients in the CHF changes are located at the same latitude as the changes in T_s. The changes are large for CAM3, especially in the SH. For AMEP the greatest increase in CHF is seen at low latitudes, with nearly constant values. The CHF is reduced at mid-latitudes in the SH and are unaltered at middle and high latitudes in the NH.

The 2K run (7.6(b))
The results for the 2K run resemble what is seen in the 2K-Lowlat run, but the magnitude of change in the 2K-run is smaller for CAM3. CAM3 shows two large peaks in the increased CHF at mid-latitudes and a reduction at higher latitudes. AMEP exhibits an increase in CHF at all latitudes, except at high latitudes in the SH. The greatest increase in CHF with AMEP is seen at low latitudes, with less variation than what is seen with CAM3. Still, the two peaks at mid-latitudes are present, as seen in CAM3.

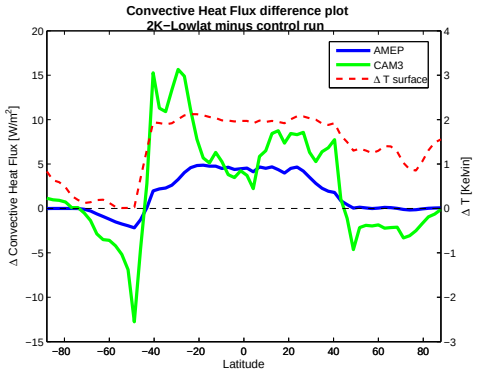

(a) 2K-Lowlat

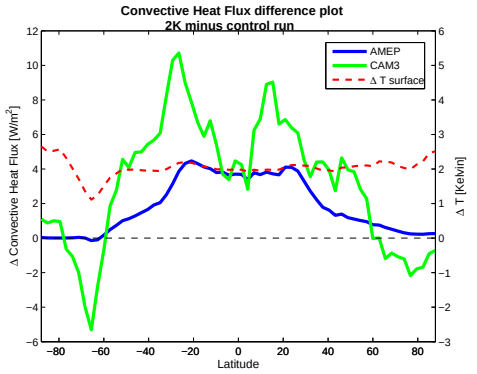

(b) 2K

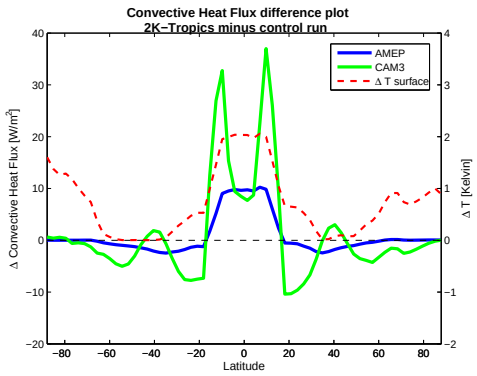

(c) 2K-Tropics

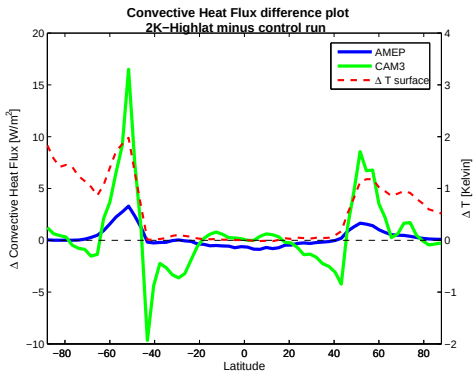

(d) 2K-Highlat

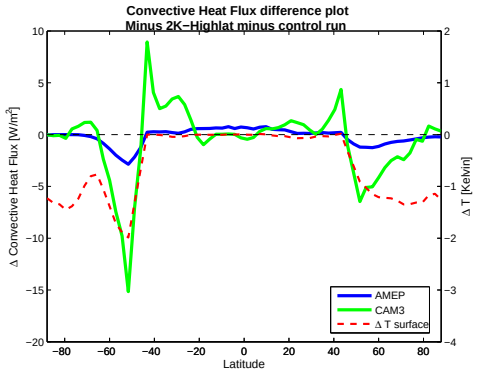

(e) Minus 2K-Highlat

Figure 7.6: The difference in the Convective Heat Flux (CHF) between the perturbed SST runs and the control run for CAM3 (green, solid line) and between the perturbed T_s runs and the control run for the AMEP model (blue, solid line). Also included is the difference in the zonal mean surface temperature field, T_s (red, dashed line), from CAM3. Note the two different y-axis.

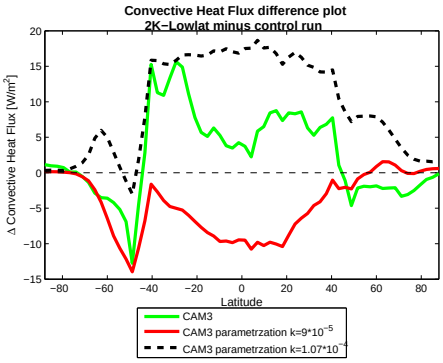

(a) 2K-Lowlat

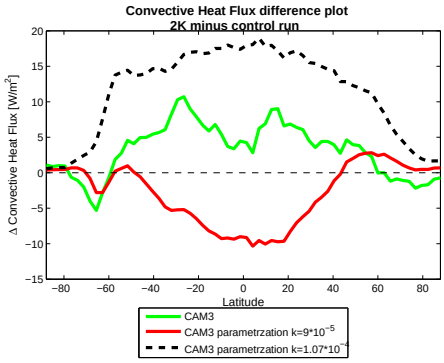

(b) 2K

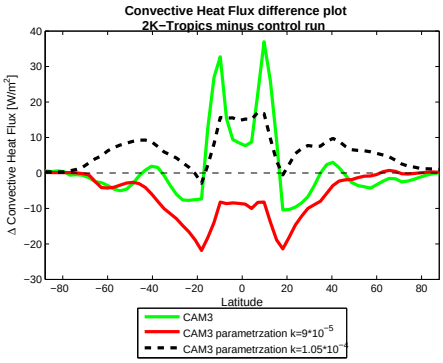

(c) 2K-Tropics

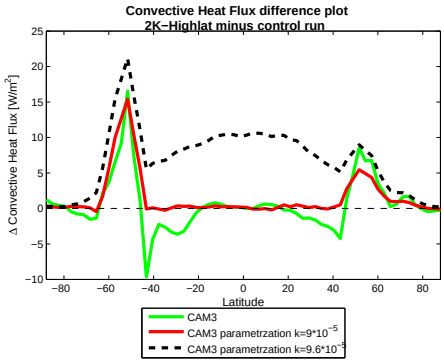

(d) 2K-Highlat

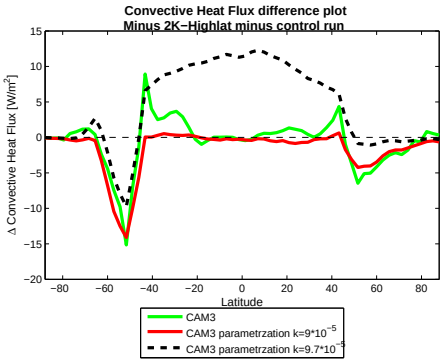

(e) Minus 2K-Highlat

Figure 7.7: The difference in the Convective Heat Flux (CHF) between the perturbed SST runs and the control run for CAM3 (green, solid line). Also included are the CHF parametrization $F_c = k \cdot (T_s - T)^4 \ \mathrm{sign}(T_s - T)$ (red, solid line), where k=$9{\cdot}10^{-5} Wm^{-2}K^{-4}$ and the CHF parametrization using k values from table 6.1 (black, dashed line). The CHF parametrization is described in detail in section 5.2 and in section 6.2.1.

The 2K-Tropics run (7.6(c))
The 2K-Tropics run shows the greatest increase in CHF of all the runs with both CAM3 and AMEP. The changes in CHF, for CAM3, peak at 10°N/S, with an increase of $37 Wm^{-2}$ and $33 Wm^{-2}$, respectively. The changes are less, close to the equator. There is a sharp drop in CHF at 15°N/S and it is reduced compared to the control run. The location of the strong CHF gradients are the same as the changes in T_s. The changes in CHF are also smaller at higher latitudes. It is worth noting that the changes in CAM3 for the 2K-Tropics run are greater in the NH. This is quite the opposite than what is seen for the other runs. AMEP also exhibits an increase in CHF equatorward of 15°N/S and a reduction poleward of 15°N/S. The changes however are much smaller than seen in CAM3 and the local minimum at equator in CAM3 is not present in AMEP.

The ±2K-Highlat runs (7.6(d),7.6(e))
The changes in CHF are nearly zero at low latitudes where T_s is unaltered. The CHF is reduced (increased in the Minus 2K-Highlat run) in CAM3 between 20°N/S-40°N/S. This reduction (increase) is not seen in AMEP or in T_s. At 45°N/S the CHF increases (decreases) rapidly in both models, with the greatest changes seen for CAM3. The changes in the CHF are small at high latitudes

Thus there is a clear tendency in the results: where there is surface and atmospheric heating, the fluxes of latent and sensible heat increase. AMEP and CAM3 exhibit the same tendencies, but CAM3 shows much more structure, rapid shifts and greater changes in CHF than does AMEP. For both models the changes seen in CHF and T_s are connected and often occur at the same location.

The CHF parametrization

The CHF parametrization used in AMEP was determined using a vertical MEP model (section 5.2). The parametrized CHF was compared to CHF fields from CAM3 (section 6.2.1). The result showed that the parametrization used for CHF succeeded in capturing the main CHF field in CAM3 (see figure 6.2). However, changes in CHF differ considerably in the two models, as seen in the results discussed above. In order to find out why, the parametrized CHF, as used in AMEP, is tested using CAM3 data and the results are compared to CHF fields in CAM3.

The CHF in AMEP is parametrized as

$$CHF = k \cdot (T_s - T)^4 \operatorname{sign}(T_s - T)$$

where k is the proportionality constant and equals $9{\cdot}10^{-5} Wm^{-2}K^{-4}$, T is the atmospheric temperature and T_s is the surface temperature. k is kept

constant for all runs, so the parametrization restricts CHF to change only due to changes in the atmospheric temperature and in T_s.

The changes in CHF using the parametrized CHF with CAM3 data are calculated as

$$\Delta CHF = \Big[k \cdot (T_s - T)^4 \, \mathrm{sign}(T_s - T)\Big]_{\text{SST run}} - \Big[k \cdot (T_s - T)^4 \, \mathrm{sign}(T_s - T)\Big]_{\text{control}}$$

The result is shown in figure 7.7. The changes in the CHF field from CAM3 are seen as green, solid lines (same result as seen in figure 7.6). The changes in the parametrized CHF are seen as red, solid lines.

Although the CHF parametrization succeeds in capturing the main CHF field from CAM3, it fails to capture the CHF changes. This is especially true for the lowlat heating runs. This is because the atmospheric temperature warms more than T_s at mid- and low latitudes (see figure 7.5(a,b,c)), resulting in

$$(T_s - T)_{\substack{\text{lowlat} \\ \text{heating}}} < (T_s - T)_{\text{control}}$$

Consequently CHF is reduced in the lowlat heating runs compared to the control run. This is clearly seen in figures 7.7(a,b,c). It is worth noting that the same problem occurs using a linear parametrization.

The ±2K-Highlat runs exhibit greater similarity between the CHF field and the parametrization. The atmospheric temperature increases (decreases for the Minus 2K-Highlat run) less than T_s (see figure 7.5(d,e)), so the problem seen in the lowlat heating runs does not occur in these runs. The parametrized CHF is able to capture some of the larger changes, still the gradients in the parametrized CHF are smaller than in CAM3.

Also included in figure 7.7 is the same CHF parametrization as described above, but using different k values for each SST run. The k values were calculated from CHF fields in CAM3 and are listed in table 6.1. This method improves the results in the lowlat heating runs. This is especially true when

$$(T_s - T)_{\substack{\text{lowlat} \\ \text{heating}}} < (T_s - T)_{\text{control}}$$

for which the CHF parametrization failed when the same k value was used in all runs. However, using different k values for each run worsen the results in the ±2K-Highlat runs, in particular at low latitudes where

$$(T_s - T)_{\pm 2K \text{ Highlat}} \simeq (T_s - T)_{\text{control}}$$

This suggests that we may not be able to take k to be constant. Rather k should probably be dependent on temperature and/or humidity. Thus the changes in CHF in CAM3 are more involved than represented by the parametrization used in AMEP. This will be discussed further in section 9.1.1.

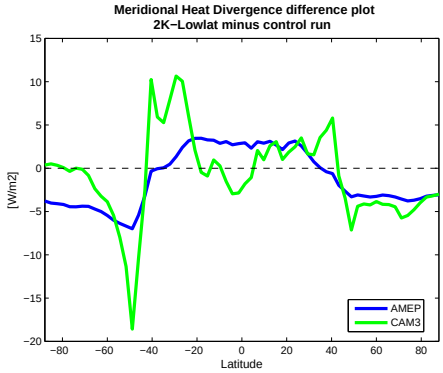

(a) 2K-Lowlat

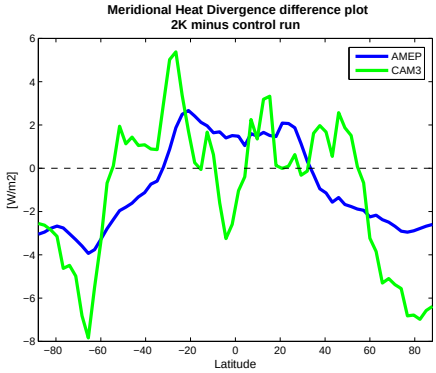

(b) 2K

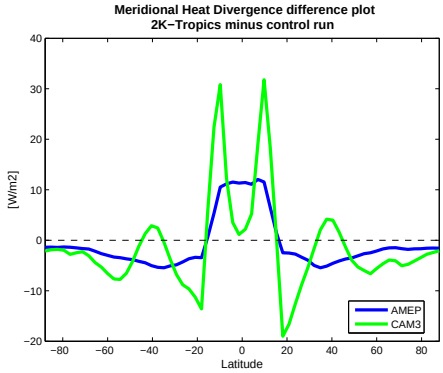

(c) 2K-Tropics

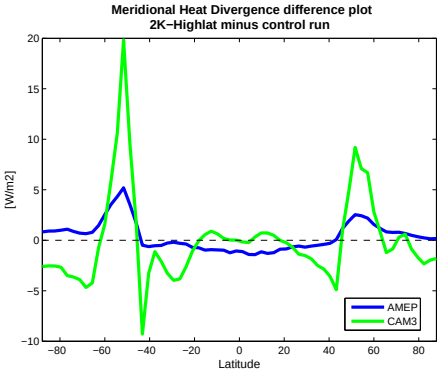

(d) 2K-Highlat

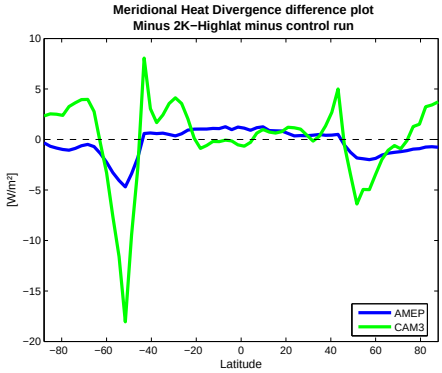

(e) Minus 2K-Highlat

Figure 7.8: The difference in the Meridional Heat Divergence, ζ, between the perturbed SST runs and the control run for CAM3 (green, solid line) and between the perturbed T_s runs and the control run for the AMEP model (blue, solid line).

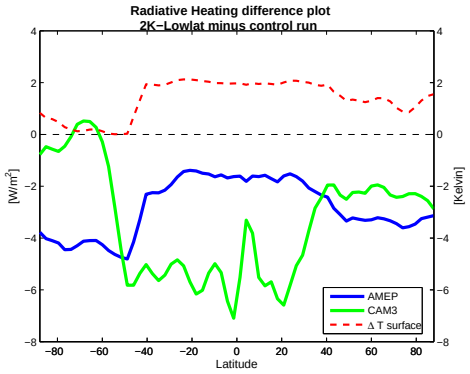

(a) 2K-Lowlat

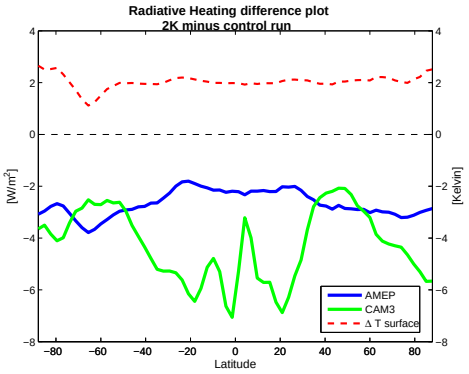

(b) 2K

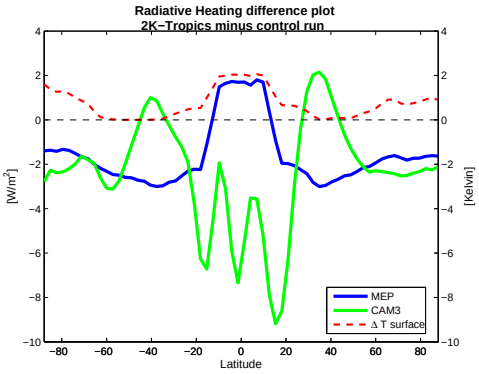

(c) 2K-Tropics

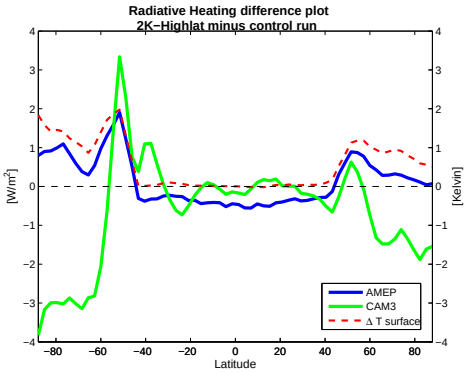

(d) 2K-Highlat

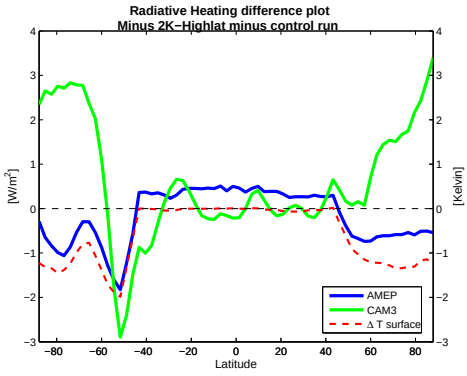

(e) Minus 2K-Highlat

Figure 7.9: The difference in the Atmospheric Net Radiative Heating, R_A, between the perturbed SST runs and the control run for CAM3 (green, solid line) and between the perturbed T_s runs and the control run for the AMEP model (blue, solid line). Also included is the difference in the zonal mean surface temperature field, T_s (red, dashed line), from CAM3. Note the two different y-axis.

7.2.3 The meridional heat divergence difference

The difference plots for the meridional heat divergence, ζ, are shown in figure 7.8. Most importantly, the shape of ζ is highly determined by the shape of the CHF. Consequently the changes seen in ζ correspond to the changes seen in CHF described in in section 7.2.2. This is true for both models. A detailed description of the changes seen for ζ is therefore not included. The magnitude of the changes on the other hand, differs from the results seen for CHF. This is because changes also occur in the radiation heating budgets for all the perturbed runs, in turn affecting ζ. The changes in the net radiative heating, R_A, for all the perturbed runs are seen in figure 7.9.

The changes in AMEP are highly dependent on the changes in T_s. This is expected. The insolation and the atmospheric absorptivity of solar radiation, A, stay the same for the different runs, resulting in no change in the absorbed solar radiation. This means that the changes in R_A are determined only by changes in the longwave radiation budget. The longwave radiation parameter, ϵ, also stays constant for all runs, making the changes in R_A determined only by changes in T_s and the atmospheric temperature (see figure 7.5). The changes can be written as

$$\Delta R_A \simeq \Delta\big(AF(1-R) - 2\epsilon\sigma(T+\delta T)^4 + \epsilon\sigma(T_s+\delta T_s)^4\big) \simeq -4\epsilon\sigma\big(2\delta T - \delta T_s\big) \tag{7.1}$$

$$\Delta R_A \propto \delta T_s - 2\delta T \tag{7.2}$$

This is not the case for the changes seen in R_A for CAM3, where R_A changes in response to altered solar absorption and altered absorption and emittance of longwave radiation. In CAM3, the lowlat heating runs experience increased radiative cooling in response to the altered SST. The only exceptions are at 40°N/S in the 2K-Tropics run for which the atmosphere warms. AMEP also shows atmospheric cooling in the lowlat heating runs, but less where there is surface heating, and radiative warming at low latitudes in the 2K-tropics run. This is quite the opposite from what is seen in CAM3, where the cooling increases as the SST warms.

In the ±2K-Highlat runs, the changes occur poleward of 45°N/S and are of opposite sign in the two models. In AMEP there is radiative heating (cooling in the Minus 2K-Highlat run) at high latitudes. In CAM3 there is radiative heating (cooling) at the same location as the changes seen in T_s and radiative cooling (warming) at high latitudes.

Nevertheless, the changes in CHF are one order of magnitude larger than the changes in R_A. So changes in ζ are still dominated by the changes in CHF, i.e.

$$\Delta\zeta \simeq \Delta\text{CHF} \tag{7.3}$$

ΔCHF differs in magnitude, but has the same tendencies in both models.

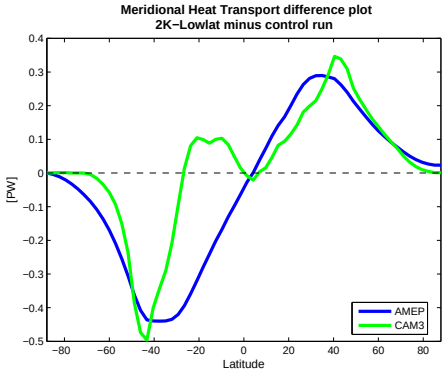

(a) 2K-Lowlat

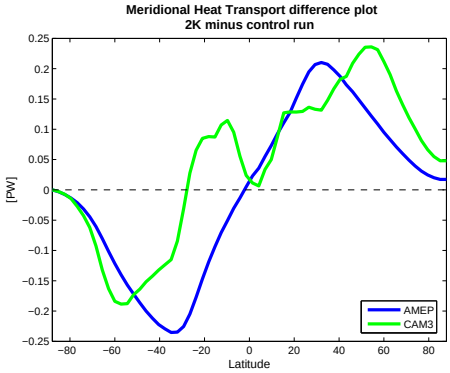

(b) 2K

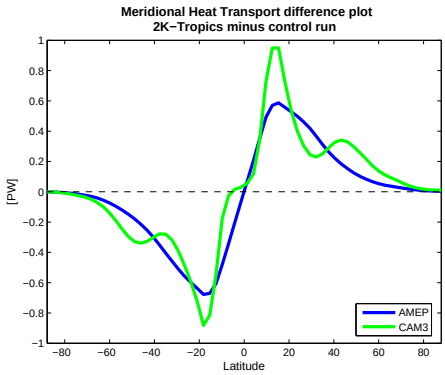

(c) 2K-Tropics

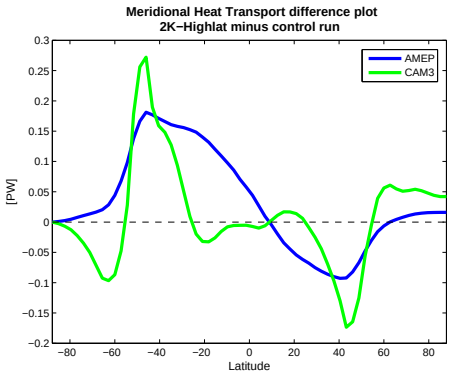

(d) 2K-Highlat

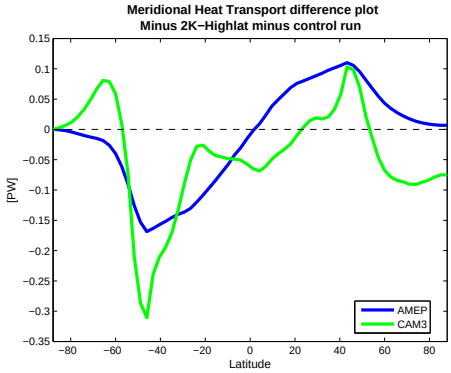

(e) Minus 2K-Highlat

Figure 7.10: Difference in the Meridional Heat Transport between the perturbed SST runs and the control run for CAM3 (green, solid line) and between the perturbed T_s runs and the control run for the AMEP model (blue, solid line).

7.2.4 The meridional heat transport difference

The difference plots for the meridional heat transport, F_ϕ, are seen in figure 7.10.

The 2K-Lowlat run (7.10(a))
F_ϕ increases in both models in response to the increased temperatures, but how F_ϕ changes differs. Consider the SH. In AMEP, the change is negative over the hemisphere, indicating an increase in the (southward) flux. However, with CAM3, the difference is positive near the equator and negative to the south. The result is that the maximum transport shifts southward, towards the pole. In the NH, AMEP behaves the same, while CAM3 has a more localized maximum. This also causes a poleward shift, albeit a less pronounced one than in the SH. Note too that the maximum changes are slightly smaller in AMEP than in CAM3.

The 2K run(7.10(b))
The differences in the 2K runs resemble those in the 2K-Lowlat runs, but with smaller magnitudes. The sharp maxima in the changes in CAM3 are located poleward of the maxima in the 2K-Lowlat run and peak at 57°S and 54°N. A reduction in F_ϕ at low latitudes is again seen in the SH. The maximal transports are shifted poleward in both hemispheres. In AMEP the peaks are slightly equatorward compared to the 2K-Lowlat run. The transport increases, but no shift occurs. The result is similar to the 2K-Lowlat run. The increase in F_ϕ is greater in AMEP than in CAM3 in the SH.

The 2K-Tropics run (7.10(c))
For the 2K-Tropics run both models show increased transport in the tropics. The changes seen are the greatest of all the runs. The results from the two models are similar, but the increase is greater in CAM3 than in AMEP. Although CAM3 exhibits a greater increase in F_ϕ in the tropics, no equatorward shift of the maximal transport occurs. The reason for this is the second peak at mid-latitudes in each hemisphere, which makes the transport also increase at mid-latitudes. The equatorward shift is clearly seen if only eddy transport is considered (not shown). The increase is not as great in AMEP as in CAM3, but the maxima occur at the same latitudes as in CAM3. An equatorward shift in the maximal transport is seen in AMEP. This is the only run where a shift of the maximal transport is seen in AMEP.

The ±2K-Highlat runs (7.10(d))
The CAM3 result exhibits small changes in the tropics. F_ϕ is reduced at mid-latitudes (increased for the Minus 2K-Highlat run) and increased (decreased) at high latitudes. For the Minus 2K-Highlat run there is also a small decrease in F_ϕ in the tropics. Sharp minima (maxima) are located at mid-latitudes in CAM3, resulting in a equatorward (poleward) shift of the maximal transport in both hemispheres. AMEP exhibits a reduction (increase) in F_ϕ for both

hemispheres and no shifts in the transport occur.

The changes in F_ϕ have the same magnitude and exhibit similar tendencies in both models. The changes peak at the same latitude for the two models in the 2K-Tropics runs and the ±2K-Highlat runs. In the 2K-Lowlat runs and the 2K runs, the peaks in AMEP are equatorward of the peaks in CAM3.

Thus an important difference between AMEP and CAM3 is the *shape* of the changes in F_ϕ. CAM3 exhibits sharp maxima at mid-latitudes for all runs, except the 2K-Tropics run where the sharp maxima are located at low latitudes. The changes in AMEP are smoother, occur over larger areas and exhibit a shape similar to the shape of F_ϕ itself. The sharp, localized changes in F_ϕ result in the shifts of the maximal transport in CAM3. In AMEP the transport only increase (i.e. the 2K-Lowlat, 2K and Minus 2K-Highlat runs) or decrease (i.e. the 2K-Highlat run). The only exception is the 2K-Tropics run for which an equatorward shift of the maximal transport is seen in AMEP.

Although AMEP shows some of the same tendencies in the changes in the atmospheric temperature, CHF, ζ and F_ϕ as seen in CAM3, AMEP is not generally able to capture the shifts in the maximal meridional heat transport. The reasons for this will be discussed in chapter 9.

Chapter 8

Summary

In order to arrive at a suitable model, several models have been presented. Before discussing the results found in the present study, a summary of the work carried out in this thesis is suitable.

Graff and LaCasce (2012) used an AGCM (CAM3.0) to study changes in storm tracks due to altered SST. Brayshaw et al. (2008) did a similar study using aquaplanet simulations to investigate the tropospheric response to mid-latitude SST anomalies. The results of the studies were consistent, showing that SST forcing induced changes in both the strength and position of the subtropical and the eddy-driven jet. The changes in the eddy-driven jet corresponded with changes in the storm tracks.

The purpose of the present study was to see if an ebm, exploiting the MEP principle, was able to capture these changes. Graff and LaCasce (2012) investigated shifts in jets, storm tracks and meridional heat fluxes. For the meridional heat fluxes, band passed filtered fields were used, but consistent changes were seen in the mean fields as well (see figure 2.2 in section 2.1). Tropospheric mixing and transport in middle and high latitudes are driven mainly by synoptic eddy activity. Thus, the shift in storm tracks seen in their study should correspond to a shift in the maximal meridional heat transport in the atmosphere. Bandpass-filtered fields could not be used in the model intercomparison in this thesis, hence changes in the maximal mean transport were investigated instead.

Paltridge (1975, 1978) proposed the first MEP model, which was a coupled atmosphere-ocean model. Ebms constrained by MEP have later been used to study climate sensitivity (Grassl, 1981; Pujol and Llebot, 2000b; Lorenz et al., 2001; Paltridge et al., 2007) and have showed inconclusive results.

An examination of Paltridge's MEP model proved it unsuitable for the present study. The model is an air-sea model containing both atmospheric and oceanic heat transport, while the aim of the present study was to examine changes in the atmospheric transport only. Consequently we needed to

construct an Atmospheric MEP model (AMEP) to be able to compare our results with results from CAM3. In order to make an AMEP model it was necessary to build a hierarchy of box models.

First two-box models were developed and investigated. We started out with a simple model, making it more complex, closing in on the AMEP model. Horizontal two-boxes models were made, starting out with the simplest case, *the Blackbody Assumption*. Then we made the two-box model more realistic by adding atmospheric emissivity and by fixing the surface temperature, i.e. *Grey Atmosphere, Black Surface*. In the final version of the horizontal two-box model, only the atmospheric layer was considered, i.e. *An two-box atmospheric MEP model*.

Only radiative processes were considered in the horizontal two-box models. In order to investigate fluxes of sensible and latent heat, a vertical box model was made. The results from the vertical MEP model was used to parametrize the convective heat flux (CHF). The parametrization was confirmed using CHF data from CAM3 and the proportionality constant, k, determined.

Going from 2 to 64 boxes, a multi-box horizontal atmospheric MEP model, namely *the AMEP model*, was constructed. This model is an ebm using the MEP state as a constraint. The convective heat fluxes were parametrized using the results found in the vertical two-box model, and SST forcing was made possible. Shifts in the maximal heat transport were then investigated.

The results from AMEP were compared with results from CAM3. There was a good correspondence between the changes seen in the atmospheric temperatures in both models. However, CAM3 exhibits broader changes in the lowlat heating runs, indicating that more heat is gained at higher latitudes in CAM3.

The changes in meridional heat transport differ considerably between the two models. AMEP has changes that mirror the total transport curve, while CAM3 has more localized changes. Thus the total AMEP transport increases or decreases, while the maximal transport in CAM3 shifts as well. The only exception was in the 2K-Tropics run, where an equatorward shift in the maximal transport was seen in AMEP. Nevertheless, AMEP generally fails to capture the shifts in the maximal heat transport seen in CAM3.

The main reason for this is the changes in CHF, which differ considerably between the two models. The meridional heat divergence, ζ, is the sum of CHF and the net radiative heating, R_A. $R_A \simeq -100 W m^{-2}$ and shows little latitudinal variance. The changes in R_A, due to altered SST, are also fairly small. Consequently;

$$\Delta\zeta \simeq \Delta\, CHF$$

This shows that the changes in the meridional heat divergence are mainly determined by changes in CHF. CHF exhibits abrupt changes and large values in the altered SST runs. The abrupt changes are often located at the same latitudes as the SST forcing stops. The changes in CHF are responsible for the shifts in the maximal heat transport. Since AMEP fails to capture the CHF changes, the shifts in the transport are not captured either.

Chapter 9

Discussion and Conclusions

Results show that CAM3 exhibits a shift in the meridional heat transport due to altered SST, while AMEP does not. The reasons for this difference are discussed below (section 9.1). A discussion of the application of the MEP principle is also provided (section 9.2), before the conclusions (section 9.3) are given.

9.1 Discussion of results

9.1.1 CHF

The parametrized CHF used in AMEP failed to capture the changes in CHF seen in CAM3, indicating that changes in CHF depend on more than only atmospheric and surface temperature changes.

The moisture content in the atmosphere can change in response to altered temperatures. A warmer atmosphere can contain more moisture and a warmer ocean (or a wet surface) can evaporate more water. The Clausius-Clapeyron equation shows the relation between saturated vapor pressure and temperature in the atmosphere and can be written as (Wallace and Hobbs, 2006)

$$\frac{\mathrm{d}e_s}{\mathrm{d}T} = \frac{L}{T \cdot (\alpha_2(T) - \alpha_1(T))} \tag{9.1}$$

where e_s is the saturated water vapor pressure, L is the latent heat of vaporization and equals $2.25{\cdot}10^6 Jkg^{-1}$. α_1 and α_2 are the specific volumes of liquid water and water vapor at temperature T. Equation 9.1 shows that the saturation vapor pressure changes approximately exponentially with temperature. Consequently, small changes in temperature can cause big changes in the saturation pressure. The increased saturation pressure makes a larger water vapor content in the atmosphere possible.

Figure 9.1 shows changes in specific humidity, q, for the perturbed SST runs in CAM3. Also included are changes in CHF for the corresponding runs.

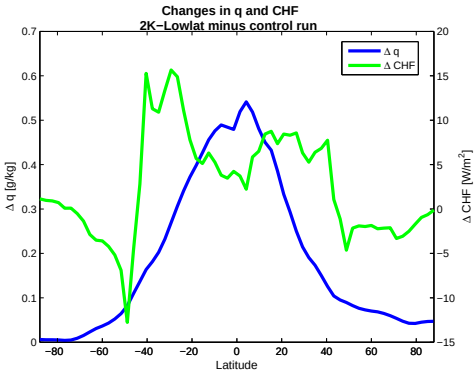

(a) 2K-Lowlat

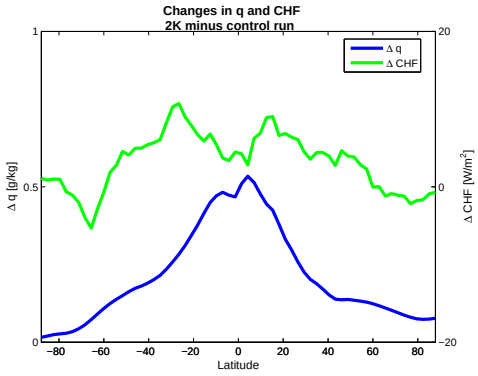

(b) 2K

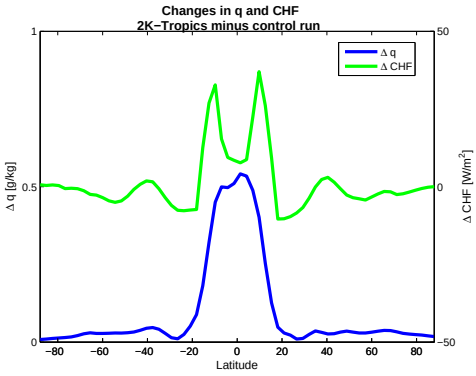

(c) 2K-Tropics

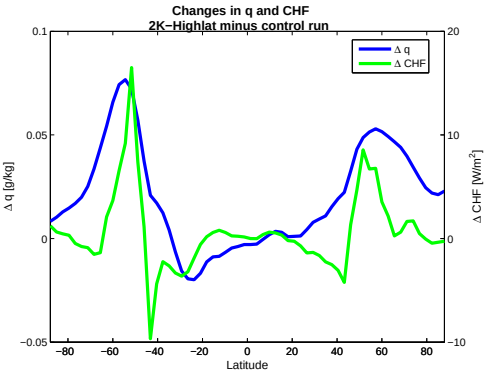

(d) 2K-Highlat

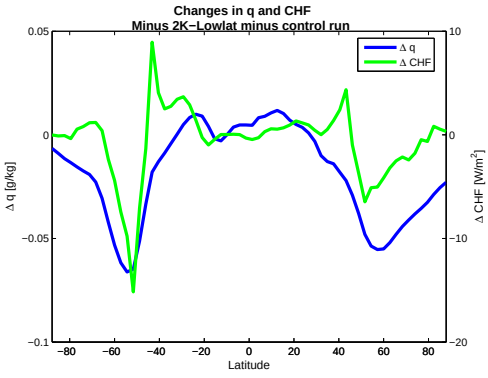

(e) Minus 2K-Highlat

Figure 9.1: The changes in the specific humidity, q, (blue, solid line) and the convective heat flux, CHF, (green, solid line) between the perturbed SST runs and the control run in CAM3.

The changes in CHF are the same as seen in figure 7.6 in section 7.2.2. The changes in specific humidity give a measurement of changes in the moisture content in the atmosphere. The moisture content in CAM3 is indeed changing in the heated areas (cooled for the Minus 2K-Highlat run). For the 2K-Tropics runs and the ±2K-Highlat runs the changes in the specific humidity correlate well with changes in CHF. The correlation is not as good in the 2K-Lowlat and 2K runs.

As seen in equation 9.1; a warmer atmosphere can contain more moisture before it is saturated. The increased moisture content results in increased latent heat release, which dominates CHF. Moisture is not included in AMEP and the results in figure 9.1 indicate that this can be one of the reasons why AMEP fails to capture the CHF changes.

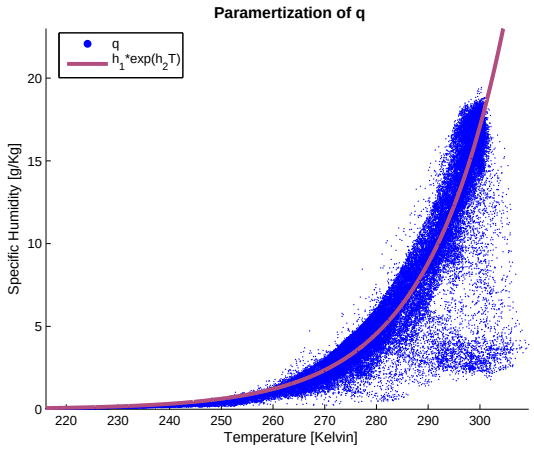

Figure 9.2: Scatter plot of atmospheric temperature and specific humidity using reanalyse data from ECMWF (blue dots). The data used are the vertically-averaged data from the five lowest levels of the atmosphere. All data are from the 1^{st} of April 2008. Also included is an exponential fit of the reanalysis data (red, solid line).

One way to include moisture in AMEP is to parametrize the specific humidity in the atmosphere in terms of temperature. To find a relationship between the temperature and specific humidity in the atmosphere, ECMWF operational reanalysis data were obtained from the ECMWF data server. ECMWF reanalysis data are model data assimilated with observational data in a 4D assimilation process, in order to statistically best represent the current state of the atmosphere. A global 1x1 degree grid was selected for model temperatures and specific humidity values.

Figure 9.2 shows a scatter plot of the atmospheric temperature and specific humidity. Vertically-averaged reanalysis data from the lowest levels of the

atmosphere were used for all global points using daily averages of April 1st 2008. Using global values should ensure that all conditions are covered. To be implemented it is, however, recommended to use more data, to see if there are annual or zonal differences, and possibly look at data for several more atmospheric layers.

The fitted curve is an exponential fit to the reanalysis data. The relationship between the two observed properties is

$$q = h_1 \cdot e^{h_2 T} \tag{9.2}$$

where q is the specific humidity, T is the atmospheric temperature, $h_1 = 4.3 \cdot 10^{-8} g k g^{-1}$ and $h_2 = 6.6 \cdot 10^{-2} K^{-1}$. The moisture dependence on temperature could be included in the parametrized CHF in AMEP by implementing the findings in equation 9.2 into the proportionality constant k. Instead of using a constant k for all latitudes, k could be a function of the atmospheric temperature. This way, k could include the specific humidity in the atmospheric layer. This could be one way of accounting for moisture effects in the atmosphere in AMEP.

Another way of including moisture changes in AMEP is to use new parameters for each SST run, and in this way capture the changes in CHF. The atmospheric reflectivity, absorptivity, emissivity and the proportionality constant k differ in each SST run and could be recalculated in CAM3. These new parameters could then be used in AMEP to reproduce the CHF changes seen in CAM3. This defeats the intention of applying a simplified model in the first place, as it forces AMEP to act as CAM3. If AMEP was able to provide the same results as CAM3 using the SST changing parameters, the AMEP results would be true tautologically.

In addition, clouds could be added to the model. The clouds are not independent variables in AMEP. The mean cloud cover fraction is included through the parameters used, i.e. the atmospheric reflectivity, absorptivity and emissivity of radiation. Since the parameters stay constant between boxes and in various runs, the cloud cover fraction stays fixed as well. The cloud cover in CAM3 varies both zonally and between the various runs (see figure 9.3). The zonal changes in the cloud cover within each run are greater than the cloud cover changes between the runs, but neither of the changes are captured in AMEP. This could also be important for the differences seen in the results between the two models. However, the changes in the cloud cover are not consistent with the forcing in the perturbed SST runs and the magnitude of change is somewhat small, indicating that the clouds may not be that important. The similarities between $\Delta\, CHF$ and $\Delta\, \zeta$ suggest that the changes in CHF are more important.

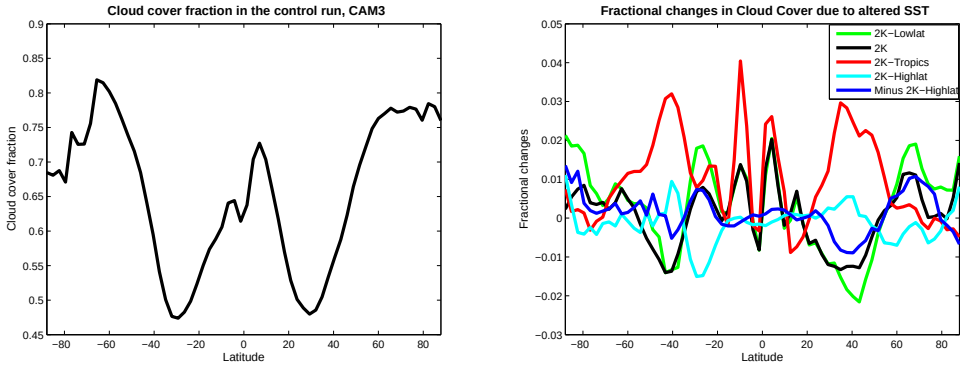

(a) (b)

Figure 9.3: (a) Annually- and zonally averaged cloud cover fraction in the control run in CAM3. (b) Fractional changes in annually- and zonally-cloud cover between the perturbed SST runs and the control run in CAM3.

9.1.2 Dynamics

Another important difference between the two models is the dynamics. AMEP is an ebm and does not resolve any dynamics. CAM3, on the other hand, take atmospheric dynamics into account.

It is fair to ask whether the use of a simplified ebm without any dynamics is suited to investigate shift in storm tracks, which is a highly dynamic feature. The intention was that the MEP state constraint used could account for some of the lacking dynamics and that AMEP would be able to capture the results of the dynamic features, as proclaimed by Dyke and Kleidon (2010) and Dewar (2009). For further discussion of this *claim*, see section 9.2.

The dynamics turned out to make a difference. Consider for example the 2K-Lowlat runs, for which there is a positive SST (CAM3) / T_s (AMEP) forcing at low and middle latitudes. The atmosphere gains extra heat from the surface due to increased surface emission of radiation and increased CHF. The only way AMEP can redistribute the excess heat is to move it poleward. Because no dynamics are included in AMEP, no specific regions are preferred for the additional heat transport.

In CAM3, the extra heat gained in the atmosphere alters the atmospheric circulation in several ways. The heating affects the atmospheric baroclinicity, which has ramifications for the jet and the storm tracks. Equally important is that strong baroclinic zones are preferred regions for cyclone development; hence the atmospheric heat transport is larger in these regions in CAM3. This latitudinal dependence for the heat transport in CAM3 is different from

AMEP, where no preferred region for the heat transport exists.

In the 2K-Lowlat run, large changes in both the mean and the eddy circulation occur in CAM3. The jets are intensified and shifted poleward. The same result is seen for the storm tracks. In addition, changes in the meridional overturning circulation are seen, e.g. the expansion of the Hadley Cell (see section 2.1 for further details). The changes seen in the CAM3 results are partly a consequence of all the circulation changes described above. None of these circulation changes occur in AMEP, and no shift in the transport is seen.

The impact of dynamics is also seen in the temperature difference plot (figure 7.5 in chapter 7) for the two models. The changes in the atmospheric temperature in AMEP mirror the gradients in the forced T_s. The temperature changes seen in CAM3 are much broader, indicating more efficient atmospheric mixing. The atmospheric mixing flattens the transitions from the heated regions to the unaltered regions, which is not the case in AMEP.

It may be possible to include some dynamics in AMEP. One method could be to parametrize ζ in terms of the meridional temperature gradient, dT/dy. By doing this, baroclinic instability could be crudely included in AMEP. The parametrization could guarantee that strong mixing occurs at the same latitude as the temperature gradient. This method could account for some of the latitudinal dependence seen in CAM3, but lacking in AMEP.

9.2 Discussion of the MEP principle

For an isolated system the entropy is maximized when the system is in thermodynamic equilibrium. For a system out of thermodynamic equilibrium there is no proof that such a state exists. However, the MEP principle proclaims that a steady state system out of thermodynamic equilibrium will be in a state of maximum entropy production. There is little theory backing the MEP principle. Other quantities which may be maximized instead have been suggested, such as the APE (Lorenz, 1960).

There are different views on why the MEP principle works and how it can be used. Although the MEP principle itself is not the main subject in this thesis, I think it deserves some closing remarks. The problem of interest is the same; how to predict macroscopic behavior of non-equilibrium physical systems (e.g. turbulent heat transport in the atmosphere), but the purpose of the MEP principle differ.

9.2.1 The MEP principle as a physical principle

The MEP principle can be regarded as a physical principle, which contains physical assumptions beyond the more familiar laws of physics (e.g. conservation of mass, conservation of energy, etc.). From this point of view the

MEP principle is regarded as a fundamental adjustability of non-equilibrium systems, e.g. the Earth will adjust it self as to maximize the entropy production. Kleidon (2004, 2009) and Lorenz et al. (2001) apply the MEP principle in this context. A 2-box model is used to find estimates of the effective conductivity of the linearized heat transport (see section 3.2.7). Kleidon (2004, 2009) studied the total heat transport in the climate system on Earth, while Lorenz et al. (2001) studied the atmospheric heat transport on Earth and other planets. The effective conductivity was determined to be the one corresponding to the MEP state for the system under consideration.

One question comes to mind regarding these studies, and also regarding Paltridge's MEP model, namely the lack of some essential details, like the rotation rate of the Earth. A substantial part of the atmospheric heat transport is due to synoptic eddies which would not exist in the absence of the Coriolis force. Would the heat transport in the atmosphere stay the same if the world spun twice as fast? These properties are buried in the effective conductivity parameter used in the linearization of the heat flux. However, no information about it is given in the models used to calculate it in the first place.

Walker and Schneider (2006) investigated changes in the strength and meridional extent of the Hadley circulation due to altered rotation rate of the Earth using an idealized GCM. Their findings showed that the Hadley circulation became wider and stronger as the rotation rate decreased.

Dyke and Kleidon (2010) argue that Paltridge (1975, 1978), Kleidon (2004, 2009) and Lorenz et al. (2001) still managed to find realistic predictions using the MEP principle. This tells us that such *details* (s.a. the Coriolis force) are irrelevant for the purpose of the models and demonstrate that complex systems, like planetary atmospheres, may not be required to get accurate predictions for *some* properties. For instance; if the world spun twice as fast, the synoptic eddies would probably differ, but the efficiency of the transport may stay the same, since the eddies also depend on the baroclinicity of the atmosphere. E.g. more efficient eddies would decrease the temperature gradients and in this way decrease the baroclinicity, making the eddies less efficient. Walker and Schneider (2006) findings suggest that Dyke and Kleidon (2010) argument may be too simple.

9.2.2 The MEP principle as a Messenger of Essential Physics

The MEP principle can be regarded as a passive algorithm that translate physical information into predictions without introducing any additional physics or assumptions (Dewar, 2009). The algorithm (like MaxEnt (Jaynes, 1957a,b) used in information theory) produces the least biased estimate possible on the given information. In this context the MEP principle can only

predict phenomena that are already predictable. The physical constraints used are the law of physics and the predictions are found by using for instance the equations of motion, from which we could predict system behavior without any reference to the MEP principle. So why should we care?

Instead of simulating all microscopic physics in detail, only to discover that most of the microscopic behavior is irrelevant to the macroscopic behavior, the MEP principle seeks to identify a set of *essential physical assumptions* that provide the same result. The identification of the *essential physics* may only be achieved through trial and error (Dewar, 2009). The MEP state should be chosen because it reflects the physical assumptions, not because the system in itself is driven to the MEP state physically.

Every student in meteorology has a comprehension of the frequently used concept of an *air parcel*. We use air parcels because we do not bother to calculate every single molecule movement in the air. Instead, we choose an *air parcel* and define the macroscopic quantities, like temperature and pressure for that parcel, regardless of its microscopic properties. The same way of thinking describes this view of MEP. The microscopic properties (e.g. every single cyclone) are not important when we consider climate predictions. Instead we can define certain physical assumptions that give us the predictions directly, without the use of enormous calculation schemes which are needed in GCMs in order to calculate the same predictions.

9.3 Conclusions

The main conclusions derived from this thesis' investigations are provided in bullet points below.

- A vertical MEP model was used to investigate fluxes and sensible and latent heat. The result showed a ΔT^4 dependence in CHF. The result was compared to CHF data from CAM3, for which a similar dependence was found. This was especially true for fluxes of latent heat. The result indicates that the MEP assumption may be suitable for studying vertical convection.

- The Atmospheric MEP model, AMEP, managed to capture the main tendencies in the atmospheric temperature and the meridional heat transport changes seen in CAM3. However, AMEP failed to capture the shifts in the maximal heat transport due to the T_s forcing. The only exception was in the 2K-Tropics run where an equatorward shift of the maximal transport was seen in AMEP. In this run the shift in the maximal heat transport was toward the region where the forcing occurred, indicating an increased transport out of the heated region.

The large and abrupt changes in CHF in CAM3, were not captured by AMEP. This is the reason why AMEP failed to capture the transport shifts in CAM3. AMEP is too simple to capture non-trivial changes in the atmospheric circulation because it has neither a Hadley cell nor baroclinic instability. To capture the circulation changes, the AMEP needs dynamics and possible a moisture parametrization. Equally important is the strong latitude dependence in the heat transport in CAM3 needs to be present in AMEP. Dynamics matter and these are not captured in AMEP. Consequently, AMEP is not suited for studying the shifts in the meridional heat transport.

- While the MEP principle obviously has its limitations, it does offer computational efficiency. However, the findings in this thesis may suggest that the dynamics of the eddies in the atmosphere and the strong relation between the eddies and the meridional heat transport, may be too important to be regarded as microscopic properties of the climate system.

- An interesting result seen in this thesis, which is not directly related to MEP, is the relation

$$\Delta CHF \simeq \Delta\zeta$$

seen in CAM3. CAM3 exhibits large changes in CHF as a response to altered SSTs. It is the changes in the meridional heat divergence, ζ, which cause the shift in the maximal meridional heat transport. Due to fairly small changes in the net radiative heating, the changes in ζ are determined mainly by changes in CHF. This finding indicates that the changes in CHF can be more important than previously presumed for the shift in the storm tracks in CAM3. This finding provides grounds for further research.

Bibliography

Brayshaw, David James; Hoskins, Brian J. and Blackburn, Michael (2008) *The Storm-Track Response to Idealized SST Perturbations in an Aquaplanet GCM*. Journal of the Atmospheric Sciences, Vol. 65(9): p. 2842–2860. URL http://centaur.reading.ac.uk/1303/.

Busse, F. H. (1978) *The optimum theory of turbulence*. Archive of Applied Mechanics, Vol. 18: p. 77–121.

Charney, J. G. (1947) *The dynamics of long waves in a baroclinic westerly current*. J. Meteorol., Vol. 4: p. 135–163. URL http://ci.nii.ac.jp/naid/10019920229/en/.

Clausius, R. (1865) *Ueber verschiedene für die Anwendung bequeme Formen der Hauptgleichungen der mechanischen Wärmetheorie*. Annalen der Physik, Vol. 201(7): p. 353–400. ISSN 1521-3889. URL http://dx.doi.org/10.1002/andp.18652010702.

Collins, William D; Rasch, Philip J; Boville, Byron A; Hack, James J; Mccaa, James R; Williamson, David L; Kiehl, Jeffrey T and Lin, Shian-jiann (2004) *Description of the NCAR Community Atmosphere Model (CAM 3 . 0)*. Science, Vol. NCAR/TN-48(June): p. 226. URL http://www.ccsm.ucar.edu/models/atm-cam/docs/description/desc%ription.pdf.

Dewar, R. (2003) *Information theory explanation of the fluctuation theorem, maximum entropy production and self-organized criticality in non-equilibrium stationary states*. Journal of Physics A Mathematical General, Vol. 36: p. 631–641.

Dewar, Roderick (2005) *4 Maximum Entropy Production and Non-equilibrium Statistical Mechanics*. In Axel Kleidon and Ralph Lorenz (editors), *N*on-equilibrium Thermodynamics and the Production of Entropy, Vol. 2 of *U*nderstanding Complex Systems, p. 41–55 (Springer Berlin / Heidelberg). ISBN 978-3-540-22495-2. URL {http://dx.doi.org/10.1007/11672906_4}.

Dewar, Roderick C (2009) *Maximum Entropy Production as an Inference Algorithm that Translates Physical Assumptions into Macroscopic Predictions: Don't Shoot the Messenger*. Entropy, Vol. 11(4): p. 931–944. URL http://www.mdpi.com/1099-4300/11/4/931/.

Donohoe, A. and Battisti, D. S. (2010) *Atmospheric and Surface Contributions to Planetary Albedo and their Relationship to the Total Meridional Energy Transport*. AGU Fall Meeting Abstracts, p. J4.

Dyke, James and Kleidon, Axel (2010) *T*he Maximum Entropy Production Principle: Its Theoretical Foundations and Applications to the Earth System. Entropy, Vol. 12(3): p. 613–630. ISSN 1099-4300. URL http://www.mdpi.com/1099-4300/12/3/613.

Eady, E. T. (1949) *Long Waves and Cyclone Waves*. Tellus, Vol. 1(3): p. 33–52. ISSN 2153-3490. URL http://dx.doi.org/10.1111/j.2153-3490.1949.tb01265.x.

Feigenbaum, M. J. (1983) *Universal behavior in nonlinear systems*. Physica D Nonlinear Phenomena, Vol. 7: p. 16–39.

Feigenbaum, Mitchell J. (1978) *Q*uantitative universality for a class of nonlinear transformations. Journal of Statistical Physics, Vol. 19: p. 25–52. ISSN 0022-4715. URL http://dx.doi.org/10.1007/BF01020332, 10.1007/BF01020332.

Graff, Lise Seland and LaCasce, J. H. (2012) *Changes in the Extratropical Storm Tracks in Response to Changes in SST in an AGCM.*. Journal of Climate, Vol. 25(6): p. 1854–1870. ISSN 1521-3889. URL ttp://dx.doi.org/10.1175/JCLI-D-11-00174.1.

Grassl, Hartmut (1981) *The climate at maximum entropy production by Meridional atmospheric and oceanic heat fluxes*. Quarterly Journal of the Royal Meteorological Society, Vol. 107(451): p. 153–166. ISSN 1477-870X. URL http://dx.doi.org/10.1002/qj.49710745110.

Hack, J. J.; Caron, J. M.; Danabasoglu, G.; Oleson, K. W.; Bitz, C. and Truesdale, J. E. (2006) *CCSM CAM3 Climate Simulation Sensitivity to Changes in Horizontal Resolution*. Journal of Climate, Vol. 19: p. 2267.

Hartmann, Dennis L. (1994) *Global Physical Climatology* (Academic Press).

IPCC (2007) *Summary for Policymakers*. In *Climate Change 2007: The Physical Science Basis. Contribution of Working Group I to the Fourth Assessment Report of the Intergovernmental Panel on Climate Change [Solomon, S., D. Qin, M. Manning, Z. Chen, M. Marquis, K.B. Averyt, M. Tignor and H.L. Miller (eds.)]* (Cambridge University Press, Cambridge, United Kingdom and New York, NY, USA).

Jaynes, E. T. (1957a) *Information Theory and Statistical Mechanics*. Phys. Rev., Vol. 106: p. 620–630. URL http://link.aps.org/doi/10.1103/PhysRev.106.620.

Jaynes, E. T. (1957b) *Information Theory and Statistical Mechanics. II*. Phys. Rev., Vol. 108: p. 171–190. URL http://link.aps.org/doi/10.1103/PhysRev.108.171.

Jaynes, E T (1980) *The Minimum Entropy Production Principle*. Annual Review of Physical Chemistry, Vol. 31(1): p. 579–601. URL http://www.annualreviews.org/doi/abs/10.1146/annurev.pc.31.10%0180.003051.

Kleidon, Axel (2004) *Beyond Gaia: Thermodynamics of Life and Earth System Functioning*. Climatic Change, Vol. 66: p. 271–319. ISSN 0165-0009. URL http://dx.doi.org/10.1023/B:CLIM.0000044616.34867.ec, 10.1023/B:CLIM.0000044616.34867.ec.

Kleidon, Axel (2009) *Nonequilibrium thermodynamics and maximum entropy production in the Earth system*. Naturwissenschaften, Vol. 96: p. 653–677. ISSN 0028-1042. URL http://dx.doi.org/10.1007/s00114-009-0509-x, 10.1007/s00114-009-0509-x.

Kushner, P. J.; Held, I. M. and Delworth, T. L. (2001) *Southern Hemisphere Atmospheric Circulation Response to Global Warming.*. Journal of Climate, Vol. 14: p. 2238–2249.

Levitus, Sydney; Antonov, John I.; Boyer, Timothy P. and Stephens, Cathy (2000) *Warming of the World Ocean*. Science, Vol. 287(5461): p. 2225–2229. URL http://www.sciencemag.org/content/287/5461/2225.abstract.

Lin, Charles A. (1982) *An extremal principle for a one-dimensional climate model*. Geophysical Research Letters, Vol. 9(6): p. 716–718. ISSN 0094-8276. URL http://dx.doi.org/10.1029/GL009i006p00716.

Lorenz, D. J. and DeWeaver, E. T. (2007) *Tropopause height and zonal wind response to global warming in the IPCC scenario integrations*. Journal of Geophysical Research (Atmospheres), Vol. 112(D11): p. 10 119.

Lorenz, E. N. (1960) *Generation of available potential energy and the intensity of the general circulation*. In R. C. Pfeffer (editor), *D*ynamics of Climate, p. 86–92 (Pergamon Press, Oxford, UK).

Lorenz, E. N. (1963) *Deterministic Nonperiodic Flow.*. Journal of Atmospheric Sciences, Vol. 20: p. 130–148.

Lorenz, Edward N. (1955) *Available Potential Energy and the Maintenance of the General Circulation*. Tellus, Vol. 7(2): p. 157–167. ISSN 2153-3490. URL http://dx.doi.org/10.1111/j.2153-3490.1955.tb01148.x.

Lorenz, Ralph D.; Lunine, Jonathan I.; Withers, Paul G and McKay, Christopher P. (2001) *Titan, Mars and Earth : Entropy production by latitudinal*

heat transport. Geophysical Research Letter, Vol. 28(3): p. 415– 418. URL http://dx.doi.org/10.1029/2000GL012336.

Lu, J.; Chen, G. and Frierson, D. M. W. (2010) *The Position of the Mid-latitude Storm Track and Eddy-Driven Westerlies in Aquaplanet AGCMs*. Journal of Atmospheric Sciences., Vol. 67(12): p. 135–163. URL http://dx.doi.org/10.1175/2010JAS3477.1.

Lu, J.; Vecchi, G. A. and Reichler, T. (2007) *Expansion of the Hadley cell under global warming*. Geophysical Research Letters, Vol. 34: p. 6805.

Martyushev, Leonid M. (2010) *The maximum entropy production principle: two basic questions.*. Philosophical transactions of the Royal Society of London. Series B, Biological sciences, Vol. 365: p. 1333–1334. ISSN 1471-2970.

Martyushev, L.M. and Seleznev, V.D. (2006) *Maximum entropy production principle in physics, chemistry and biology*. Physics Reports, Vol. 426(1): p. 1 – 45. ISSN 0370-1573. URL http://www.sciencedirect.com/science/article/pii/S03701573050%04813.

Meehl, G. A.; Stocker, T F; Collins, W D; Friedlingstein, P; Gaye, A T; Gregory, J M; Kitoh, A; Knutti, R; Murphy, J M; Noda, A and et al. (2007) *Global Climate Projections. In: Climate Change 2007: The Physical Science Basis. Contribution of Working Group I* (Cambridge University Press). URL http://www.ipcc.ch/publications_and_data/ar4/wg1/en/ch10.html%.

O'Brien, D. M. and Stephens, G. L. (1995) *Entropy and climate. II: Simple models*. Quarterly Journal of the Royal Meteorological Society, Vol. 121(527): p. 1773–1796. ISSN 1477-870X. URL http://dx.doi.org/10.1002/qj.49712152712.

Ozawa, Hisashi; Ohmura, Atsumu; Lorenz, Ralph D and Pujol, Toni. (2003) *The second law of thermodynamics and the global climate system: A review of the maximum entropy production principle*. Rev. Geophys., Vol. 41(4): p. 1018–. ISSN 8755-1209. URL http://dx.doi.org/10.1029/2002RG000113.

Ozawa, Hisashi; Shimokawa, Shinya and Sakuma, Hirofumi (2001) *Thermodynamics of fluid turbulence: A unified approach to the maximum transport properties*. Phys. Rev. E, Vol. 64: p. 026 303. URL http://link.aps.org/doi/10.1103/PhysRevE.64.026303.

Paltridge, G. W. (1974) *Global Cloud Cover and Earth Surface Temperature.*. Journal of Atmospheric Sciences, Vol. 31: p. 1571–1576.

Paltridge, G. W. (1975) *Global dynamics and climate - a system of minimum entropy exchange*. Quarterly Journal of the Royal Meteorological Society,

Vol. 101(429): p. 475–484. ISSN 1477-870X. URL http://dx.doi.org/10.1002/qj.49710142906.

Paltridge, G. W. (1978) *The steady-state format of global climate*. Quarterly Journal of the Royal Meteorological Society, Vol. 104(442): p. 927–945. ISSN 1477-870X. URL http://dx.doi.org/10.1002/qj.49710444206.

Paltridge, Garth W. (1979) *Climate and thermodynamic systems of maximum dissipation*. Nature, Vol. 279: p. 630–631. ISSN 5714. URL http://dx.doi.org/10.1038/279630a0.

Paltridge, Garth W. (1981) *Thermodynamic dissipation and the global climate system*. Quarterly Journal of the Royal Meteorological Society, Vol. 107(453): p. 531–547. ISSN 1477-870X. URL http://dx.doi.org/10.1002/qj.49710745305.

Paltridge, Garth W. (2001) *A physical basis for a maximum of thermodynamic dissipation of the climate system*. Quarterly Journal of the Royal Meteorological Society, Vol. 127(572): p. 305–313. ISSN 1477-870X. URL http://dx.doi.org/10.1002/qj.49712757203.

Paltridge, G.W.; Farquhar, G.D. and Cuntz, M. (2007) *Maximum entropy production, cloud feedback, and climate change*. Geophysical Research Letters, Vol. 34: p. 14 708.

Phillips, Norman A. (1954) *E*nergy Transformations and Meridional Circulations associated with simple Baroclinic Waves in a two-level, Quasi-geostrophic Model1. Tellus, Vol. 6(3): p. 273–286. ISSN 2153-3490. URL http://dx.doi.org/10.1111/j.2153-3490.1954.tb01123.x.

Prigogine, I. (1947) *Étude thermodynamique des phénomènes irréversibles.*. URL http://worldcat.org/oclc/1526144.

Pujol, T. and Llebot, J. E. (1999) *Extremal principle of entropy production in the climate system*. Quarterly Journal of the Royal Meteorological Society, Vol. 125(553): p. 79–90. ISSN 1477-870X. URL http://dx.doi.org/10.1002/qj.49712555306.

Pujol, T. and Llebot, J. E. (2000a) *Extremal climatic states simulated by a 2-dimensional model Part I: Sensitivity of the model and present state*. Tellus A, Vol. 52(4): p. 422–439. ISSN 1600-0870. URL http://dx.doi.org/10.1034/j.1600-0870.2000.00092.x.

Pujol, T. and Llebot, J. E. (2000b) *Extremal climatic states simulated by a 2-dimensional model Part II: Different climatic scenarios*. Tellus A, Vol. 52(4). ISSN 1600-0870. URL http://www.tellusa.net/index.php/tellusa/article/view/12275.

Schroeder, Daniel V (2000) *An Introduction to Thermal Physics; int. ed.* (Addison-Wesley, San Francisco, CA).

Seager, R.; Murtugudde, R.; Clement, A. and Herweijer, C. (2003) *Why is There an Evaporation Minimum at the Equator?*. Journal of Climate, Vol. 16: p. 3793–3802.

Trenberth, Kevin E; Fasullo, John T and Kiehl, Jeffrey (2009) *Earth's Global Energy Budget*. Bulletin of the American Meteorological Society, Vol. 90(3): p. 311. URL `http://journals.ametsoc.org/doi/abs/10.1175/2008BAMS2634.1`.

Vallis, Geoffrey K (2006) *Atmospheric and Oceanic Fluid Dynamics: Fundamentals and Large-scale Circulation* (Cambridge Univ. Press, Leiden).

Walker, C. C. and Schneider, T. (2006) *Eddy Influences on Hadley Circulations: Simulations with an Idealized GCM*. Journal of Atmospheric Sciences, Vol. 63: p. 3333–3350.

Wallace, J M and Hobbs, P V (2006) *Atmospheric science: an introductory survey* (Academic Press).

Wyant, P. H.; Mongroo, A. and Hameed, S. (1988) *Determination of the Heat-Transport Coefficient in Energy-Balance Climate Models by Extremization of Entropy Production.*. Journal of Atmospheric Sciences, Vol. 45: p. 189–193. ISSN 0022-4928.

Yin, J. H. (2005) *A consistent poleward shift of the storm tracks in simulations of 21st century climate*. Geophysical Research Letters, Vol. 32: p. 18 701.

Ziegler, H. and Wehrli, C. (1987) *On a Principle of Maximal Rate of Entropy Production*. Journal of Non Equilibrium Thermodynamics, Vol. 12: p. 229–244.